Universidade de Aveiro Departamento de Engenharia Cerâmica e do Vidro
2012

João Pedro Fernandes Ramos

Efeito da Microestrutura do Óxido de Cálcio na Difusão de Isótopos

Effect of Calcium Oxide Microstructure on the Diffusion of Isotopes

Universidade de Aveiro Departamento de Engenharia Cerâmica e do Vidro
2012

João Pedro Fernandes Ramos

Efeito da Microestrutura do Óxido de Cálcio na Difusão de Isótopos

Effect of Calcium Oxide Microstructure on the Diffusion of Isotopes

University of Aveiro
2012
Department of Ceramics and Glass Engineering

João Pedro Fernandes Ramos

Effect of Calcium Oxide Microstructure on the Diffusion of Isotopes

Dissertation presented to the University of Aveiro in the fulfillment of the requirement for the awarding of the Masters in Materials Science and Engineering carried out under the supervision of Prof. Doutora Ana Maria Oliveira Rocha e Senos, Associate Professor in the Department of Ceramics and Glass Engineering of the University of Aveiro, and Doctor Thierry Stora, Target and Ion Source Team Leader, at the ISOLDE Facility, at the European Organization for Nuclear Research (CERN).

Financial support from CERN and Agência de Inovação, S.A. under the Grant SFRH/BEST/51352/2011.

I dedicate this work to my beloved girlfriend and to my family, to whom I owe everything…

The Board of Examiners

president

Prof. Doutor Jorge Ribeiro Frade
Full professor from University of Aveiro, Portugal

Doutor João Guilherme Martins Correia
Principal Researcher from ITN - Nuclear and Technological Institute, Sacavém, Portugal

Prof. Doutora Ana Maria de Oliveira Rocha e Senos
Associate professor from the University of Aveiro, Portugal (Supervisor)

Doctor Thierry Stora
Target and Ion Source Development Team Leader, ISOLDE Facility, CERN – European Organization for Nuclear Research, Switzerland (Co-supervisor)

Acknowledgements

Firstly of all I would like to thank my supervisors, Prof. Doutora Ana Senos and Dr. Thierry Stora, for the guidance through this work: not only because they were my scientific mentors but also because of their personal support and motivation.

At the University of Aveiro, I'm thankful to Maria João Bastos, Célia Miranda, Ana Ribeiro and Marta Ferro which are responsible for the material characterization tests in the Department of Ceramic and Glass Engineering. Thank for all the availability, patience, support and sympathy. Also to Professors Rui Ferreira, Margarida Almeida and Jorge Frade and for providing part of the essential equipment to my studies.

I would also like to thank my colleagues and friends from University of Aveiro, which not only gave me support in the work itself, but also personally. Thank you Cristina Fernandes, Erika Davim, Luís Vilhena, Filipe Davim, João Pereira, Sónia Patrício, Liliana Pires, Ana Rondão, Patrick de Sousa and others.

At CERN I would like to thank my friend and office mate, Alexander Gottberg, for everything, not only the help and motivation at work, but also for the warm welcoming at this new life and for the good times we passed together. I'm also thankful to Tânia Mendonça, Bernard Crepieux, Magdalena Kowalska, Michał Czapski, Christoph Seiffert, Martin Breitenfeldt, Gonzalo Izquierdo, Monika Stachura, Michael Owen, Jens Roder, Susanne Kreim, Dr. João Guilherme Correia, Thomas Schneider and all the other colleagues of the ISOLDE group.

For the personal support, even though we were very far apart, I want to thank my Portuguese friends Luís Duarte, Francisco Duarte, Rui Figueiredo, Diva Carreira and André Santos. I'm also grateful to my Portuguese friends and fellows at CERN: Luís Alberty, Gabriel Ribeiro, Vitor Gouveia, Dora Rio and David Rogrigues for all those fun trips and moments we pass together in Switzerland.

To the most important persons in my life, my sweet Diana and my family, I'm grateful for the constant and undeniable support. You were always there for me even when I was not for you, especially Diana to whose effort I'll be always grateful.

I would like to also thank Agência de Inovação, S.A. (Adi) and CERN for the financial support since April of 2011. I'm especially grateful to Adi for the selection and trust in me for this job and training at CERN

To everyone who directly and indirectly contributed to this work, I'm grateful for support in the fulfillment of my dream of working in science research and at such great organization as CERN.

keywords

radioactive ion beams, $CaCO_3$ decomposition, CaO sintering, diffusion, CaO reactivity, CERN, ISOLDE, ISOL

summary

Calcium oxide (CaO) powder targets have been successfully used at CERN-ISOLDE to produce neutron deficient exotic argon and carbon isotopes under proton irradiation at high temperatures (>1000^{o}C). These targets outperform the other related targets for the production of the same beams. However, they presented either slow release rates (yields) from the beginning or a rapid decrease over time. This problem was believed to come from the target microstructure degradation, justifying the material investigation.

In order to do so, the synthesis, reactivity in ambient air and sintering kinetics of CaO were studied, through surface area determination by N_2 adsorption, X-ray diffraction for crystalline phase identification and crystallite size determination, and scanning and transmission electron microscopy to investigate the microstructure.

The synthesis studies revealed that a nanometric material is obtained from the decarbonation of $CaCO_3$ in vacuum at temperatures higher than 550^{o}C, which is very reactive in air. This reactivity was studied, and it was observed that the CaO powder microstructure is changed through the reaction with air (hydration and carbonation of the oxide) and that this change is not completely reversible after thermal decomposition of the reaction products. Therefore, special care was taken in the target handling at CERN-ISOLDE. From the sintering kinetics, studied in the range of 1000-1200^{o}C, it was determined that this material's microstructure degrades, with the reduction of the specific surface area and decrease of the powder porosity. At 1200^{o}C, the specific surface area reduction is accentuated, reaching values of 50% of surface area reduction in 10h. These results suggest that the use of high temperatures, equal or higher than 1000^{o}C must be avoided, if the microstructural characteristics of the targets are to be preserved.

At CERN-ISOLDE, selected conditions for synthesis, handling of the target and target operation temperatures were chosen, based on the previous material research, and the obtained target material was tested under proton irradiation.

From the online studies, the newly developed target proved to show better initial and stable over time release rates of almost all isotopes investigated and especially the exotic ones. These results are essentially due to the nanometric characteristics of the produced target and to the use of operation and handling conditions that decreased the degradation of the microstructural characteristics.

Diffusion studies of Ar and Ne were also done in CaO through the application of a mathematical model, to the release curves of the respective isotopes at different temperatures, which enables the determination of the respective diffusion coefficients and activation energies.

palavras-chave

Feixes de iões radioativos, decomposição de $CaCO_3$, sinterização de CaO, difusão, reatividade do CaO, CERN, ISOLDE, ISOL

resumo

Alvos de pós de oxido de cálcio (CaO) têm sido usados, com sucesso, no CERN-ISOLDE para produzir isótopos de Árgon (com défice de neutrões) e de carbono, sob irradiação com protões a alta temperatura (>1000^{o}C). Estes alvos têm mostrado um desempenho superior a outros alvos usados para produzir os mesmos feixes. Contudo, apresentam baixas taxas de libertação de isótopos desde o início de operação ou uma redução rápida com o tempo. Suspeitou-se que este problema se devia à degradação da microestrutura do material, justificando a sua investigação.

Assim, a síntese, reatividade em ar ambiente e a cinética de sinterização do CaO foram estudadas, nomeadamente através da determinação da área superficial especifica por adsorção de N_2, difração de raios-X para identificação de fases e determinação do tamanho de cristalite e microscopia eletrónica de varrimento e transmissão para o estudo da microestrutura.

Os estudos de síntese do CaO revelaram que um material nanométrico, e muito reativo em ar, é obtido através da descarbonatação do $CaCO_3$ em vácuo a temperaturas superiores a 550^{o}C. Esta reatividade foi estudada e observou-se que a microestrutura do pó de CaO é alterada por reação com o ar (hidratação e carbonatação do óxido) e que esta alteração não é totalmente reversível após decomposição térmica dos produtos de reação. Assim, foram tomados cuidados especiais no manuseamento dos alvos de CaO. Da cinética de sinterização, estudada na gama de 1000-1200^{o}C, foi concluído que a microestrutura deste material se degrada com redução da área superficial específica e diminuição da porosidade do pó. A 1200^{o}C, a redução da área superficial específica é acentuada, atingindo-se valores de 50% de redução em cerca de 10h. Estes resultados indicam que a utilização de temperaturas elevadas, iguais ou superiores a 1000^{o}C, devem ser evitadas se se pretendem preservar as características microestruturais dos alvos.

No CERN-ISOLDE, as condições de síntese, de manuseamento do material e temperatura de operação do alvo foram escolhidas, com base nos estudos anteriores, e o material resultante foi testado sobre irradiação de protões.

Dos estudos online, o alvo desenvolvido provou ter melhores taxas de libertação iniciais e que se mantêm ao longo do tempo de libertação, comparativamente a outros alvos de CaO previamente usados no CERN-ISOLDE. Isto verificou-se em praticamente todos os isótopos estudados, especialmente nos exóticos. Estes resultados foram atribuídos às caraterísticas nanométricas do alvo produzido e à utilização de condições de manuseamento e de operação, tais que a degradação das características microestruturais do alvo é reduzida.

Estudos de difusão de Árgon e Néon foram feitos no CaO através da aplicação de um modelo matemático às curvas de libertação dos respetivos isótopos a diferentes temperaturas de operação, que permitiram a determinação dos respetivos coeficientes de difusão e energias de ativação.

Table of Contents

List of Figures iii
List of Tables vii
Lists of Symbols and Abbreviations ix
Introduction 1
Chapter I - State of the Art 5
I.1 Radioactive Ion Beams 7
I.1.1 The Chart of the Nuclides 8
I.1.2 Radioactive Ion Beam Applications 9
I.1.3 Production of Radioactive Ion Beams 9
I.2 ISOLDE at CERN 12
I.2.1 Layout of ISOLDE Facility 13
I.2.2 Target Unit 16
I.2.3 ISOLDE Pulse Shape 17
I.3 Target Materials 19
I.3.1 Diffusion 20
I.3.1.1 Main Diffusion Mechanisms 21
I.3.1.2 Factors Influencing Diffusion 22
I.3.1.3 Diffusion and ISOLDE Release Curve 22
I.3.2 Effusion 25
I.3.3 Other Important Material Requirements 25
I.4 Calcium Oxide Nanopowders 26
I.4.1 General Characteristics 28
I.4.2 Calcination 29
I.4.2.1 Effect of the Atmosphere and Temperature 31
I.4.2.2 Influence of the Precursor 33
I.4.3 Reactivity in Air 34
I.4.4 Sintering of Calcium Oxide 35
Chapter II - Experimental Procedure 39
II.1 Characterization Techniques 41
II.1.1 X-Ray Diffraction - XRD 41
II.1.2 Surface Area and Porosity Measurements through Isotherm Determination – BET/BJH 42
II.1.3 Differential Thermal and Thermogravimetric Analysis – DTA/TGA 44
II.1.4 Scanning Electron Microscopy – SEM/STEM 44

II.1.5 Transmission Electron Microscopy - TEM 45
II.1.6 Tape Station – Release Curves Measurement at ISOLDE 45
II.2 Raw Material 47
II.3 Calcination 49
II.4 Calcium Oxide Reactivity Tests 51
II.4.1 Sample Storage 51
II.5 Microstructural Evolution During Vacuum Sintering 52
II.6 Material Testing at ISOLDE-CERN 53
II.6.1 CaO Target Production at ISOLDE: “Old Procedure” 53
II.6.2 CaO Target Production at ISOLDE: “New Procedure” 54
II.7 Beam Tests at ISOLDE-CERN 56
II.7.1 Offline Measurements 56
II.7.2 Online Operation 56
Chapter III - Results and Discussion 59
III.1 Material Characterization Study 61
III.1.1 Synthesis of CaO 61
III.1.2 Reactivity in Air 66
III.1.3 Sintering Kinetics of CaO 70
III.2 Material Testing at ISOLDE-CERN 73
III.3 Online Studies 76
III.3.1 Isotope Yields 76
III.3.2 Yields Over Time 77
III.3.3 Isotope Release Properties 79
III.3.4 Diffusion and Effusion of Isotopes 80
Chapter IV - Conclusions 87
IV.1 Conclusions 89
IV.2 Outlook 90
References 93
Appendix 101

List of Figures

Figure I-1 - Chart of the nuclides, where the proton, neutron and fission driplines (B_p, B_n, B_F) can be seen. Vertical and horizontal lines represent the magic numbers and the colors the decay modes of radioactive isotopes. [11] 8
Figure I-2 - CERN accelerator complex. The types of beams (different colors) produced at CERN and their paths, can be seen, as well as the main experiments. [1] 13
Figure I-3 - Layout of the ISOLDE facility, describing all the steps of the process and zones. [17] 14
Figure I-4 – Target unit MK7 with VADIS ion source in 3D (a) and cut (b) – courtesy of Stefano Marzari. The numbers indicate the target container (1), the transfer line (2) and the ion source (3). The arrow indicates how the proton beam is made to collide with the target material, which is inside the target container. 16
Figure I-5 - Theoretical release curve, where final release curve display a fast and a slow component (courtesy of Alexander Gottberg). 18
Figure I-6 – (a) Simulation of the ISOLDE in-target isotope production yields for calcium oxide material with a thickness of 7g/cm^2 done with ABRABLA. (b) Best historical experimental yields obtained by the CaO target material at ISOLDE. The filled marks were measured at the actual ISOLDE installations (PSB), the unfilled marks were measured in the old ISOLDE installation near the SC. [43] 27
Figure I-7 - Standard free energy of a reaction in function of the temperature. The dashed lines represent the equilibrium of the gas pressure above the reactions. [30] 29
Figure I-8 - Representation of the $CaCO_3$ decomposition and the formation of the porous layer of CaO. [30] 30
Figure I-9 - Mechanisms of solid state sintering. Only 4 to 6 cause densification, but all cause neck growth influencing densification. [30] 36
Figure II-1 – Picture of the fast tape station at ISOLDE (a), scheme of the RIB production until it arrives at the tape station [26] (b) and schematic representation of the tape station operation to build the release curve [26] (c). 46
Figure II-2 - XRD of the raw material, $CaCO_3$, used to produce CaO. 47
Figure II-3 - Thermal analysis of calcium carbonate in air atmosphere. 48

Figure II-4 – SEM observation of the $CaCO_3$ powder (a) and particle size distribution determined by laser diffraction (b). 48
Figure II-5 – Furnace temperature and pressure readouts for the samples calcined at 600°C (a), 700°C (b) and 800°C (c). The beginning of the reaction (A) and end (B) are marked on the figure. 50
Figure II-6 – Pumpstand used to produce the CaO at ISOLDE. In the picture: the oven (a), the turbo pump (b), and below a rotary pump (c), the controls for the water cooling and others (d), the bottle of Ar to purge the system (e) and the window used to measure the temperature with the pyrometer (f). 54
Figure II-7 – Gloves box used to do the material change to the target unit. In the picture: the pre-chamber (a), the gloves box main chamber (b), a bottle of Ar to fill both pre-chamber and main chamber (c) and a rotary pump (d). 56
Figure II-8 - Schematic representation of a target container indicating the sides (a) and the center (d) of it, where the transfer line is also represented (c). 57
Figure III-1 - Plot of the specific surface area (SSA) and the crystallite size (XS) versus temperature for the calcined powder, obtained under similar vacuum conditions, and 2h of holding time..... 62
Figure III-2 – SEM Microstructure of the $CaCO_3$ powder (a), the N80 sample (b), a high resolution SEM at the N80 sample (c) and STEM done to N80 sample (d). 63
Figure III-3 – TEM observations of CaO sample, N80..... 64
Figure III-4 - Isotherms obtained by adsorption of N_2 for the samples D80 and D10. 65
Figure III-5 - Pore size distribution of the samples N80 and D10. 65
Figure III-6 - Thermal analysis of the N80 sample after decomposition and normal handling (a) and after intentional exposure at air for 2 days (b). 67
Figure III-7 - XRD of the N80 powder after normal handling (a) and left at air for 2 days (b). 68
Figure III-8 - Plot of the weight gain over two days for three samples of CaO with different initial surface areas (a) and respective amplification for shorter times (b). The dotted line represents the weight gain if the powder would be completely hydrated. 68
Figure III-9 - Plot of the specific surface area versus the temperature for 3 min and 10h of thermal treatment. The isolated point corresponds to the initial powder. 70

Figure III-10 - Plot of the surface areas versus temperature for several temperature and respective fits. 71
Figure III-11 - Plot of the diameter variation with time at 1200^{o}C. 72
Figure III-12 – Arrhenius plot accordingly to the equation (I.28), from the German and Munir model [71]. 72
Figure III-13 – SEM micrographs of the sintered samples at 1200^{o}C for 3 min, a) and d), 2h, b) and e) and 10h c) and f). 73
Figure III-14 - Yield evolution on ^{32}Ar on target CaO#191 in 2001 at ISOLDE (courtesy of Susanne Kreim) and ^{31}Ar in CaO#408. 78
Figure III-15 - Yields of ^{35}Ar measured throughout the run for targets CaO#469 and CaO#419. 78
Figure III-16 – Example of release curve and respective fit, from equation (I.2), for ^{35}Ar at 520^{o}C (a) and release efficiency obtained through the fitting of the experimental release curves of ^{35}Ar for three different temperatures (b) in target CaO#469. 81
Figure III-17 – Example of release curve and respective fit, from equation (I.2), for ^{19}Ne at 520^{o}C (a) Release efficiency obtained through the fitting of the experimental release curves of ^{19}Ne for three different temperatures in target CaO#469. 83
Figure III-18 - Plot of the ln(D) vs 1/T in order to determine D_0 and Q for ^{19}Ne and ^{35}Ar (the latter by a different method. 85

List of Tables

Table I-1- Table with target materials most used at ISOLDE: T_m is the melting point temperature, T_{max} is the maximum operation temperature, p_{vap} is the vapor pressure, ρ is the theoretical density and ζ is the target thickness. [28] 19
Table I-2 – General characteristics of calcium oxide. [47] 28
Table I-3 – Summary of precursors form, calcinations conditions and CaO powders characteristics reported in the open literature. 32
Table I-4 – Kinetic exponents for surface area and shrinkage in initial stage models. [33,73] 37
Table II-1 – Shape factors and respective packing fractions for different powder geometries. [80] 43
Table II-2 – Characteristics of the raw material ($CaCO_3$) 49
Table II-3 - Experimental conditions used to decompose $CaCO_3$ into CaO, in vacuum. ... 50
Table II-4 - Weight gain of one CaO sample with different desiccants. 51
Table II-5 - Experimental conditions in CaO sintering experiments 52
Table II-6 - Calcination conditions for the "old process" of the CaO target production at ISOLDE. 54
Table II-7 - Calcination conditions for the "new process" of the CaO target production at ISOLDE. 55
Table II-8 - Summary of the online measurements and tests done on target CaO#469. 57
Table III-1 – Summary of the decomposition conditions and characteristics of the obtained powders. 61
Table III-2 – Powder characteristics before and after air exposure and reversibility thermal tests. 69
Table III-3 – Characterization of the CaO powders produced at ISOLDE, by the old target production method before (T12) and after a thermal treatment at 1200°C, 48h (S12). 74
Table III-4 – Characterization of the CaO powders produced at ISOLDE, using the new targets procedure (T80 and S80 and comparison with CaO powder obtained at UA (N80). 74
Table III-5 – Measured yields and respective conditions for target CaO#469 and the comparison with database yields. 76

Table III-6 - Release time constants obtained by fitting the data with equation (I.2) for target CaO#419 and CaO#469 for ^{35}Ar. 79
Table III-7 - Calculation of the release efficiency for Ar isotopes for the target CaO#469 and other older targets. Y_{prod} calculated from ABRABLA simulation for the different target thicknesses. 80
Table III-8 - Fitted effusion and diffusion parameters for ^{35}Ar for three different temperatures on target CaO#469. 81
Table III-9 - Obtained diffusion parameters (neglected contribution from effusion) through the release efficiency of ^{35}Ar for three different temperatures on target CaO#469. 82
Table III-10 - Obtained effusion and diffusion fitted parameters for ^{19}Ne for three different temperatures on target CaO#469. 84
Table III-11 - Values of Q and D_0 and respective R^2 for ^{19}Ne and ^{35}Ar. 85
Table A-1 - Characteristics of the raw material ($CaCO_3$) used at ISOLDE to produce past CaO targets in the past (CC2). 101

Lists of Symbols and Abbreviations

Symbols

A	Atomic mass
α	Weight factor between fast falling and slow falling
B_F	Fission dripline
B_n	Neutron dripline
B_p	Proton dripline
C	Concentration of the diffusion species
γ	Exponent related to the sintering mechanism related with surface area reduction
D	Diffusion coefficient
D_0	Diffusion pre-exponential factor
λ_f	Decay constant for the fast fall of the release curve
λ_i	Isotope decay constant
λ_r	Decay constant for the rise of the release curve
λ_s	Decay constant for the slow fall of the release curve
σ	Isotope production cross section
ε_{sep}	Separator efficiency
ε_{is}	Ion source efficiency
ε_{transp}	Transport efficiency
ε_{rel}	Target Release efficiency
ζ	Target thickness
G	Crystallite size (determined by X-Ray Diffraction ,Scherer equation)
G_{BET}	Average particle size from surface area determination
$G_{Coulter}$	Average particle size from particle size determination by laser diffraction
f	Particle shape factor
i	Beam intensity
J_x	Flux of diffusion species
k	Constant for German and Munir model of surface area reduction
k_0	Constant term for a given material for surface area reduction
k_r	Rate constant of a decomposition reaction

k_s	Constant related to the shrinkage during initial stages of sintering
l	Length of the pellet after thermal treatment
l_0	Initial length of the pellet (isothermal conditions)
n	Number of target atoms exposed to the incident beam
N	Neutron number
N_0	Number of radioactive isotopes at t=0
m	Herring scaling factor
$p(t)$	Release curve or delay curve
p	Pressure
$p_v(t)$	Effusion related release function
$p_{v1,v2}(t)$	Effusion related release curve for an ISOLDE target
$p_\mu(t)$	Diffusion related release function
$p_\infty(t)$	Release curve when isotopes have an infinite half-life
p_{CO2}	Partial pressure of carbon dioxide
p_{vap}	Vapor pressure
ρ_0	Fraction density
ρ	Theoretical density
Q	Activation energy
R	Universal gas constant
r	Particle radius
S	Specific surface area
s	Exponent related to the sintering mechanism related to the shrinkage
S_0	Initial surface area (isothermal conditions)
T	Temperature
t	Time
$T_{1/2}$	Half-life
$t_{collection}$	Tape station collection time
t_f	Slow falling (time constant)
T_C	Temperature at the center of the container
T_m	Melting point temperature
t_{delay}	Tape station delay time
T_{max}	Maximum operation temperature

$t_{measurement}$	Tape station measurement time
t_r	Rise time (time constant)
T_S	Temperature at the side of the container
t_s	Fast falling (time constant)
$t_{transport}$	Tape station transport time
θ	Flux of the incident beam
w	Weight loss during decomposition reaction
μ	Diffusion delay time parameter
v	Effusion delay time parameter
v_1	Effusion delay time parameter (E. Bouquerel equation)
v_2	2nd effusion delay time parameter (E. Bouquerel equation)
Y_{obs}	Observed yield
Y_{prod}	In-target production yield
Z	Proton number

Abbreviations

BET	Brunauner, Emmet and Teller
BJH	Barret-Joyner-Halenda
CERN	European Organization for Nuclear Reasearch
DTA/TGA	Differential Thermal and Thermogravimetric Analysis
FWHM	Full Width at Half Maximum
EBIS	Electron Beam Ion Source
EDS	Energy Dispersive X-ray Spectrometer
GPS	General Purpose Separator
HRS	High Resolution Separator
ICDD	International Center of Data Diffraction
IS	Ion Source
ISOL	Isotope Separator Online
ISOLDE	Isotope Separator Online Device (ISOL Facility in CERN)
IUPAC	International Union of Pure and Applied Chemistry
INTC	ISOLDE and Neutron Time-of-Flight Experiments Committee
LHC	Large Hadron Collider
PDF	Powder Diffraction Files
PSB	Proton-Synchrontron Booster
PSD	Pore Size Distribution
RFQ	Radio Frequency Quadrupole
RIB	Radioactive Ion Beam
RT	Room Temperature
SC	Proton-Synchro-Cyclotron
SEM	Scanning Electron Microscopy
SSA	Specific Surface Area
STEM	Scanning Transmission Electron Microscopy
STP	Standard Temperature and Pressure
TEM	Transmission Electron Microscopy
TT	Thermal Treatment
UA	University of Aveiro

VADIS	Versatile Arc Discharge Ion Source
XRD	X-Ray diffraction
XS	Crystallite Size
WITCH	Weak Interaction Trap for Charged Particles

Introduction

CERN, the European Organization for Nuclear Research, is a well-known centre for fundamental physics research and hosts the Large Hadron Collider (LHC), the highest energy particle accelerator presently in operation. The beams produced with different energies in the large accelerator complex at CERN are available to numerous experiments. One of such facilities, ISOLDE (acronym for Isotope Separator On Line Device), aims at the production of beams of radioactive isotopes. [1,2]

The ISOLDE facility is located near the Proton Synchrotron Booster (PSB) at CERN, which supplies the facility with a pulsed proton beam [1]. The proton beam is then conducted by a series of (bending and focusing) magnets to two separate target stations. Through this method, thick targets are bombarded with high-energy protons and nuclear reactions of spallation, fission and fragmentation occur inside the target. The reaction products are stopped in the bulk of the target material, diffuse out, are pumped into an ion source and are accelerated to form a secondary radioisotope beam. Different target/ion source units can be coupled to the ISOLDE front-ends for the production of the different radioactive ion beams (RIB). This technique is a particularly good and powerful method for the production of pure low energy RIB. [3] To date, ISOLDE is the facility which offers the largest number of different beams (eg. more than 1000 isobars of 73 chemical elements) in an ISOL-type facility, resulting from constant target and ion source developments over the last 40 years. [2]

The targets used are made of refractory materials assembled in thick targets, such as pure metals (molten, powder, foils), oxides (powder, fibers), carbides and other compounds. [4,5] These targets must be designed with important considerations: (i) target material must be chosen to optimize the release rate (yield) of the required isotope; (ii) rapid diffusion rate is important when short lived isotopes are required, or else the nuclei would have decayed before getting to the ionizer; for a rapid diffusion rate a high temperature and a material with minimal diffusion lengths (like fine powder or thin foil) are required; (iii) rapid effusion rate, for example, through a material with an open internal structure permitting the nuclei reaching the ionizer quickly; (iv) good structural strength at high temperatures; (v) uniform temperature in the target to prevent condensation of the required radioactive species and to reduce the thermal stresses in the target; this translates into good thermal conductivity of the target material for high intensity primary beam. [6]

As referred before, target operating temperatures must be as high as possible to reduce the time constants of the isotope diffusion and effusion release processes, minimizing decay losses before extraction. The maximum operating temperature is constrained by the following requirements: (i) limited sintering to preserve the target release performance under pulsed and intense proton beam irradiation; (ii) reduced stable beam contaminants coming from chemical impurities; (iii) a moderate equilibrium vapour pressure (~10^{-2} Pa) compatible with the ion source operation. [4]

As so, the best target microstructure was defined as the one having a high porosity (>30%) in the macrosize range (>100 nm) within a narrow size distribution, nanosized grains, and stability at high temperatures. [7,8]

Calcium Oxide (CaO) targets have been successfully used at ISOLDE to produce neutron deficient exotic argon isotopes and carbon isotopes, released as CO and CO_2 molecules. Such targets outperform other related targets used to produce the same beams, such as MgO sintered powder or TiO_x fibers. However, either some CaO target units display a slow release rates from the beginning or a rapid decrease over time when operated under proton irradiation. This is believed to come from a degradation of the initial microstructure of the targets, caused by pre-sintering effects. [9]

The large potential of these targets, for the production of exotic isotopes and the drawbacks detected in the release process, justifies the need to investigate the microstructure evolution of CaO targets, using conditions of temperature and pressure close to that of target operation under proton irradiation and its effect on the isotope diffusion.

Chapter I - State of the Art

I.1 Radioactive Ion Beams

Radioactivity, which was first discovered by Henri Becquerel in 1895, is the spontaneous emission of radiation by an atomic nucleus. The emitted radiation can be of different types, most prominently in ascending order of penetration and descending order of energy: alpha (α - ^{4}He nuclei) that can barely penetrate a sheet of paper, beta (β - positrons or electrons) that can penetrate a few millimeters of aluminum and gamma (γ – high energy photons) which can penetrate several centimeters of lead. [10] The emission of the radioactivity from a specific nucleus can reveal much about it, depending on the types of radiation and energy. It is by this emission of radiation that the less stable nuclei get to a more stable state, and thus this process is called decay.

The short ranged, nuclear force keeps the nucleus together, otherwise it would break apart due to the very large repulsive Coulomb forces between protons, which is partly compensated by the number of neutrons in the nucleus, since they experience only attractive nuclear forces. The balance between the Coulomb force and the nuclear force, or the ratio of protons and neutrons for a certain isotope is what defines the stability of a nucleus. [10] This leads us to the question: how many nuclides exist, how many have been observed and which ones are stable? First of all, stable nucleus and very long lived isotopes, the nuclei which "natural" mater is made of, mean that a possible decay process occurs in the time scale of the universe or larger. [11] The other nuclei are called radioactive isotopes, or simply radioisotopes.

In order to study in detail nuclear subnuclear elementary particles and high energy physics particle accelerators are continuously developed, constructed and operated. A particle accelerator is a device in which charged particles (beam) are accelerated with electromagnetic fields to high energies. These particles can then be sent onto a fixed target or brought to collide with another particle beam in the opposite direction. Advancements in technology allow to build more powerful accelerators, to study the elementary particles and their interactions. Usually, the charged particles that are accelerated are: protons, electrons, positrons, antiprotons, ions and even unstable isotopes, which is the case of ISOLDE (acronym for Isotope Separator Online Device) at CERN. [12]

I.1.1 The Chart of the Nuclides

The chart of nuclides, shown in Figure I-1, displays all the presently known nuclei in a grid of proton number (*Z*) versus neutron number (*N*). There are 186 stable nuclei and around 3600 observed radioactive isotopes, although 6000 are believed to exist in total. [11] Standard databases also include for each nuclide the measured properties, among which are, relative abundance (for stable nuclides), decay modes, half-lives (for the radioactive ones) and masses. [13] Databases of known nuclides and the chart itself can be found on the *Karlsruher* Chart [14] or on the internet in the websites of the International Atomic Energy Agency [15] and the National Nuclear Data Center [16] (both of them use several sources to keep the data up to date). Obviously this chart is a very useful tool for physicists in these related fields and a good overview of what are the known nuclides and which are their properties.

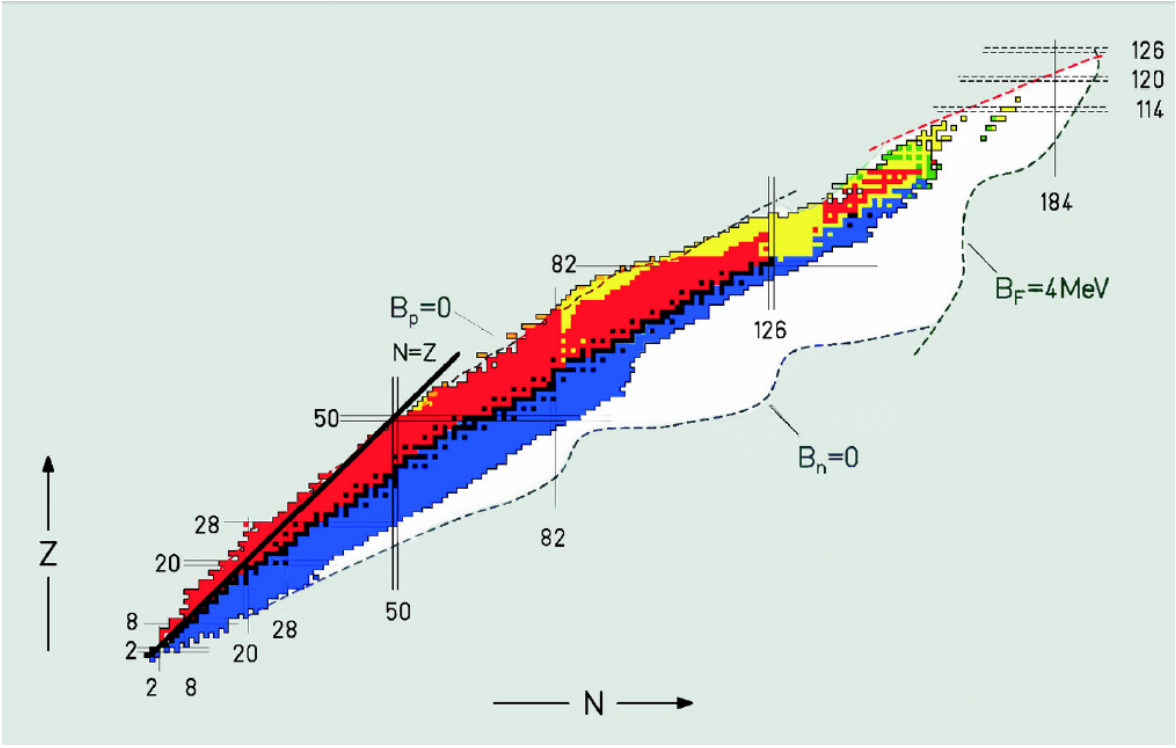

Figure I-1 - Chart of the nuclides, where the proton, neutron and fission driplines (B_p, B_n, B_F) can be seen. Vertical and horizontal lines represent the magic numbers and the colors the decay modes of radioactive isotopes. [11]

In Figure I-1, the stable nuclei (black squares) form the backbone of chart, and the color squares represent the radioactive isotopes (colors represent each type of decay mode). The vertical and horizontal thick lines provide the so-called magic numbers of protons or neutrons where the nuclides are especially stable. While the *N*=*Z* line follows

the "valley of stability" for light masses, this does not apply for heavy nuclei anymore: they have more neutrons than protons. This can be explained by the increase of Coulomb forces with increasing Z as mentioned above. The neutron ($B_n=0$) and proton driplines ($B_p=0$) represent the theoretical limit at which nuclei are believed to exist. Also the theoretical fission barrier line (B_F) at which no nuclide can exist without spontaneously fission to form smaller nuclei. The white zones represent regions where nuclei are believed to exist but still unknown. The isotopes that are away from the zone of the stability of the nuclear chart have very small half-lives and are very unstable, and therefore are much more difficult to produce and study. These are called the exotic nuclei.

I.1.2 Radioactive Ion Beam Applications

The research program based in radioactive ion beams (RIB) facilities aims at discovering fundamental properties of nuclear structure and at explaining the nuclide chart up to the predicted frontier. This covers, for example, the precise determination of nuclear masses, research on the properties of excited nuclear states, studies of radioactive decay modes, the precise determination of nuclear radii, spins and moments and also the investigation of atomic structure of radioactive elements. Fundamental interactions are also studied by RIBs, providing a contribution to the understanding of the Standard Model at low energies. RIBs are as well extremely useful in other fields like in astrophysics, trying to understand the constituents and the nuclear genesis in the stars, in which the energy is generated though nuclear reactions amongst stable and radioactive nuclei, and which can last for billions of years or explode in a few seconds. Life sciences are investigated with RIBs, in biochemistry and especially in the field of nuclear medicine studying the use of radioisotopes in medical diagnostics and therapy. Finally, an important field of research is solid state physics, in which radioisotopes are implanted as probes and act as diagnostic tools to deliver information about the environment in which they are implanted. In this way these radiotracers are used to study diffusion dynamics, surface, interface and bulk properties, spintronics and semiconductors. [11,2]

I.1.3 Production of Radioactive Ion Beams

RIBs are produced by different techniques where a beam of protons, neutrons, electrons, light or heavy ions are brought to collision with a target. [11] Several reactions and

beam target combinations are used to produce the required radioactive isotopes. [17] There are 3 major types of such reactions used at CERN-ISOLDE:

• Spallation - it happens when a proton with high kinetic energy (between hundreds of MeV and a few GeV) hits a target. This reaction can be described in a two-step reaction: first a particle is made to collide with the nucleus exciting it to a high energy state. In the second step, the excited nucleus emits single nucleons to lower its excitation state. This reaction is best suited to produce proton-rich isotopes, with a few protons and/or neutrons less than the original element. [18]

• Fragmentation - projectile fragmentation reactions are induced by a high-energy heavy ion beam with energies above 50 MeV per nucleon. [17] It implicates heavy-ions being broken up into lighter elements, on a target. The fragmentation reaction can also happen in target nuclei, when high energetic protons hit a heavy target. [18] This reaction produces a wide range of nuclei, both neutron and proton-rich, and also light nuclei.

• Fission - it happens when an incident particle, proton, neutron, electron or photons is absorbed by the nucleus. If the incident energy is high enough, two nuclei and a number of free nucleons are formed. In "cold fission" (no neutrons or gammas are emitted) a big nucleus is split in two other nucleus of smaller mass. [10] One of the produced nuclei will have a mass of about ⅓, and the second of roughly ⅔ of the mass of the original element. [13]

• Fusion-evaporation – a 4th reaction, used throughout different ISOL facilities (and not at ISOLDE) consists on inducing two nucleus to be brought together overcoming the energy of the Coulomb barrier. The resulting nucleus evaporates nucleons. This method produces highly excited nuclei in the neutron-rich side of the stability region and super-heavy elements.

The nuclear reactions described above are influenced by the nature of the projectile, its energy and nature of the target. [17] To meet the demand of ever increasing RIB intensities, new accelerators that can deliver higher intensities and target systems to handle the power deposition, resulting from the later, are under development. The production of unwanted species is often more intense compared to the desired exotic nuclei. For this, selectiveness has to be improved to separate the wanted species from the unwanted ones (contaminants). By the very definition of exotic nuclei, it is known that they have very short half-lives. As the isotopes decay, the production and the transport from the target to

the experimental setup has to be fast. The efficiency has also to be promoted by developing better ionization, acceleration and transport systems of the isotope beams. [17]

There are two methods to produce RIBs: the in-flight separation technique [19] and the isotope separator online (ISOL) technique. Both methods transport the produced nuclei out of their production zone, where there is a large radiation background due to nuclear reactions, to a well shielded experimental setup. This has two advantages: creating low radiation background conditions for the experiment, and to purify and prepare the beam with respect to its necessary conditions: energy, time and ion optical properties for the following experiments. [17]

The ISOL technique uses production methods in a thick target, thermalization in a solid, liquid or gas catcher, which often is the same as the target, as in the case of ISOLDE at CERN. The radioactive isotopes are then extracted from the catcher material and ionized in an ion source. After being extracted from the ion source the isotopes are mass analyzed by a dipole magnet and afterwards post-accelerated to the required energies for use in experiments. [17] The beams resulting from this technique are of excellent ion optical quality (energy resolution, time structure and emittance) but the thermalization process described and the eventual re-acceleration slow down the delivery of isotopes and causes additional losses for short lived isotopes. [11]

Besides ISOLDE at CERN, which is a leading ISOL facility, there is also much development ongoing on other facilities like: GSI at Germany, LISOL at Belgium, IGISOL in Finland, ISAC-TRIUMF in Canada, GANIL in France, IRIS in Russia and JAERI in Japan. [17]

The quality of a RIB facility is mainly determined by the intensity and purity of its beams. For an ISOL facility the beam intensity can be theoretically described by the expression [20]:

$$i = \theta . \sigma . n . \varepsilon_{rel} . \varepsilon_{is} . \varepsilon_{sep} . \varepsilon_{tranp} \qquad \text{(I.1)}$$

where i, is the beam intensity in ions per second per μA of the incident beam, θ is the flux of the incident beam in particles per second per μA, n is the number of target atoms exposed to the primary beam per unit of area and σ is the cross-section to produce the desired isotope (cross section is considered to be the effective size of a nucleus for a certain nuclear probabilistic reaction to happen). ε_{rel} is the release efficiency of the target, ε_{is} is the ion source efficiency and ε_{sep} and ε_{tranp} are the efficiencies of the transmission of

the mass separator and of the transmission to the users experimental setup, respectively (these last two efficiencies are normally close to unity). The ε_{rel} is directly related to diffusion through the target material and effusion through the material porosity to the ion source. It can be greatly improved by developing the target material. By investigating the microstructure and the diffusion and effusion of the isotopes on the target material, these properties can be vastly improved and in this way, the target release efficiency would be increased too, promoting the overall beam intensity, as will be seen later in this work.

I.2 ISOLDE at CERN

CERN, the European Organization for Nuclear Research is the biggest experimental laboratory center for fundamental particle physics research. It presently hosts the LHC (Large Hadron Collider), the highest energy and largest particle accelerator in operation in the world. CERN was founded in 1954, and it is located across the Franco-Swiss border area near Geneva and is operated by 21 member states (Portugal being one of them). Other non-member states and organizations are also involved in the numerous experiments taking place at CERN. CERN is a global example of successful international collaboration for scientific interests. CERN's mission is defined in four levels: (i) educating the scientists of tomorrow; (ii) fundamental research; (iii) promoting international collaboration and (iv) promoting the transfer of technology. At CERN beams of particles are accelerated to high energies and are brought to collide between themselves or with targets. By doing this, scientists expect to understand better the fundamental laws of nature. [1]

The beams produced at the large accelerator complex at CERN are delivered at various energies to numerous experiments. One of such facilities, ISOLDE, has the aim of producing beams of radioactive isotopes.

It was in 1964 that ISOLDE was originally proposed at the 0.6GeV Proton-Synchro-Cyclotron (SC) at CERN. The first experiments started in 1967 and since then, the ISOLDE facility has suffered several upgrades. Since 1989 that ISOLDE is supplied by the 1-1.4GeV Proton-Synchrotron Booster (PSB), as Figure I-2 shows. [2] This not only provides ISOLDE with more energetic protons but also the proton intensity was increased up to 2μA. This, together with different technological developments, increased the intensities and the number of accessible isotopes. Right now ISOLDE is the world-leading

facility of its type, which can provide more than 1000 isotopes with half-lives down to milliseconds out of 73 chemical elements, from Z=2 to 92, with intensities up to 10^{11} atoms per second.

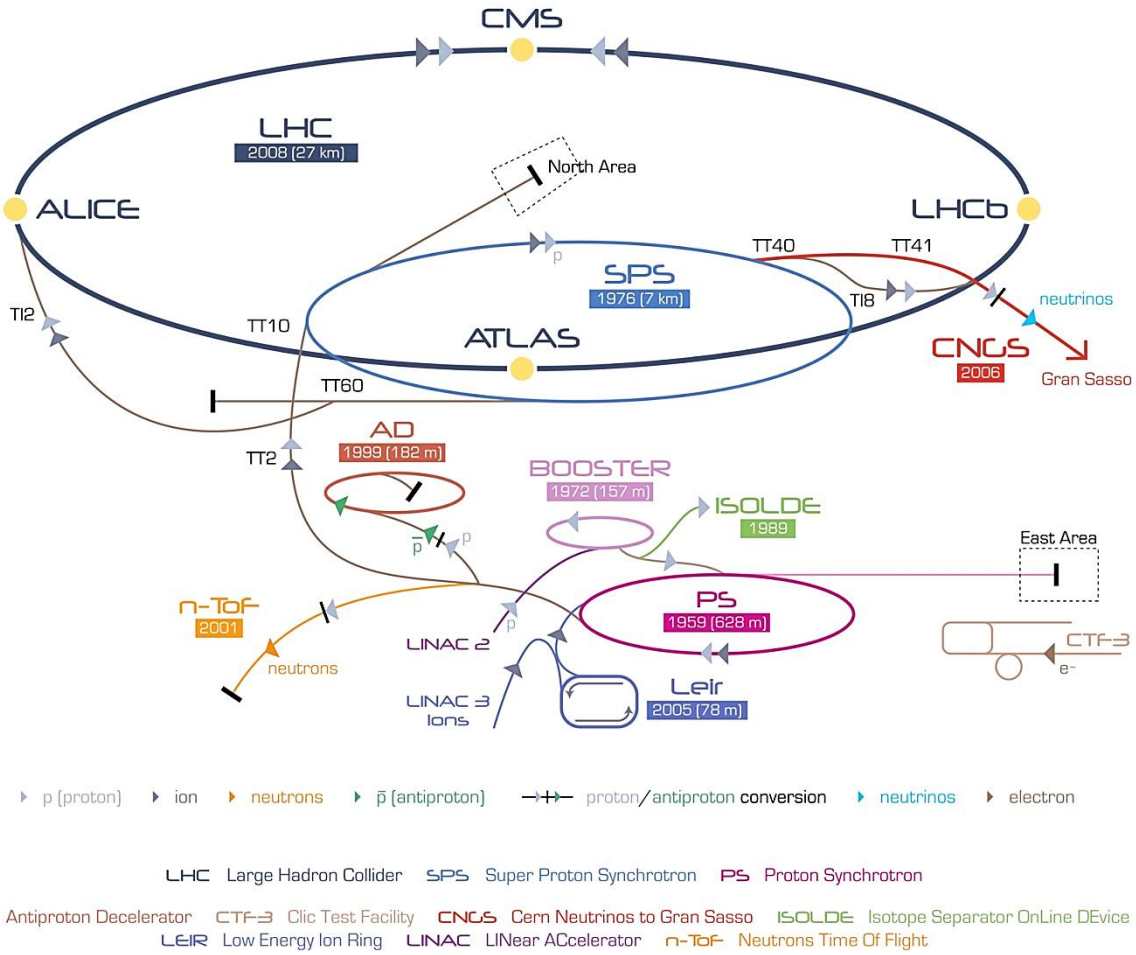

Figure I-2 - CERN accelerator complex. The types of beams (different colors) produced at CERN and their paths, can be seen, as well as the main experiments. [1]

I.2.1 Layout of ISOLDE Facility

The ISOLDE experimental facility, runs between 350 and 400 shifts of 8 hours of online operation every year [21]. The PSB supplies the ISOLDE facility (Figure I-3) with about 30-40% of CERN's protons. The proton beam can then be redirected by a series of focusing and bending magnets to two different front ends, which supply the fixed targets. The protons are delivered either in pulse sharing mode, sharing the supercycle between the two, or individually. Some targets can have a converter that is used to transform a beam of protons into a field of neutrons. With this technology, neutron-rich isotopes with low level of contaminants can be obtained from actinide targets. [17]

When the high energy primary beam hits the target, spallation, fragmentation and fission reactions take place producing radioactive nuclei that are stopped (also called thermalization) in the bulk of the target material and then diffuse out of it. The isotopes then travel through so-called processes of effusion through the transfer line to the ion source, where they are ionized. An extraction electrode accelerates them at a potential up to 60 keV, producing the secondary beam. In the ion source, several ionization mechanisms are used, but generally singly positively or negatively charged ions are produced [17]. Usually the target, transfer line, ion-source and, if installed, the neutron converter are referred to as the target unit or simply as target [3].

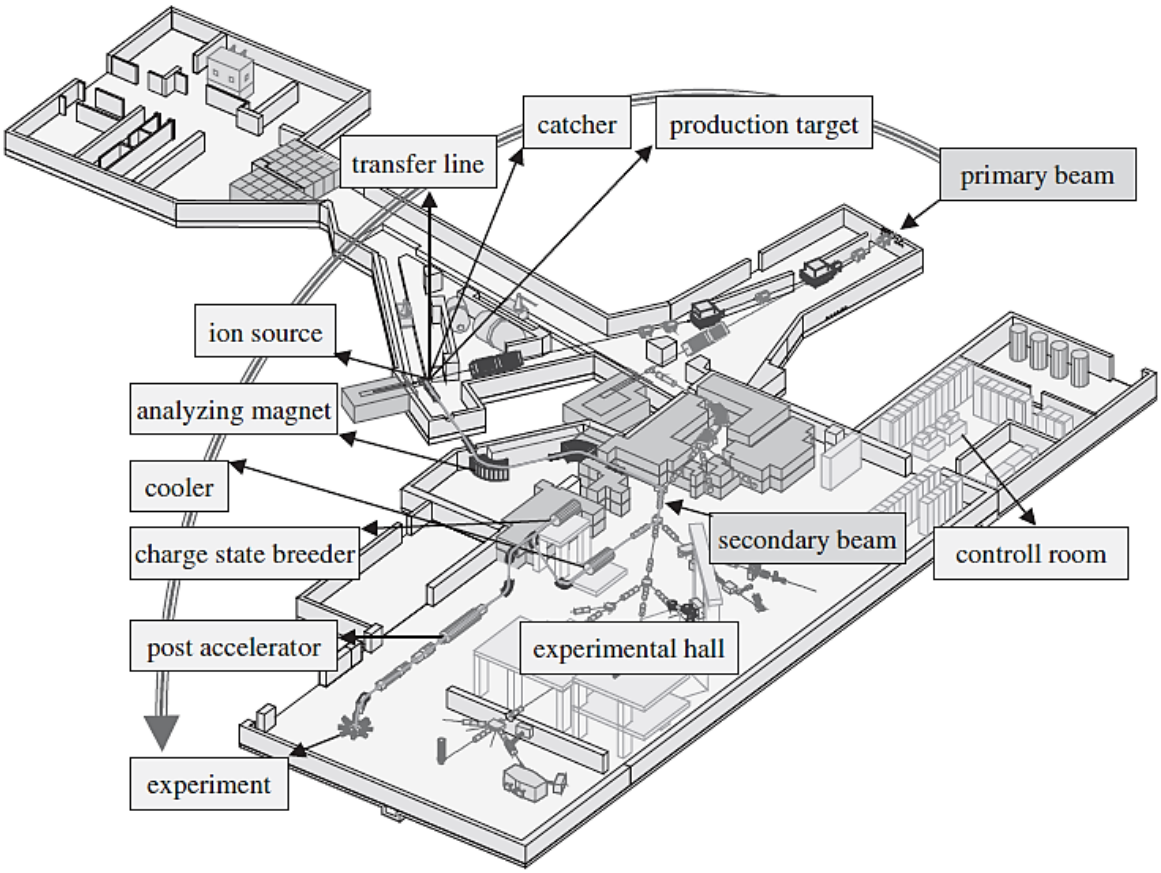

Figure I-3 - Layout of the ISOLDE facility, describing all the steps of the process and zones. [17]

To mass analyze and separate the isotopes each target station, also called frontend, is connected to a mass separator magnet: the General Purpose Separator (GPS) or to the High Resolution Separator (HRS). The magnets separate the different masses according to the Lorentzian magnetic principle [22] and both can feed a common beam distribution system which connects to the different experiments in the ISOLDE hall. The GPS has less resolution than the HRS, but allows for the separation and use, in parallel, of three beams

of different masses to three different experiments at the same time. The separation of different masses with HRS can provide the facility with one high resolution beam and is a more complex system with 2 magnets with ion-optical systems for corrections. [3]

Some experiments get the beam directly from the mass separators while others need the beam to be stopped and cooled to be highly ionized and/or post accelerated. The Radio Frequency Quadrupole (RFQ) cooler, cools down the ion beam to improve its ion-optical properties and bunches the beam. This is done to improve the peak to background ratio that is required in some experiments, or to inject the beam into the charge state breeder. The charge state breeder is an electron beam ion source (EBIS) that changes the singly charged radioactive ions to multiple charged ion state, as required for post acceleration. Finally, the highly ionized beam can be accelerated to several MeV per nucleon and sent to experimental setups which require high kinetic beam energies [17].

There is big concern and legal obligation about radiological protection at ISOLDE, since there are high amounts of radioactivity that originates from normal operation of the targets and by the RIB itself. To comply with the legislation aiming to protect the ISOLDE group and its users, who have to use a dosimeter on the ISOLDE experimental hall, the strong radioactive target zone is completely separated from the hall. It has dedicated ventilation, is separately pumped and is highly shielded with steel, concrete blocks and 8m of soil. The targets are manipulated, stored and changed by industrial robots without the need for human physical presence. The target zone is also equipped with a class A radioactive laboratory to safely and correctly handle any radioactive materials. [3] After the irradiation and operation time, the targets are disposed as radioactive waste. [23]

An important part of the ISOLDE infrastructure is made of beam diagnostics, since it permits the delivery of good quality RIB to the physics experiments. Part of these instruments, are the wire scanners and grids that permit to see the position and the profile of the beam, faraday cups that measure the overall intensity of the beam in several positions along the beam line, tape stations through which we can measure the release rates (yields) and obtain the release curve of radioactive isotopes. There are gamma detectors that allow the identification of the produced isotopes through a gamma spectrum. Some of these instruments will be described in larger detail later, in the experimental procedure chapter (see section II.7).

Furthermore, the operation of the entire ISOLDE facility, from the vacuum systems, to the beam distribution system and diagnostics, and all target parameters, with exception of the experiments, is done in the control room, by several computers and other control systems in a user friendly environment. [3]

I.2.2 Target Unit

The heart of an on-line isotope separator is its target and ion source. The performance of these components is an essential part for the delivery of high quality beams in a facility like ISOLDE. Yearly, in average, ISOLDE produces 30 target units with typical utilization from 24h to 300h with an average of 64h [23]. Around 30 different target materials, 5 transfer lines and 5 types of ion-sources are available at ISOLDE, making nearly 100 different possible combinations, which are chosen depending on the required radioactive ion beams. The targets can be either made of solid or liquid materials.

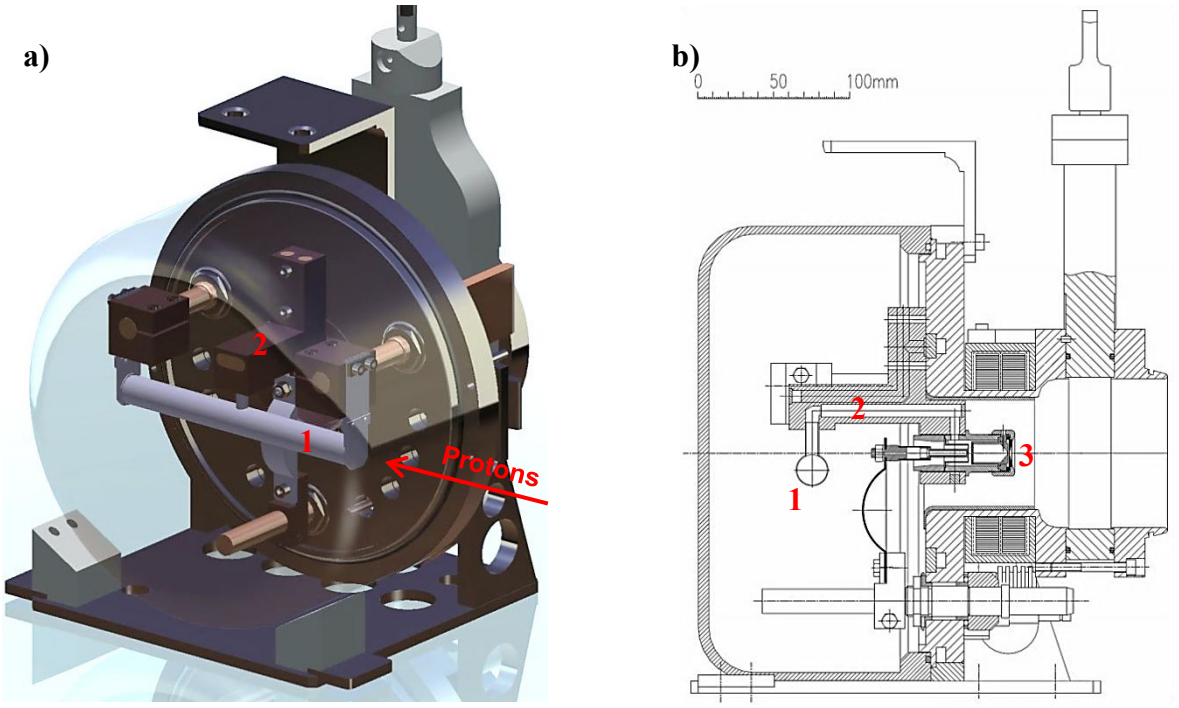

Figure I-4 – Target unit MK7 with VADIS ion source in 3D (a) and cut (b) – courtesy of Stefano Marzari. The numbers indicate the target container (1), the transfer line (2) and the ion source (3). The arrow indicates how the proton beam is made to collide with the target material, which is inside the target container.

As can be seen in Figure I-4, the ISOLDE standard target container has a cylindrical shape (200mm long, 20mm of diameter) and is made of tantalum, a refractory metal, which is then filled with the target material. To enhance the diffusion and effusion processes the target container can be heated by ohmic resistance up to 2200°C by providing

a current up to 1000A. As referred, a neutron field can be made by redirecting the proton beam to hit tantalum or tungsten rods, that are usually below the target (not present in the figure), serving as neutron converters.

The electrical connectors in both ends of the target container are specially designed to accommodate the thermal expansion of the target during its operation, reducing the mechanical stress on the target unit. The transfer line is the only opening of the target container through which the produced isotopes effuse to the ion source. By inserting cold parts into the hot transfer line some elements can be actively condensed or selectively adsorbed, providing a way to chemically select the reaction products that come out of the target.

Another very important part of the target unit is its ion source. Different ion sources can be mounted on the target for the best ionization efficiency, depending on the isotope to be ionized and its best ionization mechanism: (i) surface ionization, for elements with low ionization potential or high electrical affinity (for negative ion sources); (ii) plasma ionization, with a large efficiency but no selectivity; or (iii) resonant laser ionization for selective ionization of metallic elements. [24]

I.2.3 ISOLDE Pulse Shape

As soon as the proton beam hits the target, the isotopes produced through nuclear reactions, diffuse out of the material grains and desorb from the surface. Then, the species effuse through the porosity of the material (hitting the walls and being possibly adsorbed again) to the transfer line and then to the ion source where they are ionized. [25,26] The isotope release from the target after proton impact shows a sharp rise and a sudden fall, ending with a tail (see Figure I-5). The release can be defined as a probability function, *p(t)*, also called release curve or delay curve. To mathematically describe this behavior a three exponential function was chosen: [25]

$$p(t) = \frac{1}{Norm}\left(1 - e^{-\lambda_r t}\right).\left(\alpha e^{-\lambda_f t} + (1-\alpha)e^{-\lambda_s t}\right) \quad \text{(I.2)}$$

where t is the time, and λ_r (rise), λ_f (fast fall) and λ_s (slow fall) are three time-constant:

$$\lambda_x = \frac{\ln 2}{t_x} \quad \text{(I.3)}$$

α is a weighting factor between the slow and fast fallings components. In order to compare the release figures and their time constants, the integral of this function is normalized

(*Norm*) to 1. The fit function of equation (I.2) describes numerically the experimental curves, and its time parameters are not easily linked to specific physical phenomena.

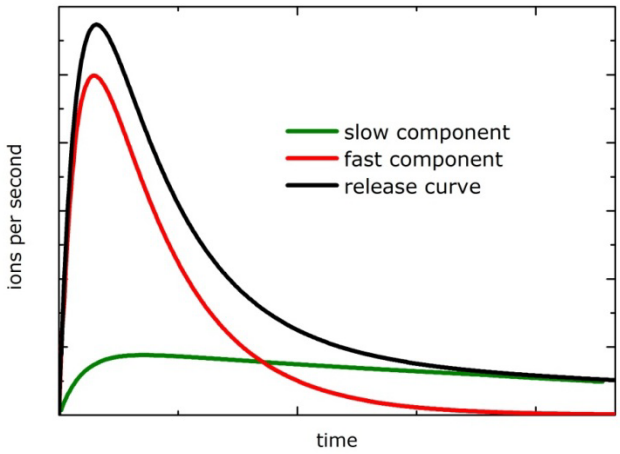

Figure I-5 - Theoretical release curve, where final release curve display a fast and a slow component (courtesy of Alexander Gottberg).

The intensity curve is calculated by multiplying equation (I.2) per N_0 which corresponds to the number of isotopes produced at t=0 (proton impact). The total yield is then calculated from the area under release intensity curve normalized to the proton current (ions/μC). [25]

To characterize the release characteristics, a useful parameter is the release efficiency (ε_{rel}). It is defined by the probability (dependent on half-life) that a certain isotope has to be released out of the target [27]. The release efficiency depends on each material, its respective operation temperature and of the target unit geometry. The release efficiency is lower for short-lived isotopes and approaches 1 for longer lived ones, since during effusion and diffusion delay processes part of what was produced, after the proton impact, is lost. The release efficiency is function of the isotope half-life ($T_{1/2}$) and is derived from equation (I.2) by the following relation:

$$\varepsilon_{rel}(T_{1/2}) = \int_0^{\infty} p_{\infty}(t) e^{-\frac{\ln 2}{T_{1/2}} t}\, dt \qquad \text{(I.4)}$$

where $p_{\infty}(t)$ corresponds to the release (equation (I.2)) for isotopes with $T_{1/2} \to \infty$, giving:

$$\varepsilon_{rel}(T_{1/2}) = \frac{1}{Norm}\left(\frac{\alpha}{\lambda_f + \lambda_i} + \frac{(1-\alpha)}{\lambda_s + \lambda_i} + \frac{-\alpha}{\lambda_f + \lambda_r + \lambda_i} + \frac{(\alpha - 1)}{\lambda_f + \lambda_r + \lambda_i}\right) \qquad \text{(I.5)}$$

where λ_i is the isotope decay constant:

$$\lambda_i = \frac{\ln 2}{T_{1/2}} \qquad \text{(I.6)}$$

I.3 Target Materials

For more than 40 years target materials have been developed at ISOLDE searching constantly for fast release properties in order to promote the production of exotic nuclei. [9] Different materials are used as ISOLDE targets either in solid or liquid state. The materials in solid state can be shaped as pressed pills, powders, fibers or foils of metals, carbides or oxides. The liquid targets are made of metals or salts of low melting points. Details about some of these materials can be seen in Table I-1.

Table I-1- Table with target materials most used at ISOLDE: T_m is the melting point temperature, T_{max} is the maximum operation temperature, p_{vap} is the vapor pressure, ρ is the theoretical density and ζ is the target thickness. [28]

Type	Material	T_m (°C)	T_{max} (°C)	p_{vap} Pa	ρ (g/cm^3)	ζ (g/cm^2)	Typical Isotopes
Metal	**Sn (l)**	232	1100	6×10^{-3}	5.5	110	$^{60-74}$Zn, $^{64-75}$Ga
	La (l)	920	1400	10^{-2}	6.2	124	$^{114-137}$Cs, $^{122-138}$Ba
	Pb (l)	328	800	10^{-1}	10.1	200	$^{177-207}$Hg
	Ti	1675	1600	2×10^{-1}	4.5	25	$^{37-46}$Ca, $^{42-48}$Sc
	Nb	2610	2050	3×10^{-4}	8.6	50	$^{70-85}$Br, $^{70-85}$Kr, $^{74-86}$Rb, $^{76-87}$Sr, $^{79-89}$Y
	Ta	2996	2200	5×10^{-5}	16.6	110	many
Carbides	**SiC**	2300*	1200	†	3.2	21	$^{17-23}$F, $^{18-24}$Ne, $^{20-24}$Na, $^{22-28}$Mg
	LaC_2	?	1750	2×10^{-1}	5.0	~30	$^{98-}$Cd, $^{100-114}$In, $^{104-}$Sn, $^{114-138}$Cs
	ThC_2	~2450	2200	2×10^{-3}	9.0	~50	many
	UC_2	~2450	2200	2×10^{-2}	11.3	~50	many
Oxides	**MgO**	2800	1500	5×10^{-1}	3.6	2.9	$^{17-24}$Ne
	CaO	2898	1400	$\sim10^{-2}$	3.3	5	^{6}He, ^{10}C, ^{17}N, $^{18-19}$Ne, $^{33-35}$Ar, $^{41-46}$Ar
	ZrO_2	2700	1850	$\sim10^{-2}$	5.9	6	Mn, Zn, Se, Kr, ^{56,71}Cu, $^{62-74}$Ga
	La_2O_3	2300	1300	$\sim10^{-2}$	6.5	64‡	$^{115-125}$Xe
	CeO_2	2600	1300	$<10^{-2}$	7.1	16	$^{112-125}$Xe, etc.
	ThO_2	3050	2100	2×10^{-2}	9.9	<30	many

Metals are used in form of foils or powders, creating target densities near one third of the bulk density. These forms are used to keep diffusion lengths short. Furthermore, diffusion in solid metals is slow for some elements so, often, oxides or carbides are preferred where higher temperatures can be applied. Although carbides are very stable, they are limited in operation temperatures by their vapor pressures or their level of impurities. The advantages and disadvantages of oxides are explained later in this work. [28]

Beyond solid targets, molten targets are also used at ISOLDE. These have a slightly different way of operation. They operate with larger pulse structure (3 bunches separated

* Decomposition temperature
† Impurity limited
‡ 400mm long target

by 16μs, instead of the normal set of 4 bunches separated by ~90ns) of the primary beam, that generate shockwaves in the molten material, promoting the release of the isotopes. [29] These targets produce RIBs of higher intensities of not too shorted-lived isotopes, due to their high densities. [28]

A solid material must fulfill several requirements to be selected as a target material for the production of RIBs at CERN-ISOLDE. The most important requirements and the ones that contribute more to the isotope release are the diffusion, effusion and adsorption.

For ISOL applications the best target microstructure was described before as the one having high open porosity (>30%) in the macrosize range (>100nm), nanosized grains, and stability at high temperatures. [7] Tortuosity should be minimized, and the pore size distribution must be narrow, minimizing the resistance to gaseous flow (effusion). [7,8]

Additionally, the surface area is a very important parameter to control. Nanometric scale materials with high surface area are envisaged, since not only diffusion lengths are shortened but also the release surface is increased. Nevertheless, a high surface area nanometric material will sinter at lower temperatures. Therefore, the temperature effect over time on the microstructure has to be well known (e.g. through sintering kinetics) in order to operate the target with temperatures high enough to promote diffusion and effusion phenomena but not degrade the microstructure of the material.

The production method of the target material defines the target final properties: different methods lead to different microstructures and different material properties.

In this section the most important properties will be described as well as their relation to the release process.

I.3.1 Diffusion

As diffusion remains one of the most important and most limiting factors involved in release properties from an ISOLDE target, it will be further detailed.

Fick's first law (in one dimension) is the simplest way of describing diffusion, for steady concentration conditions of the diffusing species: [30]

$$J_x = -D\frac{dC}{dx} \tag{I.7}$$

where J_x is the flux of the diffusing species, dC/dx is the concentration gradient and D is the diffusion coefficient. When concentration varies with time Fick's second law (also in one dimension) applies instead: [30]

$$\frac{dC}{dt} = D\frac{d^2C}{dx^2} \quad \text{(I.8)}$$

These laws can be used to determine the diffusion coefficient of a diffusing element in a host lattice from experimental data. To this end, a usual technique consists in the implantation of a radioactive isotope in a sample. Then, by heating at fixed temperatures for different delays, the diffusion coefficients can be determined as well as the diffusion pre-exponential factor (D_0) and the activation energy (Q).

I.3.1.1 Main Diffusion Mechanisms

The mechanisms of diffusion are the paths that the atoms preferably move in the crystal lattice. These are mainly influenced by the types of defects present in the material crystal lattice. The three principal mechanisms are: lattice diffusion (or volume or bulk diffusion), grain boundary diffusion, and surface diffusion. [30]

Lattice diffusion can occur either from a vacancy or by interstitial mechanism. Other mechanisms like interstitialcy and direct exchange (or ring mechanism) can also happen. Vacancies are part of the equilibrium point defects so they are always present in the material [31]. Their movement is in the opposite direction and the motion equivalent to that of the atom. The concentration of vacancies is determined by the temperature, solute and atmosphere. Another important mechanism is defined by atoms small enough to travel in the interstitial sites of the crystal lattice, which are said to move through the interstitial mechanism. Less important, interstitialcy mechanism happens when the distortion of the lattice is too large for the interstitial diffusion to happen. So a neighboring atom exchanges position with a lattice atom. The later, direct exchange or ring mechanism is defined by rotation of a group of atoms without participation of a defect. [30]

The grain boundaries of polycrystalline material are highly defective zones by nature. Because of that, grain boundaries are often zones of faster diffusion. This type of diffusion is dependent on the grain size, since higher grain sizes have reduced grain boundaries areas. [30]

Surface diffusion happens because the free surface of a solid is a perturbed region where kinks, edges, terraces and also vacancies and adatoms are formed. The migration of those last two is what provides the main mechanism of surface diffusion. [30]

I.3.1.2 Factors Influencing Diffusion

The diffusion coefficient depends greatly on the diffusing species, their concentration and the host material [31,32] and consequently on the diffusion mechanism [31].

The temperature has a large influence on the diffusion coefficients and diffusion rates. The diffusion coefficient varies with the temperature following an Arrhenius equation: [32]

$$D = D_0 exp\left(-\frac{Q}{RT}\right) \quad \text{(I.9)}$$

where D_0 is the temperature independent pre-exponential factor, Q is the activation energy for the diffusion (both dependent on the host material and diffusion species), R is the universal gas constant and T is the absolute temperature.

The type of the crystal phase (or lattice) of the host material is important in terms of atomic packing factor. For example, a face-centered cubic crystalline system has an atomic packing factor higher (0.74) than the body-centered one (0.68) so, typically, for the same host and diffusion species the diffusion coefficient is higher in the case of the later, because the atoms can move more freely. [31]

Diffusion is also influenced by defects present in the material crystal lattice. These defects influence transport phenomena, affecting for instance the rates sintering. [33] Proton irradiation is known to induce defects on the crystal structure such as voids, flaws and point defects, and this may affect the release processes by promoting diffusion [34]. Since at ISOLDE the proton beam is pulsed, this will induce high temperature spikes due to the deposited energy. These high temperatures, together with the temperature set in the target container, promote the annealing and sintering of the material. Therefore the best conditions in terms of temperature and proton intensity are those for which the microstructure is stable, defining the release properties achieved in operation over time. Only a post irradiation study would reveal the precise influence of all of these factors on the material microstructure [34].

I.3.1.3 Diffusion and ISOLDE Release Curve

Analyzing the ISOLDE release curve it is possible to obtain meaningful physical parameters about the release characteristics of the target material and also about the surrounding geometric components of the target. Effusion and diffusion time constants can be obtained through the release curve by using a model first proposed by R. Kirchner [27].

This model defines the probability of a given isotope to diffuse out of the material grains and effuse through the material porosity and to the ion source.

The effusion delay function, $p_v(t)$, can be defined analogously to the evacuation of a certain volume through an opening, which can be described by an exponential function [27]:

$$p_v(t) = ve^{-vt} \tag{I.10}$$

where v is an effusion delay parameter. The diffusion delay function, $p_\mu(t)$, was derived from Fick's Law for infinite foils of thickness d:

$$p_\mu(t) = \frac{8\mu}{\pi^2}\sum_{n=0}^{\infty} e^{-\mu(2n+1)^2 t} \tag{I.11}$$

where μ is the diffusion delay parameter, which can be related to a diffusion coefficient (D):

$$\mu = \frac{\pi^2 D}{d^2} \tag{I.12}$$

By a convolution of effusion and diffusion (equations (I.10) and (I.11)) the following equation, for the geometry of infinite foils, is obtained [27]:

$$p(t) = \frac{8\mu v}{\pi^2}\sum_{n=0}^{\infty} \frac{e^{-vt} - e^{-\mu(2n+1)^2 t}}{\mu(2n+1)^2 - v} \tag{I.13}$$

E. Bouquerel et al. [35] developed a more accurate equation for effusion delay function in an ISOLDE target unit by adding a second exponential function, to account for effusion of atoms from the target container to the ion source through a transfer line:

$$p_{v_1,v_2}(t) = \frac{1}{Norm}(1 - e^{-v_2 t})e^{-v_1 t} \tag{I.14}$$

where v_1 and v_2 are effusion time parameters. By convoluting equation (I.14) with (I.11), the following equation for effusion and diffusion was obtained:

$$p(t) = \frac{8\mu}{\pi^2}\sum_{n=0}^{\infty}\left[\frac{e^{-\mu(2n+1)^2 t} - e^{-v_2 t}}{v_2 - \mu(2n+1)^2} - \frac{e^{-\mu(2n+1)^2 t} - e^{-v_2 t - v_1 t}}{v_1 + v_2 - \mu(2n+1)^2}\right] \tag{I.15}$$

For the geometry of spherical particles, like powders, a diffusion delay function, $p_\mu(t)$ takes the form [36]:

$$p_\mu(t) = \frac{6\mu}{\pi^2}\sum_{n=1}^{\infty} e^{-n^2 \mu t} \tag{I.16}$$

where D is obtained with a equation similar to equation (I.12) from the particle radius, r:

$$\mu = \frac{\pi^2 D}{r^2} \tag{I.17}$$

A equation similar to the one obtained by E. Bouquerel et al. (equation (I.15)) can be derived for spherical particles by convoluting equations (I.14) and (I.16):

$$p(t) = \frac{6\mu}{\pi^2}\sum_{n=1}^{\infty}\left[\frac{e^{-n^2\mu t} - e^{-v_2 t}}{v_2 - n^2\mu} - \frac{e^{-n^2\mu t} - e^{-v_2 t - v_1 t}}{v_1 + v_2 - n^2\mu}\right] \tag{I.18}$$

The release efficiency, ε_{rel}, can also be related to physical phenomena like effusion and diffusion by the following equation, which was derived from the equation (I.18) similarly to the deduction of equation (I.5) [35,37]:

$$\varepsilon_{rel}(T_{1/2}) = \frac{3\mu(v_1 + v_2)v_2\left[\pi\sqrt{\frac{\lambda_i}{\mu}}\coth\left(\pi\sqrt{\frac{\lambda_i}{\mu}}\right) - 1\right]}{\pi\lambda_i(\lambda_i + v_2)(\lambda_i + v_1 + v_2)} \tag{I.19}$$

where λ_i is defined on equation (I.6).

The delay parameters of diffusion and effusion, v_1, v_2, μ can be deduced from the parameters in equation (I.18) or (I.19) by a fit to the experimental release curves. Determining μ and knowing the particle radius, one can extract the diffusion coefficient, D, through equation (I.17) and D_0 and Q values from equation (I.9) if measured for different temperatures.

The release efficiency can also be simply taken from the ratio between the yield observed experimentally (Y_{obs}) and the in target production yield (Y_{prod}), that would be obtained if the isotopes wouldn't decay over time. Y_{prod}, which is only mass dependent, can be obtained through simulations with programs like ABRABLA [38,39]. So, ε_{rel} can be obtained through the equation:

$$\varepsilon_{rel} = \frac{Y_{obs}}{Y_{prod}\varepsilon_{is}} \tag{I.20}$$

where ε_{is} is the ion source efficiency. From this using the release efficiency equation, deduced similarly to equation (I.5), from equation (I.16), just for diffusion, μ can be known [27]:

$$\varepsilon_{rel} = \frac{3\left(\sqrt{\lambda\pi^2/\mu} \times \tanh\sqrt{\lambda\pi^2/\mu} - 1\right)}{\lambda\pi^2/\mu} \tag{I.21}$$

This method is less accurate and underestimates μ since losses due to effusion are neglected.

Attempts to calculate the diffusion parameters and constants and/or activation energies from the detailed models have been successful in various works [27,35,36,40,41].

I.3.2 Effusion

After the isotope diffuses out of the target, effusion processes are responsible for transporting the isotope of interest to the ion source. Effusion can be defined as the molecular dynamics where a gas molecule doesn't hit another gas molecule. Effusion is mostly dependent on the temperature and on the target surface physico-chemical properties.

The effusion step is also dependent on the following parameters [27]: (i) the average number of collisions of the isotope with the surface of the target or the surrounding materials until it is ionized; (ii) the average sticking time in each wall collision, which is mainly dependent on the temperature and on the adsorption enthalpy of the target material or surrounding materials; (iii) and also the average flight time between each wall collision.

The defined parameters are very dependent on the type of materials that are chosen for the target unit. Furthermore, by increasing the temperature and reducing the total volume of the target the effusion speed is enhanced [7].

I.3.3 Other Important Material Requirements

Besides fast diffusion and effusion, other important characteristics for a target material must be considered and they are as S. Fernandes [7] described: high production cross section, high operational temperature, high resistance to radiation damage, high thermal conductivity and high resistance to fatigue, creep, thermal shock and corrosion.

A high isotope production cross section is related to the target material, the primary beam energy and is the probabilistic event of a certain nuclear reaction to occur. The amount of material exposed to the beam can be increased, increasing the production rate. [5]

One of the most important properties is the refractory characteristics of the material. A high operational temperature is required to reduce the time constants of the diffusion and effusion, and usually, the target temperature is set a few hundred degrees below the material melting point [4]. The maximum temperature is constrained by the evaporation of the target material and/or its impurities, degradation and sintering effects. The temperature is also limited by the vapor pressure of the material, which has to be

compatible with the ion source (less than 10^{-2} Pa), from which the ion source efficiency starts to fall [4].

Due to exposition of the target to high levels of radiation, high resistance to radiation damage of the material is needed. Radiation can induce changes in the physico-chemical characteristics (atomic, microstructural and electric, thermo-mechanical properties). These effects are dependent on the type, energy and the dose of particles which irradiates the material, its impurities, the surrounding atmosphere and temperature. Target deterioration by radiation is not a simple time effect. It mainly depends on the intensity of the beam, but on the bunch characteristics, which is deleterious for the target [20].

Both target material and target container must have a high thermal conductivity and high emissivity. When the primary beam pulse collides with the target, some fraction of energy is deposited in the target and in the target container, generating loads of high temperature in the target. Efficient cooling systems and good thermal conductance between the target and the container are needed for preserving the mechanical integrity of the target and also its microstructure. [5]

High resistance to fatigue, creep, thermal shock and corrosion is needed since the target is subjected to thermal gradients induced by the pulsed proton irradiation and ohmic resistance heating, thus requiring a high fatigue resistance. Fracture failure of the target can be induced by creep and corrosion in the target material.

I.4 Calcium Oxide Nanopowders

Since the early days of ISOLDE that ceramic powders or loose compacts have been used as target materials; firstly hydroxides (1970) [42], then oxides and carbides (1975) and later borides (1986) [43], since higher target temperatures could be reached.

Calcium oxide (CaO) has been used at ISOLDE for a long time, providing good yields of argon isotopes. Around 1 to 2 CaO targets are produced every year, representing 3.3% of the total ISOLDE RIB time – data from the last 5 years [44].

Alkaline earth materials are known for the production of good yields of noble gas isotopes through spallation nuclear reactions. [42] Calcium oxide is too corrosive to be used as a target material at high temperature directly in a tantalum (Ta) container, so it's covered, therefore protected, by a rhenium (Re) foil [43]. Submitted at high temperatures (>1050^{o}C), it gives fast release of some of the elements. Proton induced reactions of

spallation and fragmentation mainly produce the isotopes as showed from the ABRABLA simulation plot of Figure I-6 a).

This target is operated with a Versatile Arc Discharge Ion Source (VADIS) plasma ion source which is especially designed for the production of noble gas RIBs, when coupled via a cold transfer line (cooled by water) in order to trap condensable elements and improve the chemical selectivity [43]. The yields provided by the different CaO target units can vary by more than one order of magnitude, only the best historical values at ISOLDE are shown in Figure I-6 b).

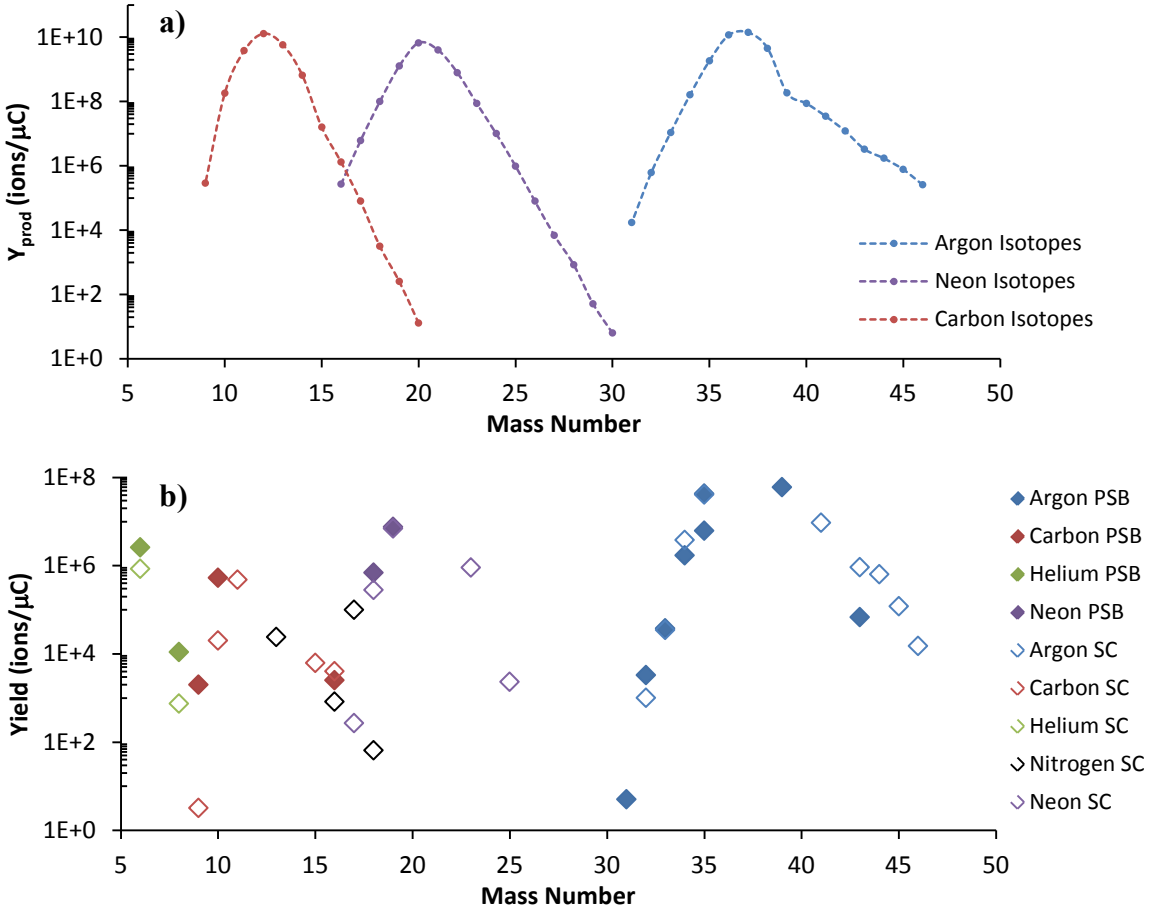

Figure I-6 – (a) Simulation of the ISOLDE in-target isotope production yields for calcium oxide material with a thickness of 7g/cm^2 done with ABRABLA. (b) Best historical experimental yields obtained by the CaO target material at ISOLDE. The filled marks were measured at the actual ISOLDE installations (PSB), the unfilled marks were measured in the old ISOLDE installation near the SC. [45]

At ISOLDE, as referred in the Introduction, CaO targets outperform other target material to produce similar beams but the material degrades in operation, either showing low yields from the beginning or a decrease over time. This effect is believed to be either due to sintering effects on the material due to high operation temperatures, to the proton pulses, or both.

Since CaO, as a target material, has never been characterized at ISOLDE, and the reduction of the grain size of other materials has been proved to enhance their release properties [8,7], the state of the art of calcium oxide nanopowders in terms of its production, reactivity in air and thermal behavior, is presented in the following sections, in order to provide a background for this study.

I.4.1 General Characteristics

Calcium oxide (CaO) is a white, refractory and alkaline crystalline solid at room temperature [46]. The Table I-2 summarizes the general characteristics of calcium oxide.

Table I-2 – General characteristics of calcium oxide. [47]

Molar weight	56.007g/mol
Physical form	Crystalline, cubic
Color	Gray-white
Melting point	2898°C
Density	3.34g/cm^3
Vapor Pressure [48]	1.49x10^{-6}Pa (1500°C)
Crystal System [48] **Space Group** [48] **Lattice constants** [48]	Cubic (NaCl) O_h^5 – Fm3m a=0.4799nm
Reactivity	Reacts violently with water forming calcium hydroxide. Soluble in acid solutions. Reacts with carbon forming carbide. [48] Reacts with CO_2 forming calcium carbonate. [48]

The calcium oxide (CaO) also called lime, calcia, quicklime or unslaked lime, has many uses in the current industrial world such as in mortars and cements, in the manufacturing of steel, plastic and glass, in food processing such as sugar refining, in disinfecting and disease control, in many chemical processes, as an absorbent, in water treatment, air pollution control as in flue-gas desulfuration and in agriculture for soil conditioning. [49,46]

Nanocrystalline CaO is also used, since its large specific surface and high interfacial energies have superior material properties required to improve the performance in many applications, especially in applications as catalysts, sensors and oxide dispersion strengthened alloys. [50]

CaO, as powder, is also very interesting as a target for proton irradiation for isotope production through the ISOL method, as referred before.

I.4.2 Calcination

The production of CaO through the decomposition of calcium carbonate ($CaCO_3$, calcite) has been object of study for the past 100 years [51]. The chemical decomposition reactions are within the most common solid state reactions. A different solid gas phases are produced by heating up another solid, producing simple oxides from carbonates, hydroxides, nitrates, sulphates and other metal salts. [30] The calcination, lately generalized to the chemical reaction between solids or decomposition of solids through heating, is the decomposition of the calcium carbonate, by supplying heat, into calcium oxide (CaO) and carbon dioxide (CO_2):

$$CaCO_3 \leftrightarrow CaO + CO_2 \qquad \text{(I.22)}$$

By having a look into the reaction thermodynamics, in Eq. (I.22), it is known that the reaction is strongly endothermic, because the calculated standard enthalpy of the reaction is high and positive, ΔH^o_R=42.6kcal/mol [52]. From the calculation of the Gibbs free energy change from the reaction, the temperature at which the $CaCO_3$ begins to become unstable can be known. Equivalent information can be taken from data of the partial pressure of the gaseous product – CO_2 (p_{CO_2}).

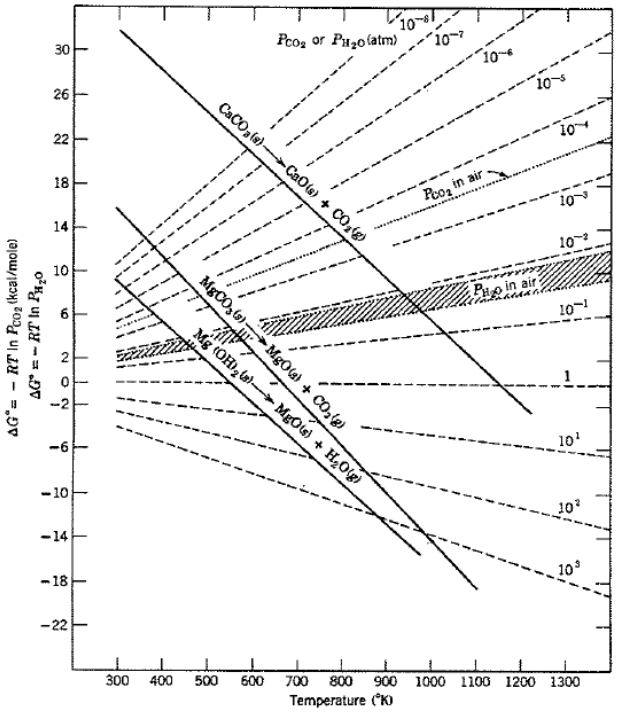

Figure I-7 - Standard free energy of a reaction in function of the temperature. The dashed lines represent the equilibrium of the gas pressure above the reactions. [30]

A graphic representation of the variation of the Gibbs free energy with temperature and the equilibrium gas pressure can be seen in Figure I-7. This figure is a very important theoretical asset for this work since from it, one can assess the theoretical temperature at which the $CaCO_3$ starts to decompose at a specific partial pressure of CO_2. This can be done by drawing a vertical line which intercepts the point where the $CaCO_3$ reaction line meets the dashed line of the determined p_{CO_2}. It can be seen that, for the decomposition in air, the reaction starts at ~800°C, whereas for reduced CO_2 pressures, lower temperatures are required. For instances, when p_{CO_2}=10^{-7}atm (10^{-2} Pa) the reaction is shifted to ~610°C.

To achieve the desired properties and a high quality oxide product, a precise control of the $CaCO_3$ thermal decomposition is necessary. The characteristics of the precursor, such as the particle size, porosity, purity, calcination temperature, holding time and CO_2 pressure all influence the final characteristics of the synthetized CaO. [49] An understanding of these factors along with their influence on the kinetics of the reaction is, therefore, important and has been undertaken in various works which will be reviewed here.

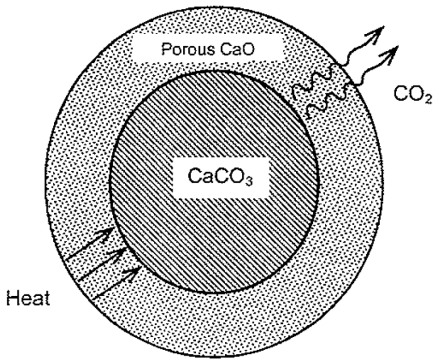

Figure I-8 - Representation of the $CaCO_3$ decomposition and the formation of the porous layer of CaO. [30]

In this heterogeneous reaction, as the molar volume of the solid reaction product (CaO) is less than the one of the reactant ($CaCO_3$), the product forms a porous layer around the nonporous reactant core, which interface moves inward [30]. This is also called the calcination shrinking core model, illustrated in Figure I-8 [53]. The kinetics of the reaction can be either controlled by the reaction at the interface between the CaO and the $CaCO_3$, by heat transfer to the reaction or gas diffusion (or permeation) from the reaction surface through the porous product layer [30].

The difference between the molar volumes indicates that the CaO should have a porosity around ~55% for the CaO produced from $CaCO_3$ and around 50% for the one produced from $Ca(OH)_2$, but slightly lower porosities (~15% less) in both cases were

obtained by D. Beruto et al. [54]. This means that the calcite particle aggregates must experience some shrinkage due to sintering effects during the decomposition step [55]. This can either be due to sintering of $CaCO_3$ before or of $CaCO_3$/CaO during the decomposition, or both [56,57].

Through the last decades an effort has been made to understand the kinetics, mechanism, and the rate limiting step of the decomposition reactions under different conditions to create adequate kinetic models. However, no agreement among authors has been reached, specifically in the case of the decomposition reactions to obtain CaO, which is by far the most studied one. [49,58] Studies on the decomposition of $CaCO_3$ and $Ca(OH)_2$ powders or large single crystals in some various atmospheres, have been made, as summarized in the Table I-3.

The kinetics of the $CaCO_3$ decomposition follows a linear law accordingly to the geometrical model of the contracting thickness: [30]

$$w = k_r t \tag{I.23}$$

where w is the weight loss, k_r is the rate constant and t is the time. This relation is verified experimentally in several works [49,51,58-61].

I.4.2.1 Effect of the Atmosphere and Temperature

In 1958, D. Glasson [56] first reported that CaO produced through decomposition of micrometric $CaCO_3$ powders in vacuum yielded higher surface areas than in air. It is by creating non-equilibrium conditions that the reaction of the equation (I.22) is shifted to the right hand side promoting the fast nucleation of CaO [57] and thus the formation of very small crystallites. Several other studies, resumed in Table I-3, report the obtainment of nanocrystalline CaO and decomposition reactions happening at much lower temperatures than the decomposition in air. For example, D. Beruto et al. [54] reported complete decomposition of $CaCO_3$ micrometric powder (3 to 10 μm) at only 510°C under $7x10^{-4}$ Pa ($7x10^{-9}$ atm), to give 15 nm crystallites of CaO with 78 m^2/g of specific surface area. This is coherent with Figure I-7, where thermodynamically, for p_{CO_2}=10^{-8} atm) the reaction happens at less than 600°C. Furthermore, E. Powell and A. Searcy [61] report decreasing surface areas for increasing temperatures of decomposition.

In most of the studies, the obtained CaO crystallites are too small to be analyzed by SEM and the characterization of CaO powders for Transmission Electron Microscopy

(TEM) is difficult mostly due to the powder instability in air atmosphere [61]. K. Towe [64], A. Singh et al. [50] and C. Rodriguez-Navarro et al. [49], could analyze the nanostructured CaO by decomposing $CaCO_3$ *in situ* in a Transmission Electron Microscope, with the electron beam under vacuum. The type of used energy to decompose the $CaCO_3$ (electron irradiation or heat) was reported to have not a significant influence on the decomposition mechanism. [49] K. Towe [64] and C. Rodrigez-Navarro et al. [49] observed rod-shaped nanocrystallites with preferred orientations, produced from large calcite single crystals, with dimensions of about 10x100 nm and 5-10x25-75 nm, respectively. The later could also determine the pore size, from 5 to 10 nm. A. Singh et al. [50], instead of using large calcite crystals, as in the previous studies, used a calcite micrometric powder and observed plate-like nanocrystals of calcia with 5-10 nm and preferred orientations.

Table I-3 – Summary of precursors form, calcinations conditions and CaO powders characteristics reported in the open literature.

Author	Raw material	T (ºC)	Atmosphere	SSA (m^2/g)	XS (nm)
D. Glasson [56]	$CaCO_3$ powder (2.5 m^2/g)	800	Vacuum	43.2	-
	$Ca(OH)_2$ powder (4.9 m^2/g)	400		85.4	-
D. Beruto et al. [54]	$CaCO_3$ powder (1 to 10 μm)	510	Vacuum ($7x10^{-3}$ Pa)	78	15
	$Ca(OH)_2$ powder (1 to 10 μm)	320		133	12
	$CaCO_3$ single crystal	580		89	-
	$CaCO_3$ powder (1 to 10 μm)	400	Dry N_2	2-4	38
		900	Air	1-2	-
E. Powell and A. Searcy [61]	$CaCO_3$ single crystals (>1 cm)	650 to 900	Vacuum (10^{-2} Pa)	60 - 127	-
D. Beruto and L. Barco [62]	$CaCO_3$ single crystals (1 mm)	686	Vacuum (10^{-4} Pa)	116	-
G. Spinolo and U. Anselmi-Tamburini [55]	$CaCO_3$ powder (5 to 30 μm)	547	Vacuum (10^{-2} Pa)	79	13.5
			Vacuum (10^{2} Pa)	54	25
		597	Vacuum (10^{-2} Pa)	82.5	16
			Vacuum (10^{2} Pa)	39	31.5
			Air	12	95.5
S. Dash et al. [51]	$CaCO_3$ powder (40 μm)	1000	Vacuum (10^{-5} Pa)	-	17
		1200	Vacuum (10^{-5} Pa)	-	47
J. Ewing and D. Beruto [63]	$CaCO_3$ powder (3 μm and 0.7 m^2/g)	650	Vacuum ($1,3x10^{-3}$ Pa)	93.6	-
			13.3 Pa of CO_2	69.3	-
			120 Pa of CO_2	51.7	-
			133 Pa to 800 Pa of CO_2	>50	-

The presence of background pressures of CO_2 (up to ~130 Pa) was studied by J. Ewing and D. Beruto [63] and was reported to influence the decomposition reactions of

$CaCO_3$ by means of decreasing the surface areas, increasing the crystallinity of CaO produced, with the increase of p_{CO_2} (for values, see Table I-3). He also reported that sintering happened already at 650°C, for 1200Pa of CO_2 pressure, and the resulting CaO particles showed coalescence, dimpling and rounding. The effect of CO_2 in sintering will be better detailed ahead.

Decomposition of $CaCO_3$ under N_2 atmospheres showed microstructures and morphologies identical to those observed in air decomposition. These microstructures showed rounded grains and coalescence between them. This was observed by J. Ewing, D. Beruto [63], M. Maciejewski and R. Oswald [57]. The former attributes this result to the partial increase of the CO_2 pressure in the decomposition atmosphere up to values comparable to those attained in air decomposition.

I.4.2.2 Influence of the Precursor

Calcium oxide has been obtained by decomposition of micrometric powders of $Ca(OH)_2$ and $CaCO_3$ in vacuum by D. Glasson [56] and D. Beruto et al. [54] They both report higher surface areas in the case of decomposition of $Ca(OH)_2$ comparing with the decomposition of $CaCO_3$. Furthermore, D. Beruto et al. [54] reported that the reaction is pseudomorphous for the decomposition of both precursors. This author obtained calcia particles with different porosities for different precursors (higher in case of decomposition from $CaCO_3$, because the molar volume of water is less that the molar volume of CO_2.

In other study done by D. Beruto and A. Searcy [60] the morphology of the obtained calcia particles from calcite large single crystals as precursors, was studied. Two microstructures were reported to be present in the obtained CaO crystals: an inner layer of about 10 to 50 μm, made of rods typically separated from their neighbors by very small pores, and an outer layer where the rods are typically collapsed into bundles of ~1 μm cross section separated by ~1 μm pores. This indicates that the outer layer, which is an open structure of the inner unbundled rods, is mechanically unstable and that strains can be induced in it. It is thought that this strain is due to the low mobility of the CaO species in the reaction interface. [58] The transition between the two layers lead to changes in the pore size and distribution as suggested by E. Powel and A. Searcy [61] and later proved by D. Beruto [62]: the transition happens, when the intermediate layer has more than ~10 μm, by difusionless repacking into bundles, reducing the surface area and creating a duplex pore

structure, with the larger pores being in the micrometric range. A consequence of this type of structure, with bimodal pore-size distribution, is that by heating, coarsening with very little shrinkage is observed, with decrease in the mesopore* volume being balanced by increase in the macropore* volume [65].

In the case of decomposition of micrometric calcite particles, no macropores are observed in CaO. This proves that re-packing into bundles is size dependent. The strain accumulates on the calcite-CaO rod interfaces, but when the stress exceeds a critical value the mechanical stability of the CaO aggregate is broken. The formation of macropores is thought to relieve the stresses. The CaO produced from small calcite particles does not reach this critical level of stress. [58]

I.4.3 Reactivity in Air

Calcium oxide produced from powders or single crystals in vacuum is very reactive and hydrates very fast compared to the ones produced in air. [66] This very high reactivity is due to their higher surface areas because of high porosity and low crystallite size. There is also evidence that this product (the formed hydrate) is nanocrystalline and forms instantaneously when high reactive CaO is exposed to air. [51]

There are three possible reactions (I.24),(I.25) and (I.26), that can happen when CaO is exposed to air:

$$CaO + H_2O \leftrightarrow Ca(OH)_2 \quad \text{(I.24)}$$

$$CaO + CO_2 \leftrightarrow CaCO_3 \quad \text{(I.25)}$$

$$Ca(OH)_2 + CO_2 \leftrightarrow CaCO_3 + H_2O \quad \text{(I.26)}$$

Which reaction happens will be decided not only by thermodynamics but also by kinetic factors. The calculated standard free energy for the reactions (ΔG^o_R) in equations (I.24), (I.25) and (I.26) are respectively -15.8 kcal mol^{-1}, -31.2 kcal mol^{-1} and -15.4 kcal mol^{-1}. [52] These values show that the reaction is spontaneous in all the cases (the more negative the more spontaneous). The calculated standard enthalpy of the reactions (ΔH^o_R) in equations (I.24), (I.25) and (I.26), are respectively -26.8 kcal mol^{-1}, -42.6 kcal mol^{-1} and -15.9 kcal mol^{-1}, showing that all the reactions are exothermic [52].

* Accordingly to the International Union of Pure and Applied Chemistry (IUPAC), the pore size is defined in three categories: micropores have less than 2nm, mesopores have between 2 and 50nm and macropores have more than 50nm. [62]

Hydration studies in CaO shows that this step leads to loss of specific surface area and increase in particle size, due to agglomeration [56] and to an increase of volume almost to double, creating internal strains in the material [67]. The roughness is reported to increase with the time of exposure to moisture [68]. A study reports that just by quick transferring a high surface area CaO (78 m^2/g) from the decomposition furnace to a thermogravimetry apparatus, caused sample hydration to an extent of 15 to 18% [54]. The hydration resistance of CaO sintered samples is reported to be enhanced with the sintering temperature. [69]

While the hydration is reported to almost double the volume, the carbonation is reported to only increase the later by 12%. The number of crystallites formed by carbonation is lower than by hydration. [70] The carbonation proceeds to the interior of the particle by an advancing interface. The newly formed $CaCO_3$, starts to inhibit the progress of the reaction because of its very low porosity which implies a large loss of surface area. [71] This finding has been studied in order to improve the hydration resistance of CaO by forming a layer of the carbonated product. [72]

With the increasing interest for the greenhouse effect over the last years, there has been several studies defending the use of calcium oxide for high temperature CO_2 sequestration and its performance after several cycles of decomposition and carbonation.

I.4.4 Sintering of Calcium Oxide

Sintering is a processing technique which is used to produce density controlled materials and components from ceramics or/and metal powders by applying thermal energy. It is a process that is influenced by the powder and compact characteristics (impurities, morphology, particle size distribution, agglomeration, green density, etc.) and by the sintering conditions (heating and cooling rates, maximum temperature, holding time, pressure, atmosphere, etc.). [33] The solid state sintering comprises three main phases: (i) the initial stage, which is characterized by rapid inter-particle neck growth and corresponds to shrinking values up to 3%, (ii) the intermediate stage which goes until 90-95% of the theoretical density and is characterized by continuous pore phase at an equilibrium of their shape, and (iii) the final stage for densities higher than 95% and the goal is to remove all porosity ending most of the times as isolated pores. [30]

The mechanisms of sintering in polycrystalline ceramics are the paths through which transport of matter happens. This happens from regions which have higher chemical

potentials towards regions with lower chemical potentials. [30] At least 6 mechanisms of sintering exist in solid state sintering and they are illustrated in the Figure I-9.

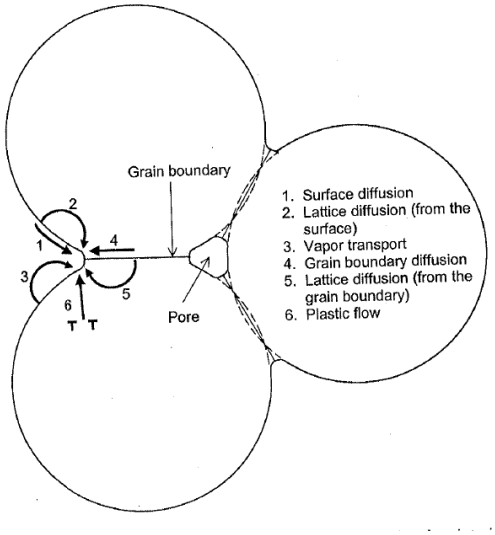

Figure I-9 - Mechanisms of solid state sintering. Only 4 to 6 cause densification, but all cause neck growth influencing densification. [30]

The specific surface area is a much sensitive parameter in the evaluation of sintering and can be used for studying the kinetics of the initial sintering. The following equation was proposed in a model developed by R. German and A. Munir [73] for the surface area reduction in the initial stage sintering, under isothermal conditions:

$$\left(\frac{\Delta S}{S_0}\right)^{\gamma} = kt \tag{I.27}$$

where S is the surface area, S_0 is the initial surface area, γ is an exponent related to the sintering mechanism, t is the time and k can be expressed as:

$$k = \frac{k_0 e^{-\frac{Q}{RT}}}{r^m T} \tag{I.28}$$

being k_0 a constant term of a given material, Q the activation energy, R the gas constant, T the temperature, r the particle radius, and m the Herring scaling exponent. This kinetic model is also called the German and Munir model. It is only valid for $\Delta S/S_0<0.5$, until necks start to touch each other, marking the end of the initial stage sintering. There are also other assumptions like dense and spherical monosized particles.

Shrinkage is another kinetic parameter for the first stage of sintering and the following equation was derived, under isothermal conditions [33]:

$$\left(\frac{\Delta l}{l_0}\right)^s = k_s t \qquad \text{(I.29)}$$

where l is the length of the pellet, l_0 is the initial length, s is an exponent related to the sintering mechanism, t is the time and k_s a constant containing material and matter transport terms.

The theoretical values of γ are shown in the Table I-4, for different particle coordination numbers, related with the particle packing, and for different sintering mechanisms. Theoretical values of the exponent s can also be seen in the same table.

Table I-4 – Kinetic exponents for surface area and shrinkage in initial stage models. [33,73]

Mechanism	Densification	γ (N_c fractional density)			s
		4 (0.32)	7 (0.60)	10 (0.68)	
Viscous or plastic flow	Yes	1.1	1.1	1.1	1
Evaporation-condensation	No	1.6	1.5	1.4	-
Volume diffusion	Yes	2.7	2.7	2.7	2
Grain-boundary diffusion	Yes	3.3	3.3	3.2	3
Surface diffusion	No	3.6	3.5	3.4	-

The sintering of calcium oxide powders having high specific surface areas was investigated taking as variables the oxide precursors [74,75,69], either the carbonate or the hydroxide and the sintering atmospheres: air [75,69], N_2 [74], H_2O and CO_2 [76].

W. De Keyser et al. [75] studied CaO sintering in air atmosphere, reporting much higher sintering speeds of CaO produced from $Ca(OH)_2$, C_H, than from $CaCO_3$, C_C, both calcined at 1000°C (C_H precursor was 0.45 μm and C_C was 2.7 μm particle size powders). Main shrinkage is observed in both cases after 1100ºC, and for the CaO produced from $Ca(OH)_2$ shrinkage is much higher than the one produced from $CaCO_3$ case. It is suggested that the production of CaO from the hydroxide introduces in the CaO lattice a large number of excess vacancies. These vacancies enhance the mater transport during the sintering process.

R. Borgwardt [74] investigated the sintering of high surface area CaO powders produced from $CaCO_3$ (S=104 m^2/g) and $Ca(OH)_2$ (S=76.7 m^2/g) in a flowing N_2 atmosphere. The reduction SSA was followed between 700°C and 1100°C and the kinetic analysis, using the German and Munir model [73], was applied. The calculated average γ exponent value of 2.7, agreeing with lattice diffusion as sintering controlling mechanism. The C_H, also showed in this study, a much faster sintering rate than C_C which was

attributed to its lower porosity, leading to a denser compact with more contact points between the particles. Finally, by decomposing $CaCO_3$ pure and with impurities he observed a higher sintering rate for the latter, which was explained by the effect of impurities creating lattice defects and therefore, accelerating solid-state diffusion processes.

R. Borgwardt [76] also studied the influence of presence of H_2O and CO_2 in the sintering atmosphere of the same CaO powders used in the previous study [74], from 350°C to 1150°C, and partials pressures up to $1.5x10^3$ Pa of H_2O and up to $1.2x10^3$ Pa of CO_2. Both types of gas are reported to strongly catalyze the sintering process and, furthermore, their effects are additive. The kinetic analysis taking the German and Munir model [73] couldn't identify the mechanism, since the values of γ exponent increased by increasing H_2O or CO_2 pressure and the values are higher than the theoretical ones, in Table I-4. Other mechanisms, than lattice diffusion may be operating and it was proposed that the presence of CO_2 and H_2O on free surfaces and interfaces activates the surface and grain boundary transport.

D. Beruto et al. [65] studied the influence of the CO_2 pressure in the sintering of CaO with ~120 m^2/g. He observed that a CO_2 pressure around 1330 Pa greatly increases the sintering of CaO at a low temperature of 686°C which is in accord with the activating effect of CO_2 in the matter transport for sintering also reported by R. Borgwart [76]. The surface area reached more than 50% of reduction after 10h, at this temperature.

Chapter II - Experimental Procedure

II.1 Characterization Techniques

The different techniques and experiments used for material characterization, both in University of Aveiro and CERN will be shortly described in this section.

II.1.1 X-Ray Diffraction - XRD

X-Ray diffraction was a very useful technique in this work, enabling a qualitative analysis of the crystalline phases in the powder and pre-sintered samples. The determination of the crystallite size was done using this technique.

By exposing a crystalline sample to a X-ray beam, some of those X-rays are diffracted according to a certain angle (2θ) matching characteristic crystallographic directions of the material as given by the Bragg's Law [31]. This diffracted X-rays are detected, generally, by a moving counter in a goniometer, giving origin to more counts at the certain angles, producing peaks in a plot of counts per second versus the diffraction angle (2θ).

At the University of Aveiro, the equipment used was a *Rigaku® D/Max-B* with an X-ray source ($\lambda CuK\alpha$=1.54056Å), in which a potential of 40kV and a current of 30mA is applied. Another similar equipment, at CERN, *Siemens D-5000 Diffractometer*, was used. The tests were done by grinding, when needed, the samples to powder in an agate mortar. The sweeping angles used were from 10°2θ to 80°2θ and a step of 0.02 °2θ, with a speed of 3°2θ/s was used. This equipment is connected to a computer which records the results and helps in the phase identification through the X-ray diffraction peaks. For this, in the case of the *Rigaku® D/Max-B,* a software named *Jade (version 9.3.4 – 05-02-2011)* was used which has an integrated database of Powder Diffraction Files (PDF) from the International Center of Data Diffraction (ICDD). For the *Siemens D-5000 Diffractometer* a software named *TOPAS P v2.0* was used.

Through the broadening of the X-ray diffraction peaks, crystallite sizes of less than ~0.1μm can be conveniently measured. [30] The crystallite size is given by the Scherer equation: [77]

$$\beta = \frac{K\lambda}{G\cos\theta} \qquad \text{(II.1)}$$

where β is the breadth usually expressed as the full width at half maximum (FWHM), θ is the diffraction angle, λ is the wavelength of the X-rays, G is the crystal size and K is a

constant to account for particle shapes (close to unity, usually 0.9). The broadening is also affected by instrumental factors. Such factors have to be subtracted to correctly calculate the crystallite size. To measure the instrumental broadening a macrocrystalline material in which the broadening is negligible can be used. [77] In this case, the instrumental broadening was determined with a macrocrystalline lanthanum hexaboride (LaB_6).

To measure the FWHM a mathematical treatment has to be done to the diffractograms peaks. There are 4 empirical peak shape functions: Gauss, Lorentz, Pseudo-Voigt which is a convolution from the last two and Pearson-VII. The latter two are the most used, [78] and accordingly the mathematical treatment was done using the software *Jade* or *TOPAS* with the Pearson-VII to do the fitting. The peaks were considered to be symmetric and to subtract the background a 4th order polynomial function was chosen.

II.1.2 Surface Area and Porosity Measurements through Isotherm Determination – BET/BJH

Adsorption measurement based on the Brunauer, Emmet and Teller (BET) isotherm is a method commonly used to determine the specific surface area (SSA) of a powder or porous material. [79]

This measurement is done at 77K in which N_2 adsorption, the most common gas used in BET, is easier to measure. By putting a solid of a known mass in contact with a known volume of gas, it adsorbs creating a decrease in the pressure, from which the amount of adsorbed gas can be calculated. From this measurements a plot of the amount of gas adsorbed versus the relative pressure (p/p_0, p_0 being the saturation vapor pressure of the adsorption gas used) is represented, which is called the adsorption isotherm. The BET equation that can be applied to the isotherm curve, which is only valid for lower values of p/p_0 (usually between 0.05 and 0.3) and is used in this form: [79]

$$\frac{p}{V(p_0 - p)} = \frac{1}{V_m C} + \frac{C - 1}{V_m C}\frac{p}{p_0} \qquad \text{(II.2)}$$

where V is the volume of gas adsorbed, V_m is the monolayer volume and C is a constant. By this procedure the V_m can be calculated (from the slope and the intercept) and applied in equation (II.3) to calculate the surface area: [79]

$$S = \frac{N_A \sigma V_m}{V_0} \qquad \text{(II.3)}$$

where the S is the surface area, N_A is the Avogadro number, σ is the area of an adsorbed gas molecule and V_0 is the volume of 1mol of gas at STP (Standard Temperature and Pressure).

The average particle size (G_{BET}) of a powder can also be known, assuming a certain particle shape, and dense and unagglomerated particles, by the following equation: [80]

$$G_{BET} = \frac{f}{S \times d_S} \quad \text{(II.4)}$$

where d_s is the theoretical density of the solid material and f is a particle shape factor defined in Table II-1.

Table II-1 – Shape factors and respective packing fractions for different powder geometries. [80]

Powder Shape	Shape factor, f	Packing fraction
Sphere	6.0	0.60
Ellipsoid (1:2:4)	7.6	0.52
Cylinder (1:1)	6.0	0.61
Cylinder (1:2)	5.0	0.60
Cylinder (1:10)	4.2	0.48
Cube	7.4	0.72
Parallelepiped (1:4:4)	9.4	0.68
Flake (1:10)	24	0.55

The very initial part of an isotherm and its end may also give information about the material porosity. There are 6 different main types of the isotherms accordingly to Brunauer, Emmet and Teller. [30] The different isotherms represent different properties of a material, also the different type of hysteresis on adsorption and desorption measurements reveals much about the type of porosity. From the isotherms the pore size distribution (PSD), pore volume and pore area can be obtained, using either the nonlinear high p/p_0 zone of the isothermal or the low one, through methods such as the t-plot (for microporosity area) and the Barret-Joyner-Halenda method (BJH) for the PSD, pore volume and pore area. For further reading refer to the bibliography. [81,79]

The equipment used was a *Micromeritics® – Gemini 2370 V5*, in the University of Aveiro, and a *Quantachrome® eNOVA2200*, at CERN, which both use N_2 as the adsorption gas and liquid N_2 to cool down the samples.

Before every test the samples were degased at 200°C for 4-6h in flowing nitrogen.

II.1.3 Differential Thermal and Thermogravimetric Analysis – DTA/TGA

Differential Thermal Analysis (DTA) is a technique that permits to know the thermal behavior of a material and the transformations it goes through.

This is done by heating up the material, registering the temperature difference against an inert material (reference, normally pure alumina), which is being heated simultaneously. The temperature difference (in μV) is then plotted against the temperature of the furnace and positive differences between them indicating exothermal transformations or negative ones, endothermic transformations.

It's usual in this kind of tests to record the weight variation during DTA test, which technique is called thermogravimetric analysis (TGA). This provides additional information about the transformation that is occurring, by overlapping the weight loss curve (TGA) with temperature to the thermal energy curve (DTA).

The equipment used was a *Shimadzu® TGA-50*. It's a DTA/TGA equipment with the capability of doing the tests under a flowing gas of choice. The tests were done under flowing Argon. All tests were done in the same conditions: heating from room temperature to 1000^{o}C at a rate of 10^{o}C/min.

II.1.4 Scanning Electron Microscopy – SEM/STEM

The scanning electron microscopy (SEM) is a widely used technique to study the microstructure and morphology of materials. An electron gun generates a beam of electrons inside a vacuum column which is then focused and driven to collide with a target, the sample. An image is possible due to the electronic signal generated by the low angle backscattered electrons, which are created by electron interactions with the material surface. [31]

The SEM equipment used was a *Hitachi® model SU-70*, in the University of Aveiro, that has a maximum electron acceleration potential of 30 kV, a point-to-point resolution of 1 nm at 15 kV and an energy dispersive X-ray spectrometer (EDS). This equipment also permits transmission electron microscopy by putting a detector below the sample. This technique is often called scanning transmission electron microscopy (STEM).

The powder samples were prepared by making a diluted suspension of powder in pure ethanol (99%) followed by deposition of a drop in a copper micrometric grid. The

support was then put inside the microscope before the drop dried to minimize the powder contact with air. Both SEM and STEM observations were done.

To observe the thermal treated pellets, they were fractured and put on carbon tape and then coated with gold to make them conductive and prevent hydration. [62,63]

At CERN, SEM was done in a *Link Leo Oxford Instruments*®, *model LEO 430I*. This microscope has a maximum resolution of 4 nm and an electron potential acceleration up to 40 kV. It is also equipped with EDS. The same sample preparation techniques were used but instead of a cooper grid, carbon tape was used.

II.1.5 Transmission Electron Microscopy - TEM

Transmission electron microscopy (TEM) has the same operation principle of SEM (see section II.1.4), but in this case the electrons are accelerated at a much higher potential to pass through the sample towards the detector below it. The electrons, passing through the sample, which has to be very thin to allow it, are either absorbed or dispersed changing their directions. This dispersion is influenced by the atomic arrangement of the material. Afterwards they are focused again, amplified and projected in a fluorescent screen or in a monitor. [31]

TEM was done in a *Hitachi® model 9000*, in the University of Aveiro, with an acceleration potential of 300 kV. The samples for TEM were prepared by depositing a drop of a diluted powder suspension in pure ethanol (99%) in a micrometric copper grid. After drop dried, the grid was inserted in the support of the TEM sample chamber.

II.1.6 Tape Station – Release Curves Measurement at ISOLDE

In order to measure the yield and the release curve of a specific isotope, a device called tape station is used. This device transports implanted isotopes from the beam towards $\beta(\alpha)$ and γ detectors. They are made of a plastic scintillator in the case of detector for β particles and a Germanium crystal for γ detection.

A release curve and yield are characteristic of a defined isotope and target unit. In order to accurately measure those, the beam has to have a high isotope to background noise ratio. The background is referred as being other isotopes produced and/or radiation resulting from the experimental hall or natural radiation. By increasing the isotope to

background ratio, the background can be minimized until a point where the decay detected can be assumed to be all resulted from the isotope being produced.

The tape station has two detectors and a metallic mylar tape that moves the atoms collected for a certain time ($t_{collection}$) to a measurement zone where the decay is measured for defined time ($t_{measurement}$). By separating the measurement zone from the detection zone an adaptable system is obtained. Either high beam intensities which would saturate the detectors can be measured by reducing the $t_{measurement}$ or the $t_{collection}$, or low beam intensities in which to get some statistics those times have to be increased. In Figure II-1 a), the different elements of a tape station can be seen.

The obtained values have to be corrected for the losses of isotopes during all this processes, if they have short half-lives, in such a way that this corresponds to the release curve of the isotope right after its production. For this $t_{collection}$, $t_{measurement}$, t_{delay} and the time that the tape takes to transport the atoms from the detection zone to the measurement zone ($t_{transport}$) have to be recorded. This curve is then fitted and corrected by a dedicated program to get the time constants from equation (I.2) from the pulse shape and then finally, the yield. The process of the obtainment of the beam and its way to the tape station can be seen in Figure II-1 b) and the steps for the measurement of a release curve are schematized in Figure II-1 c).

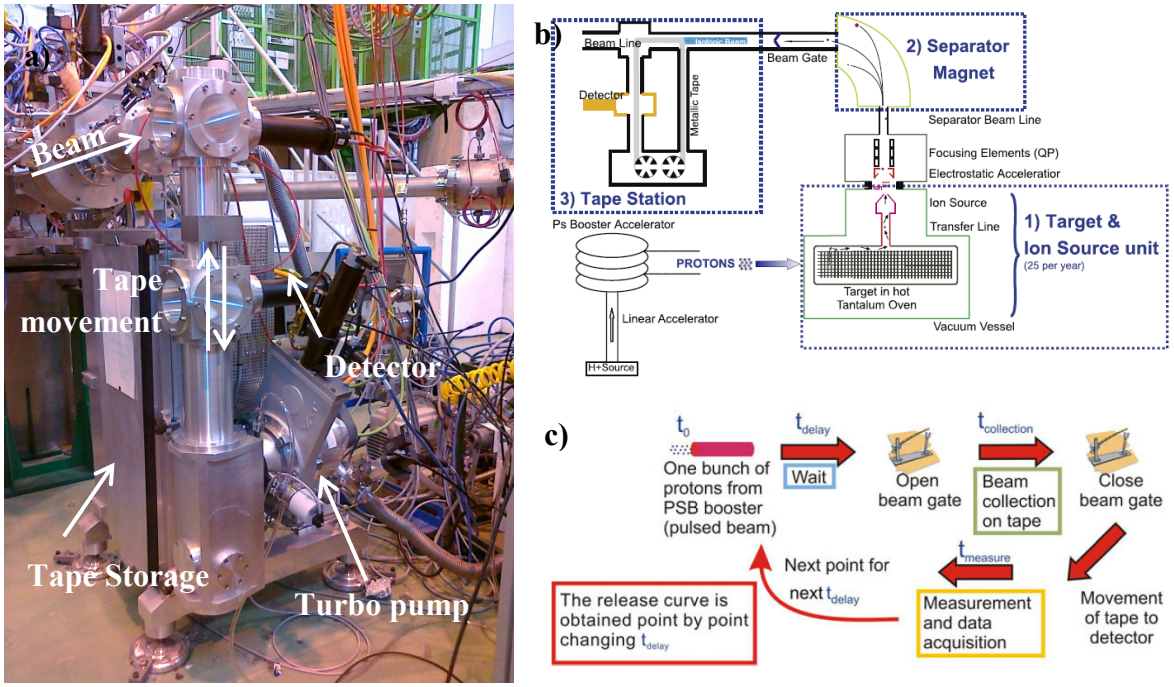

Figure II-1 – Picture of the fast tape station at ISOLDE (a), scheme of the RIB production until it arrives at the tape station [26] (b) and schematic representation of the tape station operation to build the release curve [26] (c).

For isotopes which don't have characteristic gamma decay another type of test can be done using β decay properties. After collection, the tape is transported to the detector and the decay is measured over time, building a decay curve. This permits the identification of an isotope through its characteristic half-life.

There are two tape stations at ISOLDE which ares located at different beam lines after the mass separator. The main difference between them is the minimum possible time that the tape takes to move from the detection zone to the measurement zone. Because of that, one is called the fast tape station ($t_{transport,min}$=200 ms) and the other the old tape station($t_{transport,min}$=900 ms).

To evaluate if there are contaminations in the beam after separation, gamma spectroscopy can be done, in which the different isotopes are assessed by their gamma decays. The peaks obtained are then compared (energy and relative intensity) with references in databases [14,82] to identify the isotopes.

II.2 Raw Material

For the material characterization studies done at the University of Aveiro, the raw material used to produce the calcium oxide (CaO) was a <5μm calcium carbonate ($CaCO_3$) powder, with 99.5% chemical purity (metal basis) that was acquired from *Alfa Aesar*®. Characteristics of the material were retrieved from the supplier and additional characterization was also done, such as SEM, Coulter, XRD and DTA/TGA analysis (whose technique details are described ahead (Section II.1)), which results are presented in Figure II-2 to 3 and resumed in Table II-2.

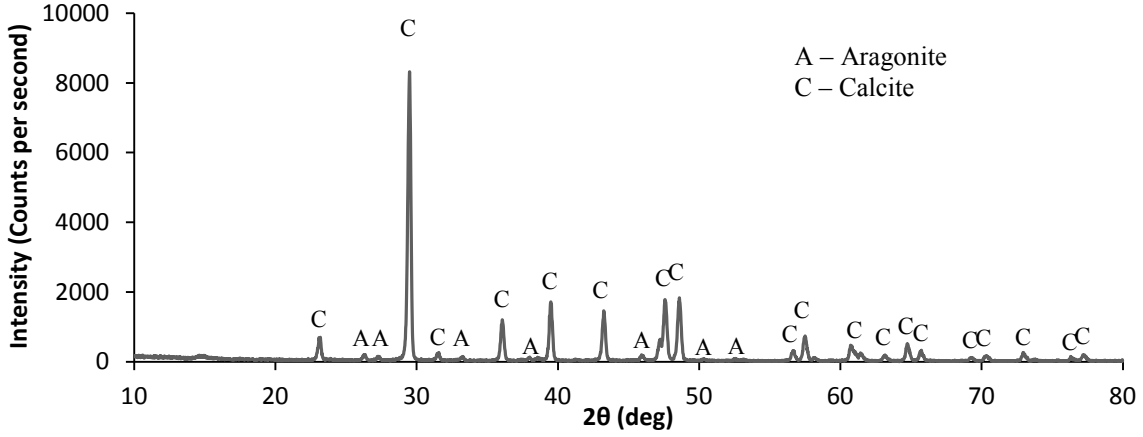

Figure II-2 - XRD of the raw material, $CaCO_3$, used to produce CaO.

As expected, calcite and traces of aragonite, a polymorph of calcite, were detected by XRD on $CaCO_3$ (Figure II-2).

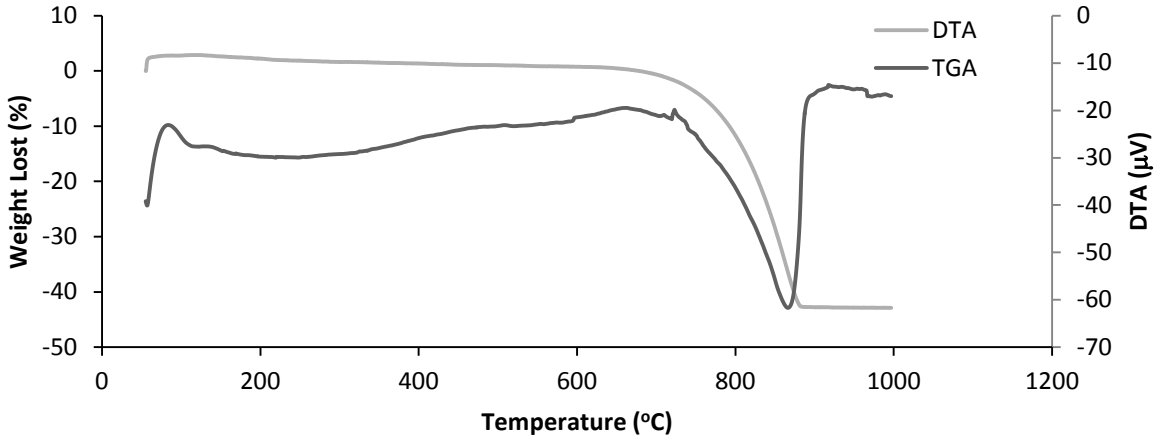

Figure II-3 - Thermal analysis of calcium carbonate in air atmosphere.

The DTA/TGA done on the raw material (Figure II-3) in air also confirms the presence of calcite by the high loss of mass between ~680°C and ~890°C and the coincident endothermic peak in the DTA curve. This analysis showed no signs of aragonite that should be seen in DTA by a peak at around 520°C [52], which confirms that it is present in small quantities.

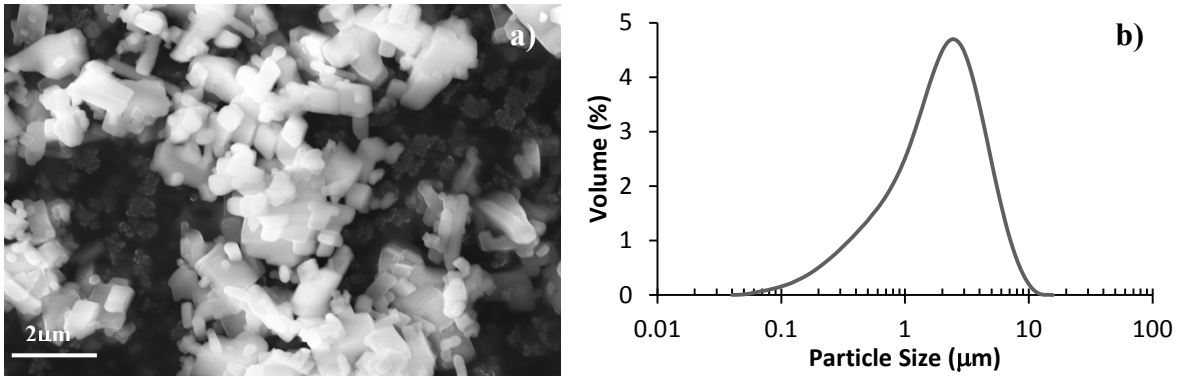

Figure II-4 – SEM observation of the $CaCO_3$ powder (a) and particle size distribution determined by laser diffraction (b).

The morphology of $CaCO_3$ particles was observed in SEM. As can be seen, in the Figure II-4 a), they are cubic shaped, like NaCl, and their sizes are less than 0.5 µm to 3 µm. This is confirmed by the particle size distribution determined by laser diffraction in Figure II-4 b) which average value, $G_{Coulter}$ is given, together with other characteristics, such as density, specific surface area, SSA, and equivalent spherical diameter calculated from the SSA value, $G_{BET,}$ is indicated in Table II-2.

Table II-2 – Characteristics of the raw material ($CaCO_3$).

Present Phases[*]	Calcite, Aragonite	**Impurities:**[*1]	
Density[*1]	2.930 g/cm^3	**Strontium**	0.0058%
SSA	2.80 m^2/g	**Chlorine**	0.0045%
G_{BET}	0.90μm	**Sodium**	0.0025%
$G_{Coulter}$	2.44±1.87μm	**Total sulfur**	0.0011%
		Magnesium	0.0007%
		Iron	0.0005%
		Barium	0.0004%

[*] Determined by Powder X-Ray Diffraction
[*1] *Alfa Aesar*® information

II.3 Calcination

The decarbonation of $CaCO_3$ to obtain CaO was done in a *Termolab*® vertical alumina furnace with a *Eurotherm*® PID (proportional – integral – derivative) controller in the University of Aveiro. A vacuum system was coupled to the furnace, which consisted in a vacuum pump *Adixen*® *Pascal 2010 SD* with a nominal pumping speed of 8.3m^3/h, a pirani gauge *Adixen*® *AP 2004* to measure the pressure (p) and a pressure display *Adixen*® *ACS 2000* connected to a computer to register the pressure during the thermal cycle with the software *AVG View* provided by *Adixen*®. The vertical tube had steel flanges cooled by a circuit of water to avoid the deterioration of the rubber o-rings. In the connection of the pump to the tube there was a valve to control the pumping speed at the beginning of the cycle. A needle valve was installed in the furnace to break the vacuum slowly, when the calcination was finished. The sample holder made of alumina foam and mulite served as support to a cylindrical crucible with a lid for keeping the powder inside during the initial stage of the pumping of the furnace.

Before calcination of the powder, tests of the furnace hot zone, heating and cooling rates, holding temperature and cycle duration were done. To accurately measure the temperature, a type-*R* thermocouple (Platinum/Platinum-13%Rhodium) was placed in the base of the sample holder and connected to a two channel *Zipp & Zonen*® recorder. As the furnace doesn't have forced cooling, at the cooling rates used (10^{o}C/min) it enters a natural cooling rate from 700ºC to room temperature (RT) taking about 7h.

A test to the vacuum conditions was done too to optimize the vacuum system and detect eventual leaks. In the end of the tests, the minimum vacuum pressure achieved by the system after 6h of pumping was in the order of 10^{-1} to 1 Pa at room temperature and 10Pa at 1100ºC.

In the following table (Table II-3) are summarized the calcination conditions. The calcined powders were characterized by XRD, BET and SEM. The sample weight loss (WL) was always taken to evaluate the extent of the decomposition.

Table II-3 - Experimental conditions used to decompose $CaCO_3$ into CaO, in vacuum.

Sample mass	~10g
Calcination Temperature	550 – 1000ºC
Heating Speed	10ºC/min
Cooling Speed	10ºC/min to 700ºC followed by natural cooling
Holding Time	2 to 48h
Pressure	~1 Pa

By plotting the furnace readout pressures during the thermal cycle versus time for different temperatures, useful information about the decomposition reaction can be obtained, as illustrated in Figure II-5 for calcinations at 600, 700, 800°C.

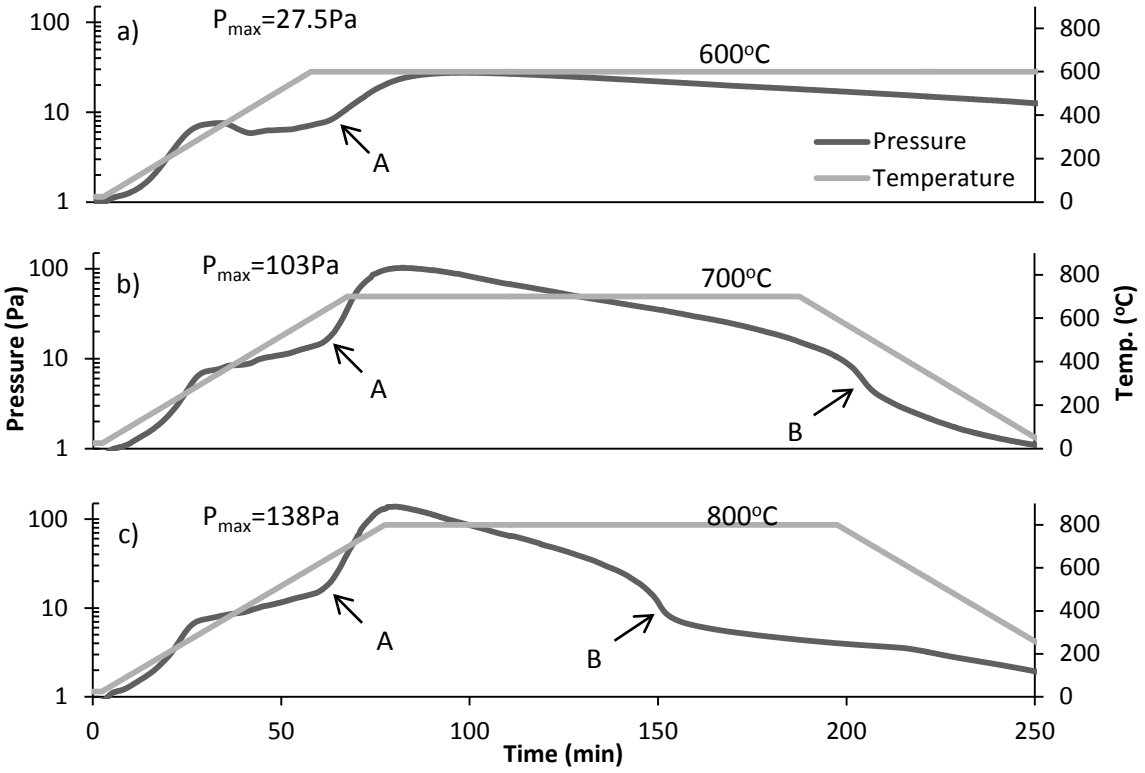

Figure II-5 – Furnace temperature and pressure readouts for the samples calcined at 600°C (a), 700°C (b) and 800°C (c). The beginning of the reaction (A) and end (B) are marked on the figure.

In Figure II-5 the time window, where the reaction happens, can be roughly estimated by the rising pressure zone, indicated as A in the figure, which corresponds to the production of CO_2. The duration of this zone (time between A and B) and its maximum pressure is clearly influenced by the temperature of the holding time, showing that the

reaction is much faster for high temperatures, since the maximum attained pressure is higher and the duration is shorter.

II.4 Calcium Oxide Reactivity Tests

Nanometric calcium oxide powder is reported to be very reactive when exposed to air at usual RT conditions. [61,66] To study the reactivity of the produced calcium oxide, somea samples of the synthetized powder with different SSAs were exposed to air during 2 days and the weight gain was taken along the exposure time. The powder specific surface area, XRD phase identification and crystallite size (before and after exposure) as well as DTA/TGA of the reacted powders, were performed.

To evaluate the reversibility of the air reaction, the exposed powders were thermal treated in vacuum at 800ºC for different times (5, 15 and 40 min) and the SSA and crystallite size were determined. Also DTA/TGA was done to the "recovered" ones to evaluate if the conversion to CaO was complete.

II.4.1 Sample Storage

Due to the observed high reactivity of the produced CaO powders to moisture and CO_2, the samples were kept under special conditions, reducing the pressure of these gases in the surrounding atmosphere. This was achieved by using a 2l *Nahita*® glass desiccator with a valve which could be connected to a pump to evacuate the system, storing the samples under vacuum.

The need to open the desiccator during the studies exposed the samples to air and so, a desiccant, silica gel, was used to reduce the hydration. Afterwards, the nanometric CaO powder itself (produced in house by decomposition of $CaCO_3$ in vacuum at 700ºC), was used as a desiccant. [61] This powder proved to be much more effective, greatly reducing the weight gain of the samples, as can be seen in Table II-4.

Table II-4 - Weight gain of one CaO sample with different desiccants.

Desiccant	Weight gain (%)	
	Silica Gel	**CaO**
1st day	0.24	0.01
2nd day	0.55	0.02

II.5 Microstructural Evolution During Vacuum Sintering

The obtained CaO powder was compacted and thermal treated in a furnace at the University of Aveiro, under a temperature range and vacuum pressure equivalent to those used during CaO target operation at ISOLDE, CERN.

In order to study the microstructural evolution during sintering, cylindrical compacts, 10 mm diameter, 2-3 mm in thickness were pressed by using a hydraulic *Carver® Laboratory Press – Model C*. A small study of the press conditions was done just in order to evaluate the pressure required to give the compact some mechanical integrity for normal handling and having at the same time a high porosity. It was concluded that the best settings were pressing ~0.25 g of powder at 125 MPa for 5 s, resulting in a compact with high porosity, P~60%.

Since the target units are operated at pressures of $\sim 10^{-4}$ Pa, a furnace which could achieve approximate vacuum conditions was used. A *Thermolab® FTV 213/2007* furnace was used, which could reach pressures of 10^{-4} Pa at RT and from 10^{-3} to 10^{-2} Pa 1200ºC. This furnace is composed of a small chamber, with a tungsten heating element, which was pumped by a rotary and an oil diffusion pump. Both chamber and diffusion pump were cooled by a water circuit.

The handling of powder and compacts revealed to be a very challenging process, since hydration and carbonation occurs very fast, affecting the powder characteristics and causing break of compacts. Therefore, immediately after pressing, the compacts were maintained under vacuum. Nevertheless, some samples were found broken after the thermal cycle.

A summary of the sintering conditions can be found in the Table II-5. After sintering, the specific surface area (SSA) the shrinkage (whenever possible) and crystallite size were determined.

Table II-5 - Experimental conditions in CaO sintering experiments.

Sample	CaO compacts (P≈60%)
Sintering Temperatures	900 – 1200ºC
Heating Speed	10ºC/min
Cooling Speed	15ºC/min
Dwell Time	3min – 10h
Pressure	10^{-4} - 10^{-2} Pa

The obtained SSA reductions and shrinkage were then plotted vs. holding time and fitted accordingly to the model presented in equation (I.27), using the program Origin v8.5.1. Identically, the same data treatment procedure was done to the shrinkage.

II.6 Material Testing at ISOLDE-CERN

After the synthesis of CaO from calcium carbonate, the respective powder characterization and sintering kinetic studies at the University of Aveiro, this investigation proceeded at ISOLDE. Before online operation, studies were performed on the CaO synthesis at ISOLDE to evaluate the powder microstructure. This was done using the established conditions for CaO target production, named "old procedure", and to compare the microstructure of the calcinated powder obtained at ISOLDE using an equivalent thermal cycle as used in Aveiro, calling it "new procedure".

In consequence of the investigation done, new conditions for the target preparation and handling could be implemented.

II.6.1 CaO Target Production at ISOLDE: "Old Procedure"

In order to produce and characterize the CaO used in the past at ISOLDE, the "old procedure" was done. The raw material ($CaCO_3$) was first dried by heating it in a porcelain crucible at 200ºC for a day. A rhenium (Re) boat with approximately the dimensions of the target (195 mm long and 20 mm diameter) was filled with the powder and put in a dedicated oven (see Figure II-6), similar to a target unit, in high vacuum ($10^{-3}<p<10^{-2}$ Pa) using a turbo and a rotary pumps. The temperature was then increased (measured with an optical pyrometer), until pressure reached 10^{-2} Pa, up to 1200ºC. The process took about 24h and was over when the pressure reached a value lower than 10^{-3} Pa, indicating that the decarbonation reaction is finished. To make sure that the decarbonation was complete the oven was kept at the final temperature for some hours, after reaching 10^{-3} Pa. Afterwards, the oven was cooled down and purged with Ar and the Re boat was refilled - due to the high loss of mass (~44%) - with $CaCO_3$, maintaining the CaO produced so far. The whole process was then repeated one more time.

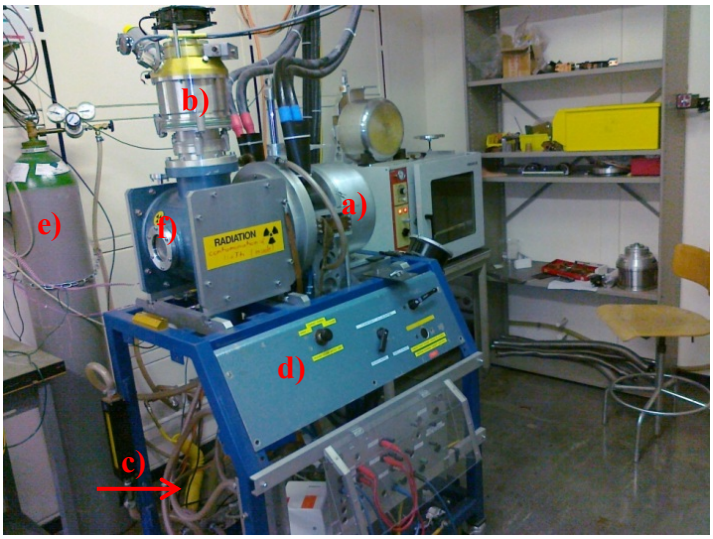

Figure II-6 – Pumpstand used to produce the CaO at ISOLDE. In the picture: the oven (a), the turbo pump (b), and below a rotary pump (c), the controls for the water cooling and others (d), the bottle of Ar to purge the system (e) and the window used to measure the temperature with the pyrometer (f).

At the end of the process (which takes around 48h) the oven was purged again with Ar and the Re boat was taken out of the oven and kept in a desiccator for material characterization testing. During the whole process the Re boat was weighted whenever possible to assess the reaction completion. Since the oven is known to have a thermal gradient from the sides to the center of it, samples were taken separately in both temperature zones for characterization by SEM, XRD and BET.

These synthesis conditions were applied to another carbonate powder (see its characteristics in Appendix (Table A-1)) previously used at ISOLDE in the preparation of the CaO targets. This sample was designated T12 and was characterized through BET, XRD and SEM. The calcination conditions are summarized in Table II-6.

Table II-6 - Calcination conditions for the "old process" of the CaO target production at ISOLDE.

Calcination Temperature	up to 1200°C
Heating and Cooling Speed	Not defined
Holding Time	Not defined (whole cycle takes ~48h)
Pressure	10^{-3} to 10^{-2} Pa

II.6.2 CaO Target Production at ISOLDE: "New Procedure"

Based on the obtained results for CaO synthesis, handling and sintering in this research, adjustments for the production method were proposed and applied. Further changes in the target unit were also done.

To produce the new target, the raw material used at the UA studies was used. The process was very similar to the old one, but the following changes were made: (i) the heating and cooling rates were fixed at 10°C/min; (ii) the temperature was risen in one step to 800°C (overriding the pressure interlock at 10^{-2} Pa) and the pressures rose up to a maximum of 160 Pa, similarly to the synthesis studies at the University of Aveiro (see Figure II-5); (iii) instead of a pyrometer to measure the temperature, a thermocouple type K was installed for a more accurate control; (iv) the material was kept at 800°C, for 48h, in order to insure a complete reaction and to outgas the impurities; (v) no refill was done to avoid unnecessary material hydration (vi) and the transfer of the material to the target unit was done in a gloves box in a controlled Argon atmosphere (as seen in Figure II-7). Afterwards, as usual for every target at ISOLDE, the target and the ion source temperatures were calibrated against input voltage and current, and the target was mounted on the offline separator for further tests and outgasing of impurities. The newly produced CaO was likewise characterized by BET and XRD. Two powder samples, named S80, were taken, one from the center and another from the side of the target. The calcination conditions can be seen in Table II-7.

Table II-7 - Calcination conditions for the "new process" of the CaO target production at ISOLDE.

Calcination Temperature	800°C
Heating and Cooling Speed	10°C/min
Holding Time	~48h
Pressure	10^{-3} to 160 Pa

The new target unit has also undergone some evolution: two type C thermocouples were installed in order to measure the current temperature at the center of the container and at the sides, during online operation. A different heat shielding was installed in order to reduce the temperature gradient along the container. A different ion source with improved ionization efficiency of argon was used.

To assess the reproducibility of the process at ISOLDE and characterize the new target material, a calcium oxide sample was produced in the same target oven with the same thermal cycle used at the UA (2h of holding time at 800°C, with 10°C/min of heating and cooling rates). The resulting sample was named T80 and characterized in terms of surface area and porosity.

Figure II-7 – Gloves box used to do the material change to the target unit. In the picture: the pre-chamber (a), the gloves box main chamber (b), a bottle of Ar to fill both pre-chamber and main chamber (c) and a rotary pump (d).

II.7 Beam Tests at ISOLDE-CERN

II.7.1 Offline Measurements

The target unit was tested at the offline mass separator to evaluate if there were no leaks and if the electrical, gas and water connections were working, as is usual procedure at ISOLDE. The target unit was then heated up to operation temperatures (up to 800^{o}C), which in the case of the old CaO targets was around 1100^{o}C to 1200^{o}C. Stable beams were assessed for different masses to evaluate the level of impurities produced by the target material and ion source. The ion source efficiency was then tested by injecting known quantities of noble gases through a calibrated leak, and monitoring the mass separated in the beam. The target was left for 3 days at the operation temperatures to outgas impurities. Before the transport to the ISOLDE frontend, the target unit was filled with argon and sealed.

II.7.2 Online Operation

The new target was mounted in the front end of ISOLDE, pumped and operated at temperatures up to 800^{o}C with low proton intensities, 8x10^{12} protons per pulse (usually its 3x10^{13}). The new target was labeled with the reference CaO#469.

Since there was a thermal gradient on the container of the target CaO#469, a weighted average, to determine a representative (rounded) temperature given by the thermocouples (T), was taken into account according to the following formula:

$$T = \frac{2T_S + T_C}{3} \quad \text{(II.5)}$$

where T_S is the temperature at the sides of the container, T_C is temperature at center of the container, as schematically represented in Figure II-8. The calculated temperatures varies from 520°C (see Table II-8), with temperature differences from the center to side of 190°C to 840°C where this difference was only 40°C.

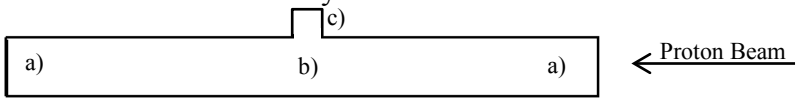

Figure II-8 - Schematic representation of a target container indicating the sides (a) and the center (d) of it, where the transfer line is also represented (c).

Release curves were done using the tape station (described in the following section) and gamma spectroscopy (also described ahead) in order to assess radioactive isobaric impurities in the beam. For the tests on the very short lived isotopes such as ^{31,32}Ar the tape station is not able to measure. For this a special experimental setup (IS476 [2]) was used. In order to compare and scale the values ^{33}Ar was measured in both systems. The tests done are summarized on the Table II-8.

Table II-8 - Summary of the online measurements and tests done on target CaO#469.

Isotope (half-life)	Temperature (°C)		Objective	Method
	Target	Ion Source		
^{35}Ar (1.78s)	650	1980	Study the yield drop by several measurements over the run. Release curve measured	Tape Station
	840	2070	Assess the maximum yield	Tape Station
	730	1980	Study effusion and diffusion processes and the respective temperature influence	Tape Station
	650			
	520			
^{31}Ar (15.1ms)	650	1980	Assess the yield	IS476 [2] (Tape Station)
^{32}Ar (98ms)	650	1980	Assess the yield	
^{33}Ar (174.1ms)	650	1980	Assess the yield	
^{19}Ne (17.22s)	730	1980	Study effusion and diffusion processes and the respective temperature influence	Tape Station
	650			
	520			
^{10}C (19.3s)	730	1980	Assess the yield	Tape Station
^{15}C (2.45s)	730	1980	Assess the yield	Tape Station
^{6}He (806.7ms)	650	1980	Assess the yield	Tape Station

In order to compare the new target with older ones, information about the operation performance of other targets was taken. This information regards mainly, the obtained yields (and how they dropped) and the operation parameters. The target labeled as

CaO#123 was operated in November 1999 and was the best calcium oxide target to be operated at ISOLDE, since its yields on several isotopes were the highest registered [45]. This target was operated at 1050^{o}C. Two recent targets were also compared: the targets CaO#408 operated in August 2009 and CaO#419 in November of the same year. The latter is representative of a standard CaO target. All of the old targets were run at $3x10^{13}$ protons per pulse.

Chapter III - Results and Discussion

III.1 Material Characterization Study

As referred before, in order to improve the intensities of beams at ISOLDE, the target material has to be improved mainly in terms of the diffusion properties. To attain this goal, the microstructure of the target material had to be investigated aiming at controlling it. This section presents the results of the CaO synthesis from the respective carbonate, powder characterization, and powder microstructure evolution during thermal treatments.

III.1.1 Synthesis of CaO

In order to study the influence of the thermal cycle in the decomposition reaction of $CaCO_3$, different conditions were tested. The summary of the decomposition conditions and characteristics of the obtained CaO powder can be seen on Table III-1. A holding time of 2h was used for the majority of experiments, which was increased for lower temperatures in order to achieve total decomposition. A long duration cycle of 48h, at 1000°C, was also tested in D10 sample. The main parameters to characterize the obtained powder were the crystallite size, by XRD using the most intense peak (200), and the specific surface area. From the surface area, applying equation (II.3), the particle size could be estimated.

Table III-1 – Summary of the decomposition conditions and characteristics of the obtained powders.

Sample	T (°C)	t (h)	WL (%)	p (Pa)	SSA (m^2/g)	G_{BET} (nm)	XS (nm)	Main XRD Phases Detected	Average Pore Size (nm)	P (%)
D55	550	16	36	~1	19	-	35	CaO, $CaCO_3$	-	-
D60	600	12	44	~1	53	34	37	CaO	-	-
D65	650	3	44	~1	38	-	38	CaO, $Ca(OH)_2$	-	-
D70	700	2	45	~1	49	37	35	CaO	-	-
D80	800	2	46	~1	46	39	38	CaO	-	-
D90	900	2	46	~1	42	42	36	CaO	-	-
D10	1000	48	45	~1	35	51	50	CaO	11	32
N80	800	2	-	$\sim10^{-1}$	58±4	31±3	32±2	CaO	12	44

For a total $CaCO_3$ decomposition, 44% of weight loss (WL) is expected taking the stoichiometry expressed by equation (I.22), but in some cases, higher values of WL were observed due to losses of powder from the crucible during the furnace operation. The sample D55, calcined at 550°C, had a lower value of WL (36%) suggesting incomplete

decomposition (confirmed by XRD) which matches the low value of SSA, due to the presence of low SSA $CaCO_3$ (2.80 m^2/g). In the case of D65, the decomposition was complete but significant hydration had occurred, as confirmed by the detection of $Ca(OH)_2$ by XRD, leading to a lower SSA value. The effects of powder hydration on the SSA will be further detailed ahead. In all other samples no $CaCO_3$ phase or traces could be detected on the XRD, confirming the full decomposition, but often traces of the $Ca(OH)_2$ could be detected. These results are similar to those obtained by D. Glasson at the same temperature, as can be seen in Table I-3, page 32.

After the optimization of the furnace operation, to operate under lower vacuum (p~10^{-1}Pa), the samples produced at 800°C (N80) yielded an average SSA value of 58±4 m^2/g with XS being 32±2 nm in agreement with G_{BET} (31±3 nm).

In order to better visualize the effect of the decomposition temperature on the surface area and crystallite size, for similar vacuum conditions, the plot of the Figure III-1 was done.

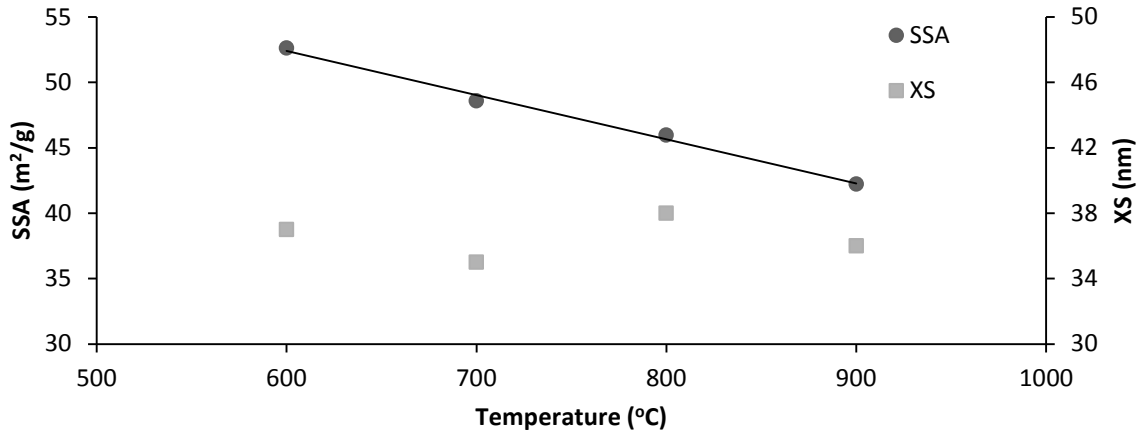

Figure III-1 - Plot of the specific surface area (SSA) and the crystallite size (XS) versus temperature for the calcined powder, obtained under similar vacuum conditions, and 2h of holding time.

In Figure III-1 a linear decrease of the SSA with the increase of the decomposition temperature can be seen. The behavior is in agreement with the results of E. Powell [61]. D. Glasson's [56] results showed increasing surface area until 800°C and then fast decreasing of SSA, claimed to be due to sintering of CaO, he stated. This behavior doesn't match the obtained results in this work. No tendency was found for the variation of the determined crystallite size. The XS values present a fairly good agreement with the obtained G_{BET}, value and confirm that a nanometric material is obtained by decomposing $CaCO_3$ under vacuum, in this range of temperatures, as confirmed by other authors [50,51,54,55,57].

Despite the fact that the obtained powders were nanometric, the obtained surface areas are somehow lower than those obtained in the literature (see Table I-3, in page 32). This differences may come from the better vacuum conditions reported in the literature ($10^{-2}<p<10^{-5}$ Pa), lower temperatures used for decomposition and better storage/transport conditions up to the material analysis equipment. Furthermore, J. Ewing [63] and D. Beruto [58] reported that in powder beds, residual pressures of CO_2 decreases the surface areas obtained, by enhancing sintering. Maximum pressures over 100 Pa were measured during the decompositions, as can be seen in Figure II-5 in page 50, which according to J. Ewing [63], can lower the SSA. This reduction of surface area is due to the catalytic effect of CO_2 on the sintering of the samples. [63] The improvement of the vacuum conditions in this work (with the change of the powder support from porous to denser parts and other adjustment in valves and o-rings), led to the attaining of SSA and XS closer to those in the literature values, as can be exemplified by sample N80 when compared with D80 (higher pressure, see Table III-1).

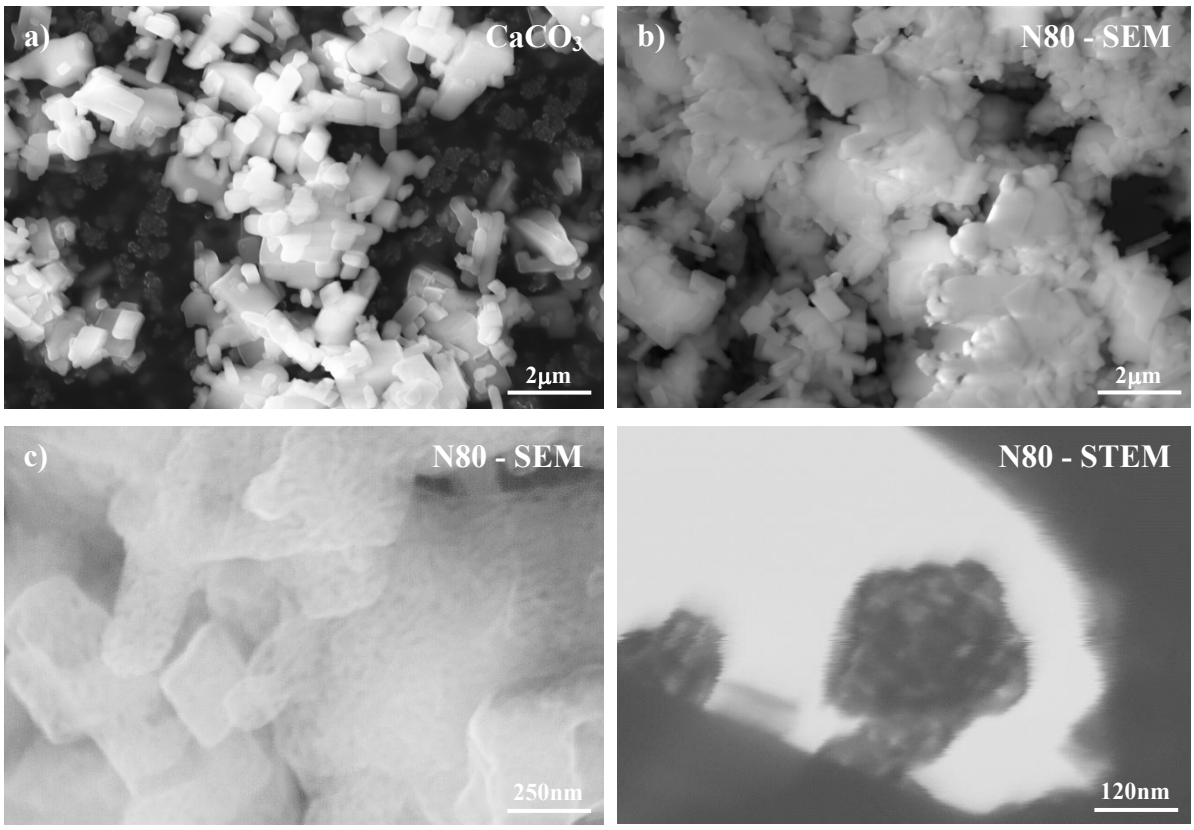

Figure III-2 – SEM Microstructure of the $CaCO_3$ powder (a), the N80 sample (b), a high resolution SEM at the N80 sample (c) and STEM done to N80 sample (d).

The sample D10 (as shown in Table III-1) was synthesized at 1000°C for a longer time (48h), to approximate the calcination conditions previously used at ISOLDE. [9] As

expected, lower values of SSA and higher values of XS were obtained, but the material was still able to keep its nanometric size.

SEM and STEM was used to analyse the microstructure of the N80 powder, as presented in Figure III-2. Observing the microstructures of the raw material in the Figure III-2 a) and the N80 sample in Figure III-2 b), the decomposition reaction can be classified as pseudomorphous due to the small changes in the particle size and shape. This was also observed by D. Beruto [54] and others [55,49,63]. The CaO powder presents a higher degree of agglomeration and rounded edges that may come either from hydration during handling or/and transport to the microscope [68].

The CaO nanograins were hard to see in SEM. The apparent orange-peel roughness observed at the surface of the particles in the SEM microstructure of Figure III-2 c), and in the STEM observation of a thin agglomerate in Figure III-2 d), was reported to correspond to the image of nanosized CaO grains [55]. The SEM and STEM observations permit to conclude that the CaO powder is constituted by agglomerates of identical shape and size as the initial $CaCO_3$ particles and that these agglomerates are constituted by nanograins smaller than 70 nm. The particles seem to be more like plate shaped, agreeing with what was observed for CaO powder obtained by $CaCO_3$ in other studies [50,64].The porosity inside the agglomerates couldn't be resolved by SEM.

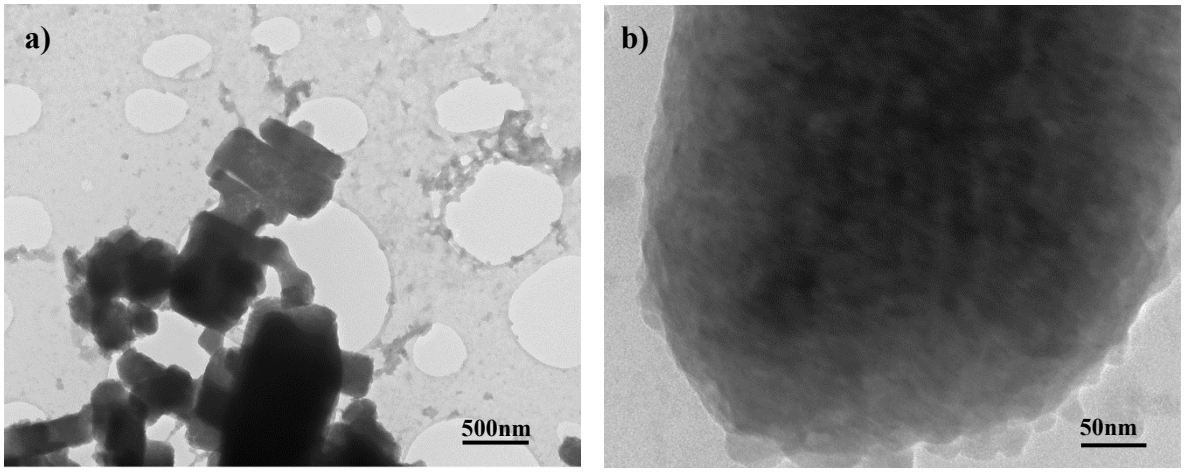

Figure III-3 – TEM observations of CaO sample, N80.

By taking a look in the TEM micrographs presented in Figure III-3, the cubic shaped CaO agglomerates can be observed in the left and on the right a high magnification image shows that they are constituted by very fine grains, confirming the previous observation in SEM/STEM. One of the limitations in the TEM analysis came from the

significant hydration of the sample due to the drying of the alcohol suspension drop before the microscope observation.

Taking the adsorption of N_2 gas at 77K on the powder samples N80 (800°C) and D10 (1000°C, 48h), the whole isotherm was determined for each powder in Figure III-4.

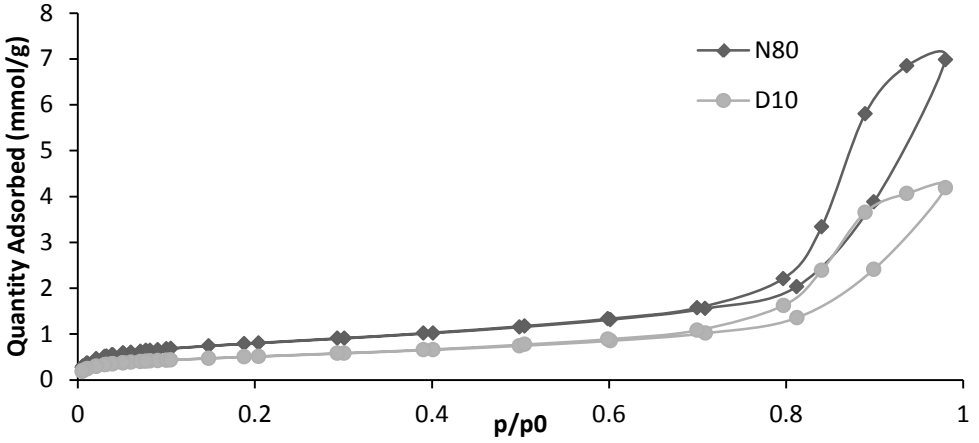

Figure III-4 - Isotherms obtained by adsorption of N_2 for the samples D80 and D10.

Both isotherms are of type IV and present hysteresis [81]. These types of isotherms are associated with materials that have mesoporosity. [81] The software of the BET equipment was used to calculate of the pore size distribution using the Barret-Joyner-Halenda (BJH), giving also the pore volume. In Figure III-5, the determined pore size distribution for the N80 and D10 samples is represented.

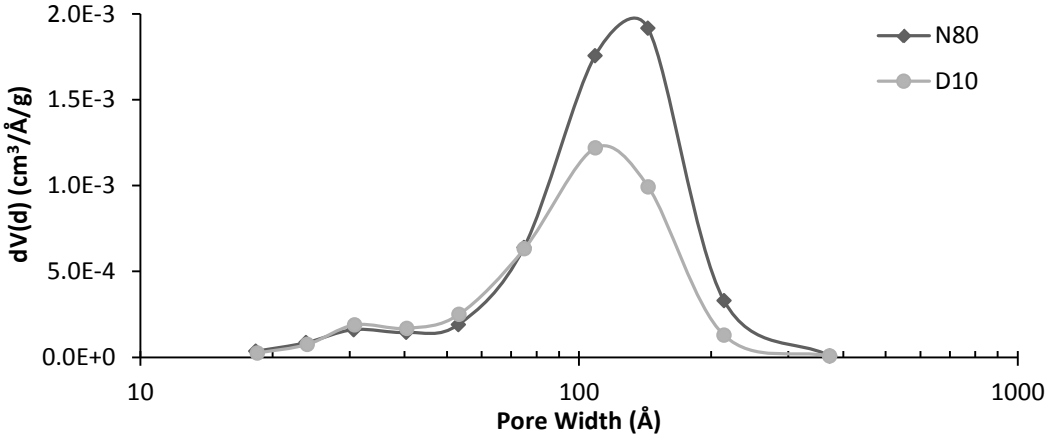

Figure III-5 - Pore size distribution of the samples N80 and D10.

From Figure III-5 it can be seen that both pore size distributions are unimodal and that the porosity of the sample D10 is lower and slightly shifted to lower pore sizes, comparing to the N80 sample. In Table III-1, the values of porosity and average pore size calculated from the curves of Figure III-5 are presented. The lower average pore size and

lower porosity at the sample D10 calcined at 1100°C, 48h, when compared with the N80 sample calcined at 800°C, 2h, are in accord with the reduced SSA value in that sample and show that at 1000°C sintering effects are already relevant.

The values obtained for the porosity of N80 sample were consistent with the ones published in the literature [54] (41.5% of porosity and 10 nm of pore average size in CaO obtained from $CaCO_3$ vacuum calcination). Assuming that the reaction is pseudomorphous and taking the molar volumes of CaO and $CaCO_3$ one could expect a porosity of ~55%. This is probably related to some sintering either of $CaCO_3$ before the decomposition [56] or of the CaO during the calcination, possibly catalyzed by the presence of the CO_2 resultant from the decomposition [55].

III.1.2 Reactivity in Air

As stated in section I.4.3, the calcium oxide reacts, spontaneously, with H_2O and CO_2 in air. The high surface area of the CaO powders in this study will enhance the reactivity, as reported by D. Beruto [66] and E. Powel [61], affecting powder characteristics. Therefore, the kinetics of the reaction between the nanometric CaO powder and air and the effect on the powder characteristics needs to be investigated, prior to the powder processing.

In order to know the extent of the hydration/carbonation reactions, DTA/TGA tests under Ar flow, were done in N80 sample, as shown in the Figure III-6 a) after normal handling* and b) intentionally left at air for 2 days.

As can be seen in the TGA curve presented in Figure III-6 a), the sample, after normal handling, keeps reacting until 330°C (rise in weight of 1.2%). This is probably due to residual water/carbon dioxide coming from its surface (adsorbed), from the gas bottle (residuals) or even air leaks in the system. Around 400°C the decomposition of $Ca(OH)_2$ is happening (DTA endothermic peak and TGA loss of mass). The $\%H_2O$ is about 4.5 wt.% which corresponds (equation (I.24)) to a conversion of ~18 wt.% of CaO in $Ca(OH)_2$ during air exposure. Similarly, from the slight weight loss (~2%) around 600°C, which is most likely due to loss of CO_2 ($\%CO_2$) due to the $CaCO_3$ decomposition, one can estimate ~4 wt.% (from the reaction (I.25)) of carbonate in CaO. In the XRD of the powder after

* A "normal handled" CaO powder corresponds to an exposure at air variable between 5 and 10min, due to the purge and opening of the calcination furnace, weighting and transport to the desiccator.

normal handling (Figure III-7 a)) no $CaCO_3$ and only small traces of $Ca(OH)_2$ were detected. D. Glasson [83] reported that values up to 20 wt.% of $Ca(OH)_2$ in reacted CaO couldn't be detected in XRD. He attributes this to a fast reaction which has a time lag in recrystallization, giving a poorly crystalline phase.

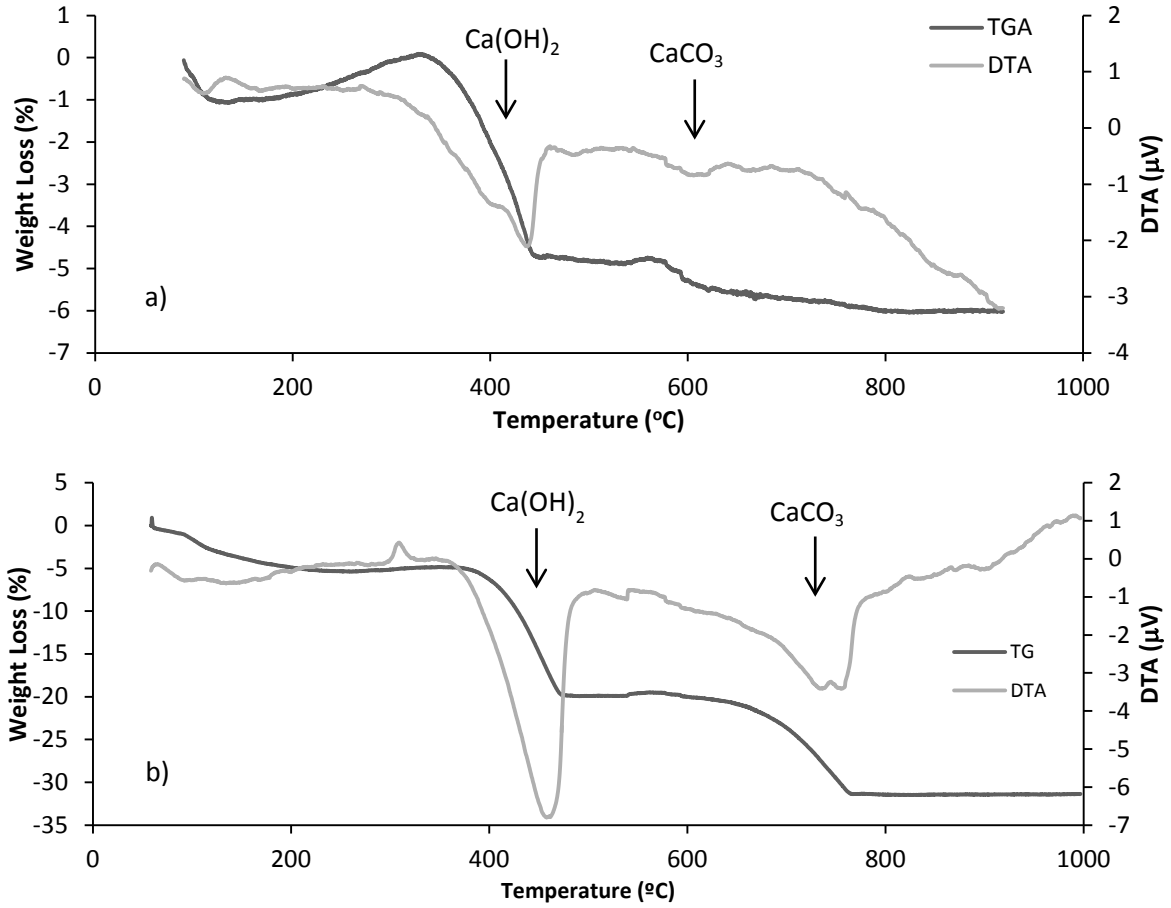

Figure III-6 - Thermal analysis of the N80 sample after decomposition and normal handling (a) and after intentional exposure at air for 2 days (b).

From the DTA/TGA of the Figure III-6 b) the total weight loss (~32%), is equivalent to the weight gain after air reaction for 2 days (~49 wt.%) by changing the base of calculation from reacted CaO mass to non-reacted one. From the DTA/TGA curves, the CaO hydration and carbonation extent are calculated to be ~70 wt.% and ~30 wt.%, respectively (correcting already for weight loss due to adsorbed molecules from 60 to 250^{o}C, as seen in the TGA curve of Figure III-6 b)). These results are consistent with the XRD results (see Figure III-7 b)), where no peaks of CaO were detected, confirming the depletion of CaO, and the intense peaks of $Ca(OH)_2$, whereas only small $CaCO_3$ peaks are detected.

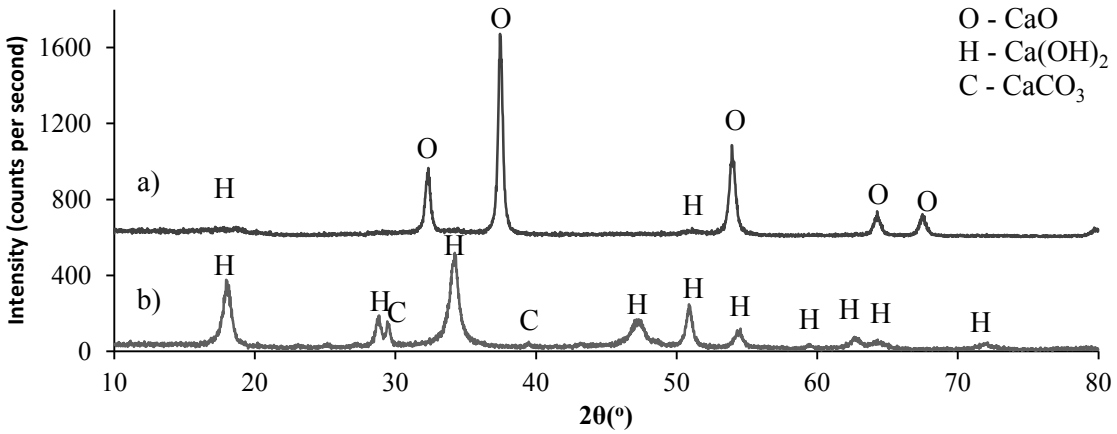

Figure III-7 - XRD of the N80 powder after normal handling (a) and left at air for 2 days (b).

To study the rate and extent of the CaO reaction in air, three samples of different initial SSA (25, 47 and 59 m^2/g) were left at air during Summer time and periodically weighted. The results are presented the Figure III-8 a).

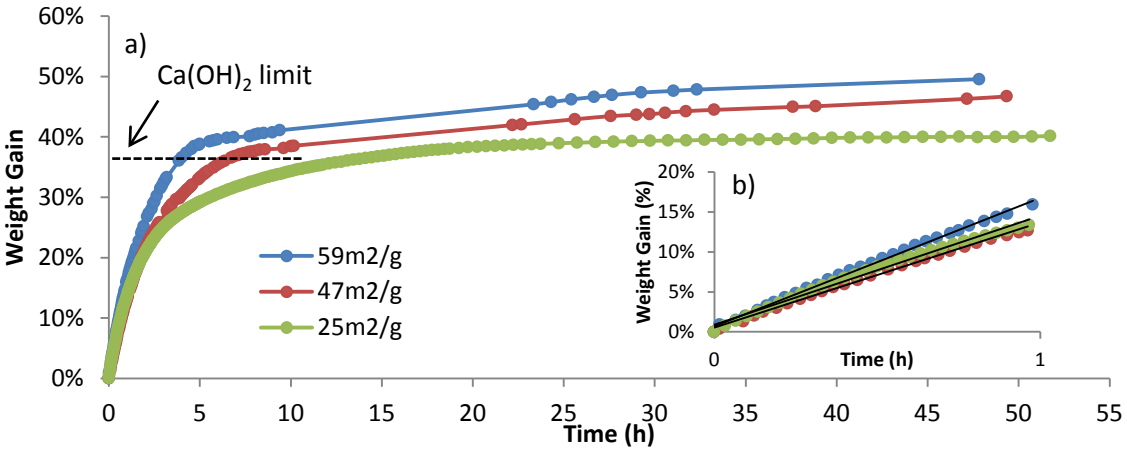

Figure III-8 - Plot of the weight gain over two days for three samples of CaO with different initial surface areas (a) and respective amplification for shorter times (b). The dotted line represents the weight gain if the powder would be completely hydrated.

It can be seen that the kinetics of the reactivity of the CaO in air is divided in two regimes: the initial one with a higher reaction rate, until ~5h, and another slower for longer times. As expected the powders with higher SSA were the most reactive ones, gaining weight faster and attaining larger values of weight gain which are probably related with the interference of the adsorption phenomena. After 2 days, the weight gain was unnoticeable for all the samples, indicating that the reaction was finished. In order to confirm this DTA/TGA would have done, to check for CaO for the samples (47 and 25 m^2/g). The fast hydration when exposed to air, of high surface area CaO powders was previously reported by other authors [54,61] but nothing was referred about carbonation in their studies. Since in

the reacted samples, only a small quantity of $CaCO_3$ was detected (see Table III-2 below) comparing to the $Ca(OH)_2$, the faster regime is assumed to be mainly controlled by the hydration reaction, defined by the equation (I.24).

For shorter times the reaction is nearly linear with time (see Figure III-8 b)). The rate of weight gain is, in average, ~0.3 wt.% min^{-1}. If one, considers this weight gain for shorter times to be essentially due to hydration, the average "hydration rate" can be roughly defined as 1 wt.% min^{-1} of conversion of CaO into $Ca(OH)_2$.

From the above results and using some speculation, the reaction of CaO with air can be described by the following steps: (i) as soon as CaO is in contact with air, it reacts both with H_2O (equation (I.24)) and CO_2 (equation (I.25)) to form spontaneously at the same time respectively, $Ca(OH)_2$ and $CaCO_3$. It also starts to adsorb, gaining additional weight. As shown before, the hydration reaction dominates the faster regime; (ii) as soon as $Ca(OH)_2$ is formed, another spontaneous (accordingly to thermodynamics) reaction can start to form $CaCO_3$ from the hydrate (equation (I.26)); (iii) when most of the CaO is consumed by the hydration reaction, the slower regime starts: the reaction of carbonation is known to form a low porous product slowing down and preventing further reaction [71]. As the reaction progresses more and more, and $CaCO_3$ is being formed, it creates an impermeable layer, slowing down the process and eventually stopping the transformation of $Ca(OH)_2$ into $CaCO_3$.

Since it was observed that during the hydration of CaO there is also carbonation the chosen temperature to test reversibility and to accomplish complete conversion back to CaO needs to be high enough to decompose the formed $CaCO_3$. The selected temperature was 800°C and different times at this temperature were tested. Results for powder characteristics before and after the hydration and reversibility thermal tests can be seen in the Table III-2.

Table III-2 – Powder characteristics before and after air exposure and reversibility thermal tests.

Conditions	BET		XS (nm)	Main Phase	$Ca(OH)_2$ detected		$CaCO_3$ detected	
	SSA (m^2/g)	G_{BET} (nm)			DTA/TGA	XRD	DTA/TGA	XRD
Initial Powder	59	31	33	CaO	~18%	Yes	~2%	No
Left at Air (2d)	9	-	-	$Ca(OH)_2$	~70%	Yes	~30%	Yes
800ºC, 5mn	34	52	29	CaO	~12%	Traces	<2%	No
800ºC, 15mn	28	64	32	CaO	~16%	Traces	<4.5%	No
800ºC, 40mn	22	82	33	CaO	~12%	Traces	<2%	No

From the presented results it can be seen that the initial material is not totally recovered in terms of surface area, although the crystallite size is almost the same as that of the initial powder. The SSA decreases significantly during the powder exposure and increases after the thermal treatment, although, the attained values are less than half of the initial SSA. The time increase at 800°C brings a fast reduction of the SSA values. Not enough studies were made in this work to assess the sintering kinetics of the CaO obtained from $Ca(OH)_2$ but the literature reports higher sintering rates than the one produced from $CaCO_3$ [74].

To evaluate the difference in the microstructure of the material, SEM analysis was done before the powder was left at air and after the thermal treatment. The differences seen in the micrographs were not conclusive enough, but in the literature the hydration reaction is reported to be followed by a volume expansion [70], which would change the morphology of the microstructure.

III.1.3 Sintering Kinetics of CaO

In order to study the thermal behavior of the CaO powders, pressed compacts with a relative density, ρ_0=0.4, were used. Several thermal treatments (TT) were done in a high vacuum furnace using atmosphere and temperature conditions close to those used during target operation. The samples were handled* in order to minimize contact with air, to enhance the reproducibility of the results. Even though all the precautions were taken an error of ~20% is expected from the obtained results, due to some air exposure.

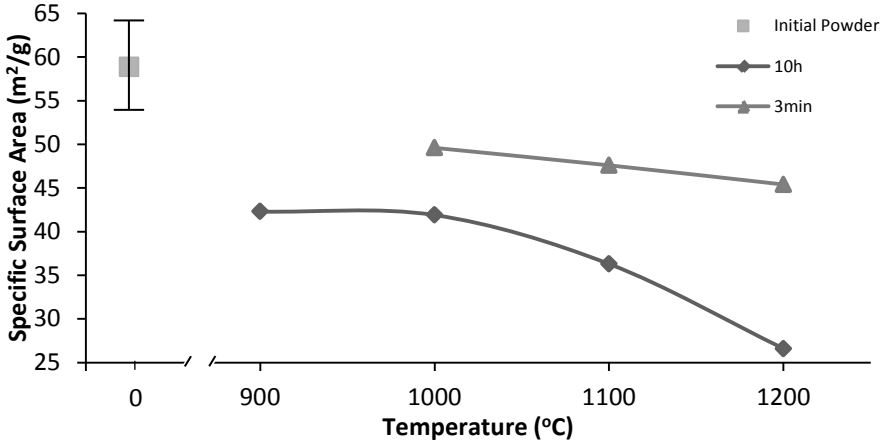

Figure III-9 - Plot of the specific surface area versus the temperature for 3 min and 10h of thermal treatment. The isolated point corresponds to the initial powder.

* During pressing the powder was exposed approximately 5min to air.

In the plot of the Figure III-9, the results of surface area reduction after sintering the powder compacts for the shortest - 3min - and longest times - 10h - can be seen. From this plot it can be observed that for T>1000°C there are net sintering effects which brings a significant surface area reduction from the initial powder (more than one half, in the case of 10h at 1200°C).

It was possible to apply the German and Munir model [73] to the values of SSA at 1200°C by fitting equation (I.27), through iterations, finding S_0 and γ as represented in Figure III-10.

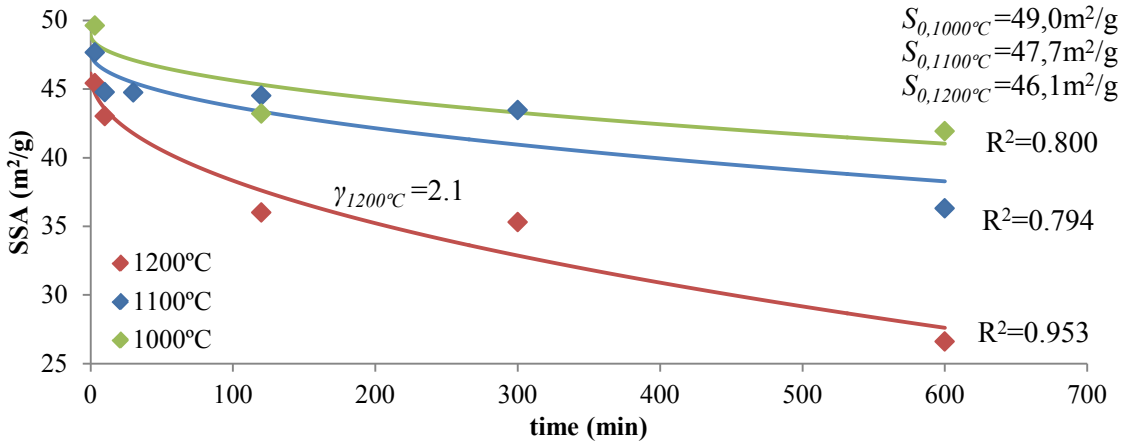

Figure III-10 - Plot of the surface areas versus temperature for several temperature and respective fits.

The obtained value for the kinetic exponent, γ, was 2.1. By checking Table I-4 it can be seen that for Nc=4, ρ_0=0.32, close to the fractional density, ρ_0=0.4, of the green compacts, the determined γ value lies between 1.6 for the mechanism of evaporation-condensation and 2.7 corresponding to volume diffusion.

Since at 1200°C the SSA values were the ones that were obtained with less scattering, the exponent γ=2.1, determined at that temperature, was assumed for the variation of SSA at lower temperatures. The calculated curves could reasonably fit the points, as seen in Figure III-10 (values of R^2 from the fit are presented). This means that the same mechanism may control the matter transport for sintering. From the same plot, it can be seen that the higher degree of sintering happens at 1200°C, and at 1000°C and 1100°C the sintering rate is much lower, as expected from a thermal activated mechanism as diffusion is.

To help the identification of the controlling mechanism of matter transport, the linear shrinkage ($\Delta l/l_0$) at 1200°C was determined for the pressed samples. The diameter values are plotted versus time at 1200°C, Figure III-11, accordingly to equation (I.29).

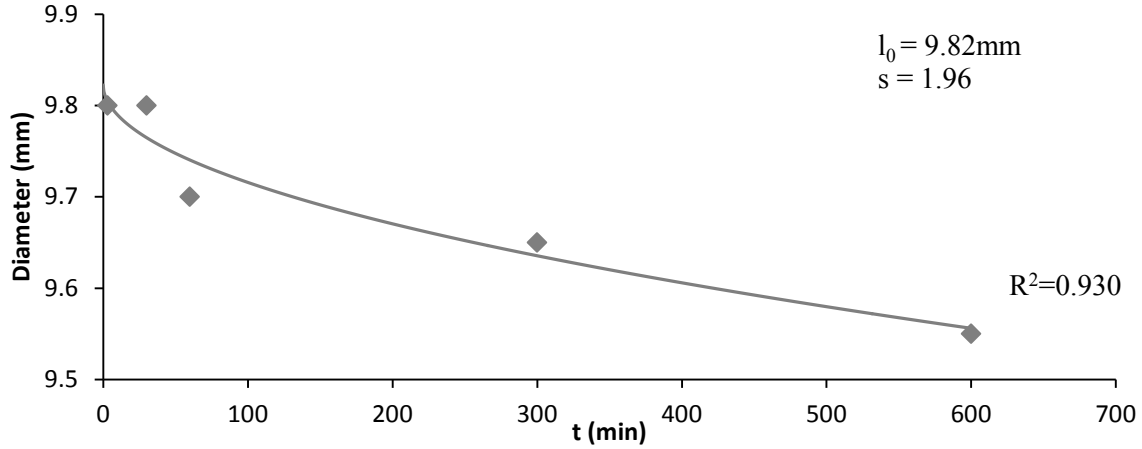

Figure III-11 - Plot of the diameter variation with time at 1200°C.

Since this model also applies for isothermal conditions, l_0 was also taken from the fit. Figure III-11 shows that the reduction of SSA is accompanied by shrinkage of the compact (a maximum value of $\Delta l/l_0$=2.7% was obtained at 600 min). This observation leads to the conclusion that the sintering mechanism can be identified with volume diffusion, since evaporation-condensation doesn't bring densification of the compact. Furthermore, the determined value for the kinetic exponent is s=1.96, and by comparing this result to the theoretical ones in the Table I-4, one can further confirm that the sintering mechanism is identified with volume diffusion (s=2). This conclusion is consistent with the studies of R. Borgwardt [74] in which for sintering in N_2 atmosphere the value of γ obtained was 2.7, identifying volume diffusion as the main sintering mechanism.

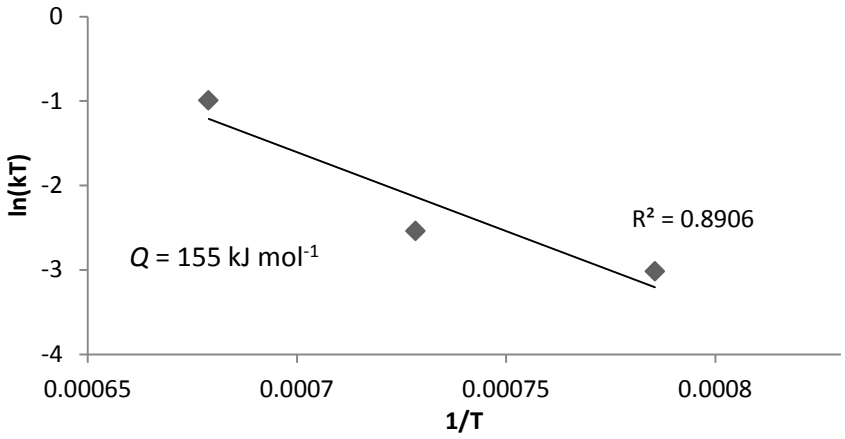

Figure III-12 – Arrhenius plot accordingly to the equation (I.28), from the German and Munir model [73].

The values of the parameter k, equation (I.27), were obtained from the fits of the SSA curves in, Figure III-10, for 1000, 1100 and 1200°C. From the Arrhenius plot of kT values, according to equation (I.28), in Figure III-12, one can estimate the apparent

activation energy for the mass transport during CaO sintering. The calculated values of Q=155 kJ mol^{-1} can be compared with the literature values for auto diffusion in CaO. From the literature, values of *Q*=339 kJ mol^{-1} for the diffusion of ^{45}Ca in CaO polycrystalline samples within the temperature ranges of 1000 to 1600ºC, [84] and Q=142 kJ mol^{-1} for the diffusion of ^{45}Ca in CaO single crystals from 1000 to 1400ºC [85] can be found. The calculated value for the apparent activation energy in the sintering of CaO, in this work, seems consistent with the published results for Ca diffusion in CaO single crystals and may be indicative of sintering controlled by the cation volume diffusion.

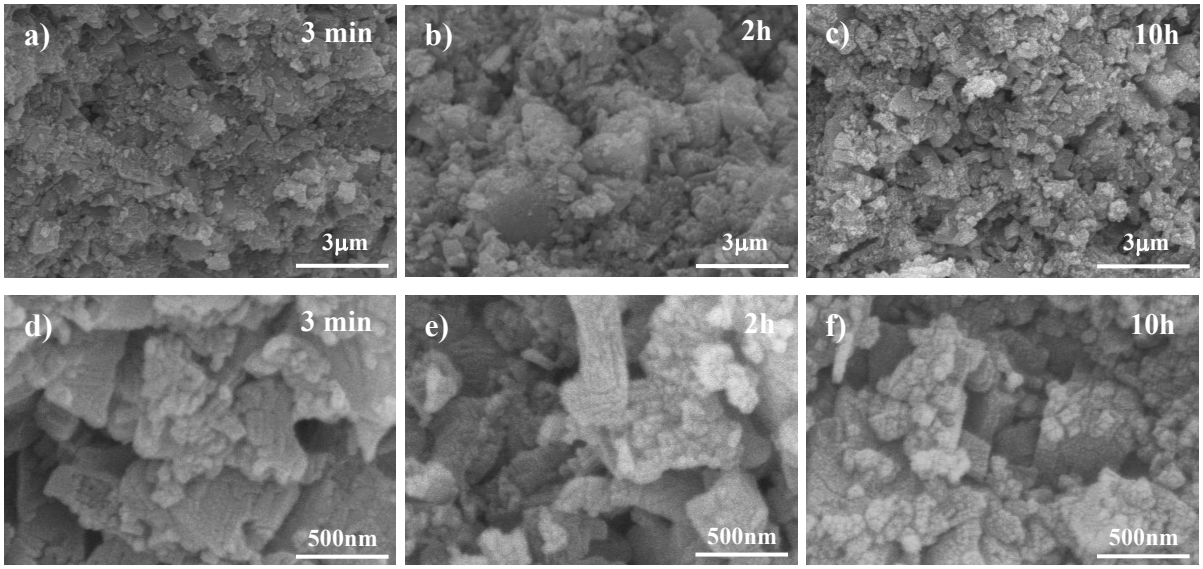

Figure III-13 – SEM micrographs of the sintered samples at 1200ºC for 3 min, a) and d), 2h, b) and e) and 10h c) and f).

SEM observations were done in samples heated at 1200ºC for 3min, 2h and 10h, as can be seen in Figure III-13. By observing those, and despite the low quality of the images caused by the reaction with air, there is no significant change. The sintering may first occurs among the nanometric grains, inside agglomerates, since ~45% of porosity was determined to exist in the powder particles.

III.2 Material Testing at ISOLDE-CERN

As referred in the experimental section II.6, page 53, the raw material used at ISOLDE to produce the old targets (henceforth CC2) was different from the one used in this study and its characteristics are presented in Table A-1 in the Appendix. A CaO powder target (T12) was produced from the $CaCO_3$ used in the past (CC2) and following synthesis conditions named “old procedure” (detailed in section II.6.1, page 53). The

microstructures of this powder before (T12, Table III-3) and after thermal treatment (S12, Table III-3) at 1200°C, for 48h, were characterized to have a comparison with the characteristics of the target produced with the "new procedure", ahead in this section.

In the "old procedure", samples from the center of the container (T12 – Center) and from the side (T12 – Side) were taken. The obtained results can be seen in Table III-3.

Table III-3 – Characterization of the CaO powders produced at ISOLDE, by the old target production method before (T12) and after a thermal treatment at 1200°C, 48h (S12).

Sample	Conditions	SSA (m2/g)	G_{BET} (nm)	XS (nm)	Pore Size (nm)	Porosity (%)
T12 - Center	CC2 with "old procedure"	25	71	46	11	33
T12 - Side		40	45	40	8	38
S12	T12 - Center at 1200°C for 48h	3.8	478	330	9	9

The difference between the center and side T12 samples is probably due to the thermal gradient in the target oven. Despite the high temperatures used, a nanometric powder was obtained. The difference between the samples T12 – Center and S12 show high sintering of the CaO powder: larger crystallite size, and a pore size and volume decrease. These results can explain the bad performance of these targets after some time of operation.

A sample of CaO (sample T80 in Table III-4) with the actual carbonate powder and the "new procedure" was prepared with equivalent thermal cycle conditions (temperature and time) of those used in University of Aveiro (UA), N80, to assess if the synthesis process was reproducible at ISOLDE.

Table III-4 – Characterization of the CaO powders produced at ISOLDE, using the new targets procedure (T80 and S80 and comparison with CaO powder obtained at UA (N80).

Sample	Conditions	SSA (m2/g)	G_{BET} (nm)	XS (nm)	Pore Size (nm)	Porosity (%)
N80	800°C for 2h at UA	58±4	31±3	32±2	12	44
T80	800°C for 2h at ISOLDE	42	43	-	20	47
S80	800°C for 48h at ISOLDE	37	48	37	23	47

There are some differences between the powder samples produced in UA and in ISOLDE, most probably due to the different equipment used to produce the CaO. A finer CaO is obtained through the "new process" as expected already (smaller grain size, higher surface area, porosity and pore volume). A long duration calcination cycle, 800°C, for 48h, was also done, sample S80, Table III-4, and small changes in the microstructural characteristics were observed when comparing it with sample T80, showing that the

produced microstructure is relatively stable at 800°C. From these results, the online operation temperature of this target was set to a maximum of 800°C. The new target material doesn't comply with the defined requirement of pore size [7,8] (>100 nm comparing to the obtained 20 nm), but this parameter is hard to control since it is characteristic of the $CaCO_3$ decomposition. One can also see that the CaO obtained from the "new procedure" (Table III-4) is finer and has larger pore size and volume than the one produced through the "old procedure" (Table III-3). The CC2 was also a coarser and less pure raw material.

A nanostructured material was already produced before at ISOLDE (as seen in the reproduced results in Table III-3), but this nanostructure was most of the times lost depending how the material was produced, handled and operated. Since no study or knowledge about this material didn't exist (or was lost) and since production, degas and handling phases were not controlled, it would be a coincidence for all the conditions to be combined in order to obtain a material with good release properties of isotopes. This explains the (sometimes) good isotope yields for this target, and the reported drop on them, meaning that the target was being heated to high, degrading the microstructure and so the yields over time.

A new target material was then produced according to "the new procedure" (detailed in section II.6.2 on page 54), and the new target was labeled with the reference CaO#469. The sample S80 (in Table III-4) was extracted from the center of the container, while the side sample indicated a very low surface area ($4.5 m^2/g$) and also the XRD showed $CaCO_3$ peaks only, stating only little or no decomposition. This is again a sign of a thermal gradient between the center and the side of the target oven. In section III.1.1, temperature influence studies on the $CaCO_3$ decomposition were done. This was further confirmed when weighting the Re boat, showing that the reaction was 95% complete, meaning that only a little quantity didn't decompose.

The material was transferred from the oven to the target container, in a gloves box under an Argon atmosphere in order to avoid exposure to air. This method proved to be effective, since no peaks from the $Ca(OH)_2$ phase were detected in the XRD, unlike most of the tests done in this study.

In this target unit, an inverse gradient to the one of the oven is formed. The temperature is lower at the center and higher at the sides as measured by two thermocouples. This was caused by a water cooled copper block around the transfer line

(see Figure I-4) in the center. As soon as temperatures approached 500°C at the sides of the container, there was a sudden increase of the pressure (up to 10^{-1} Pa), showing the decomposition of the remaining $CaCO_3$, which was completed after 50 min as the pressure went back to initial low pressures.

Afterwards, the normal procedure followed up (offline operation and outgassing for 3 days) at temperatures lower than 800°C to avoid any nanostructure degradation.

III.3 Online Studies

In order to test the impact of a nanostructure on the isotope release properties with respect of other calcium oxide targets, a benchmark of this material was obtained by testing the new unit CaO#469 in comparison with others previously used at ISOLDE. The release curves for several isotopes were monitored. Yields on ^{35}Ar were probed throughout the target run to check for possible yields drop. Also, release curves for ^{35}Ar and ^{19}Ne at 3 different target temperatures were taken in order to assess effusion and diffusion properties of the material. The release efficiency was calculated with values obtained from other CaO targets used before at ISOLDE.

III.3.1 Isotope Yields

The yields for ^{6}He, ^{10,15}C, ^{19}Ne, $^{31-33}$Ar and ^{35}Ar were measured and compared with a database compiling historical data of the best targets produced at ISOLDE [45], as seen in Table III-5.

Table III-5 – Measured yields and respective conditions for target CaO#469 and the comparison with database yields.

Isotope – $T_{1/2}$	Temperatures (°C)		Yield (ions/μC)	Database Yield (ions/μC), Target Temperature (°C) and Target Unit [45]
	Ion Source	Target		
^{6}He – 806.7ms	1970	650	2.3×10^{6}	2.6×10^{6} (1050°C) - CaO#123
^{10}C (CO) – 19.3s	1970	730	6.1×10^{5}	5.3×10^{5} (1050°C) - CaO#123
^{15}C (CO) – 2.45s	1970	730	7.0×10^{3}	6.2×10^{3} – SC Target
^{19}Ne – 17.22s	1970	650	9.6×10^{6}	7.5×10^{6} (1050°C) - CaO#123
^{31}Ar – 15.1ms	1970	650	4.2×10^{1}	5.0×10^{0} (>1050°C) - CaO#408
^{32}Ar – 98ms	1970	650	2.4×10^{3}	3.3×10^{3} (1050°C) - CaO#123
^{33}Ar – 174.1ms	1970	650	1.3×10^{5}	3.8×10^{4} (1050°C) - CaO#123
^{35}Ar – 1.78s	2070	840	2.0×10^{8}	4.3×10^{7} (1050°C) - CaO#123

Table III-5, shows a match or a significant increase of the yields of CaO#469 for most of the isotopes, versus the database yields. One of the main differences is the

temperature at which the target CaO#469 operated, relatively to the old targets. Since proton impact effect at ISOLDE is unknown for this material, the temperature was set to 650°C as regular operation temperature in order to partially compensate for the spike heating caused by the proton pulses. Whenever the target temperature was risen, it was only for the measurement in question, being lowered right away.

Clear improvement was obtained on ^{35}Ar yield, being 5 times superior to the one in the database, and the highest in all history of ISOLDE. This is consistent with the previous hypothesis that a controlled microstructure (nanostructure), leads to better yields. The good value for ^{35}Ar is even underestimated since part of the release curve was cut away, and only partly compensated by the fitting program. The ^{31}Ar yield measurement is probably the best achievement, being 8 times higher than database values, confirming again that a microstructure with smaller grains which have shorter diffusion lengths enhances the release, as will be discussed further ahead. The measured yields for ^{31,33,35}Ar and ^{10}C were all higher than database values, compared to any of the target materials used so far at ISOLDE. ^{19}Ne and ^{15}C isotope yields were the highest of all CaO past target units. Most of the yields were obtained with conservative running parameters to preserve the target nanostructure, which means that probably they can be further enhanced by increasing the target operation temperature, without compromising it.

The high yields, on the measured isotopes on the database [45], were mostly provided by target CaO#123 operated in 1999. Since then, these results were hard to reproduce mainly for the reasons detailed before (section III.2). The results of target CaO#123 were probably of such a good quality due to the use of a different production process [9], decomposing the $CaCO_3$ at a lower temperature (1000°C, instead of 1200°C used afterwards) in a single batch instead of 2, obtaining smaller grain sizes. Additionally, lower operation temperatures were used (1050°C), helping to keep the microstructure for longer times, comparing with other standard CaO targets which were operated at temperatures between 1050 and 1150°C [45] and also at 1340°C [9].

III.3.2 Yields Over Time

The CaO targets at ISOLDE, are reported to have low yields of exotic Ar isotopes from the beginning, or a fast drop when operated under proton irradiation. In this work it is shown that it can be avoided by maintaining the microstructure without significant

degradation due to sintering. An example of a relative drop on the yields for precedent targets is shown in Figure III-14 for ^{31,32}Ar.

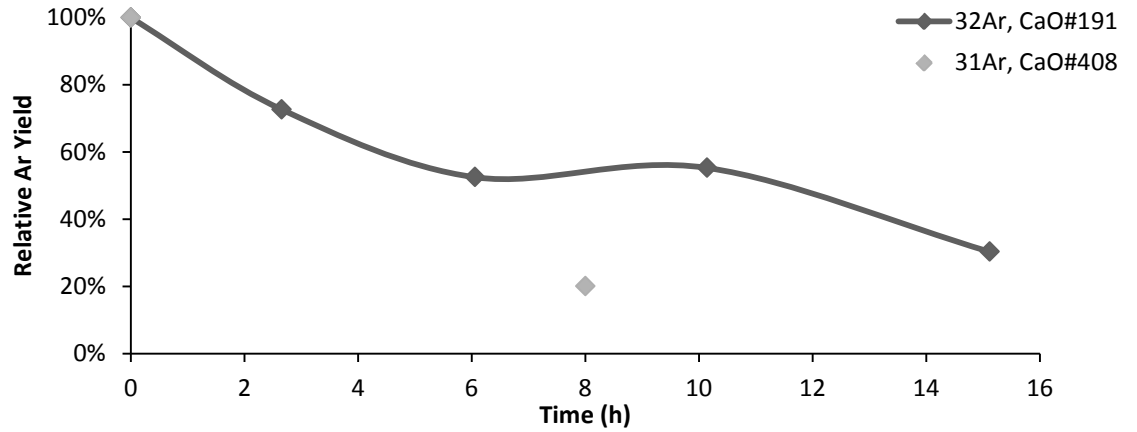

Figure III-14 - Yield evolution on ^{32}Ar on target CaO#191 in 2001 at ISOLDE (courtesy of Susanne Kreim) and ^{31}Ar in CaO#408.

As can be seen in Figure III-14, the yields dropped to 30% of the initial value in only 15h of operation time. The yield of this isotope is a good benchmark of the microstructure degradation since it is very short lived (98ms), so any increase on the grain size would increase the diffusion lengths that would directly affect the total release of ^{32}Ar. On another target, CaO#408, the yield on ^{31}Ar dropped by a factor 5 from 5 ions/μC after 8 hours of operation time. On the new target, CaO#469, the yields on the very short lived isotopes ($^{31\text{-}33}$Ar) were measured after 80 hours of operation. The measured numbers proved to be higher than in any previous target (especially for ^{31}Ar, see Figure III-14), but no measurements along time could be done.

The yield of ^{35}Ar was taken throughout the run, for target CaO#469, and compared to the yield drop on a standard target (CaO#419) as can be seen in Figure III-15.

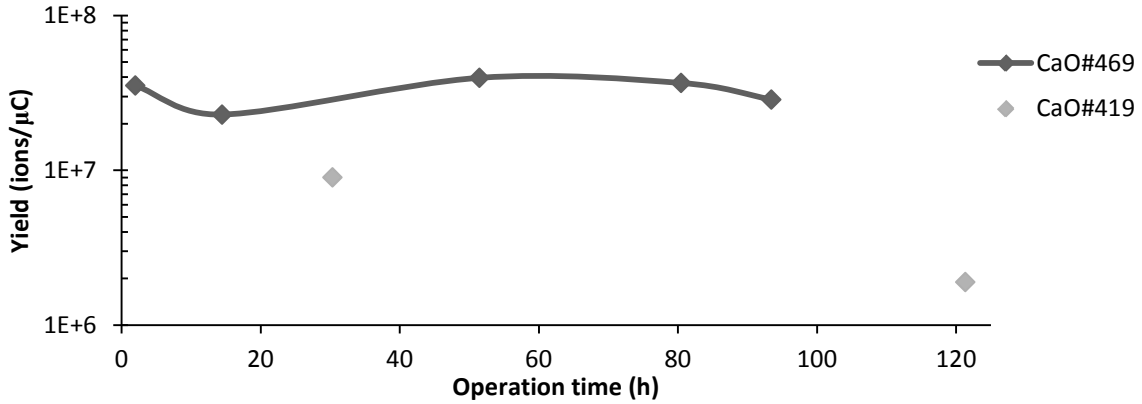

Figure III-15 - Yields of ^{35}Ar measured throughout the run for targets CaO#469 and CaO#419.

A drop of ~80% on the yield could be noticed on target CaO#419 after 120h, most probably related with the material microstructure degradation, even though this isotope is not a very short-lived one. On target CaO#469, one notices that, the yields are higher and there is no drop until the end of the run.

The stable yield indicates that the calcium oxide microstructure is stable. A confirmation of this comes with the measurement of the very short lived isotopes, $^{31-33}$Ar after 80 hours of operation. This means that the used settings (650^{o}C and 8x10^{12} protons per pulse) are appropriate to obtain stable CaO release properties, even though the temperature was risen to 730^{o}C and 840^{o}C for some hours to do some of the measurements. Since there was no degradation of the target release properties, studies with higher temperatures and/or proton intensities can be done in the future in order to provide better yields for beams delivered to experiments.

III.3.3 Isotope Release Properties

The calcium oxide release properties were assessed by measuring delay curves of ^{35}Ar, on targets CaO#469 and CaO#419 and fitted accordingly with equation (I.2) and the results are presented in Table III-6.

Parameters of the curves obtained at 950^{o}C for target CaO#419 are shown in table Table III-6, in which the ^{35}Ar yields dropped to 20% of the initial value during the run. In the case of CaO#469 the overall yields are higher, but the release (as can be seen by t_r, t_f and t_s in Table III-6) seems to be slower. This shows that the apparent time constants (t_r, t_f and t_s) are not easily related to effusion and diffusion phenomena and their time constants.

Table III-6 - Release time constants obtained by fitting the data with equation (I.2) for target CaO#419 and CaO#469 for ^{35}Ar.

Target	Temperature (^{o}C)	^{35}ArYield (ions/μC)	t_r (s)	t_f (s)	t_s (s)
CaO#419	950 (run start)	9.0x10^{6}	0.079	0.206	1.429
	950 (run end)	1.6x10^{6}	0.052	0.053	0.806
	500 (run end)	2.8x10^{5}	0.030	0.095	0.606
	680 (run end)	4.1x10^{5}	0.038	0.062	0.511
CaO#469	520	8.9x10^{6}	0.120	0.293	1.851
	730	3.9x10^{7}	0.126	0.408	1.805

In Table III-7, for target CaO#469 the release efficiency of ^{35}Ar increases with the temperature. This is to be expected since this should increase the rates of effusion and

diffusion phenomena. For CaO#419, which represents a standard ISOLDE CaO target, the release efficiency for ^{35}Ar is 1/5 of that of CaO#469, and it decays over the run to 1/35. For the very short lived isotopes, the release efficiency is higher in the case of CaO#469, than other targets (CaO#123 and CaO#408). Surprisingly, the same could not be seen for ^{32}Ar.

Table III-7 - Calculation of the release efficiency for Ar isotopes for the target CaO#469 and other older targets. Y_{prod} calculated from ABRABLA simulation for the different target thicknesses.

Target	Isotope – $T_{1/2}$	Temperature (^{o}C)	ε_{is} (%)	Y_{prod} (ions/μC)	Y_{obs} (ions/μC)	ε_{rel}(%)
CaO#469	^{31}Ar – 15.1ms	650		$3.2x10^{4}$	$4.2x10^{1}$	0.9
	^{32}Ar – 98ms			$1.1x10^{6}$	$2.4x10^{3}$	1.6
	^{33}Ar – 173ms		14.0	$2.0x10^{7}$	$1.2x10^{5}$	4.3
	^{35}Ar – 1.78s	520	7.2	$3.4x10^{9}$	$8.9x10^{6}$	3.6
		650	8.0		$3.5x10^{7}$	12.9
		730	6.1		$3.9x10^{7}$	19.2
		840	19.4		$2.0x10^{8}$	29.8
CaO#123	^{31}Ar – 15.1ms	1050	9	$1.8x10^{4}$	$1.5x10^{0}$	0.1
	^{32}Ar – 98ms			$6.2x10^{5}$	$3.3x10^{3}$	5.9
	^{33}Ar – 173ms			$1.1x10^{7}$	$3.8x10^{4}$	3.8
	^{35}Ar – 1.78s			$1.9x10^{9}$	$4.3x10^{7}$	25.1
CaO#408	^{31}Ar – 15.1ms	>1050	21	$2.0x10^{4}$	$5.0x10^{0}$	0.1
CaO#419	^{35}Ar – 1.78s	950 (run begin)	8	$1.8x10^{9}$	$9.0x10^{6}$	6.2
		950 (run end)			$1.9x10^{6}$	1.3

It is important to note that the ε_{rel} of the isotopes produced by CaO#123 are somehow close to the ones produced by CaO#469, at different operation temperatures with the exception of ^{31}Ar. Nevertheless, this shows that the good performance of these old targets (CaO#123) is possibly related, as explained before, to a better controlled microstructure. However degradation of the initial microstructure was experienced due to higher operation temperatures.

III.3.4 Diffusion and Effusion of Isotopes

Diffusion and effusion parameters can be extracted from the experimental release efficiency (equation (I.5)) of isotopes with different half-lives, using a fit of equation (I.19). To calculate the diffusion coefficient, the equation (I.17) was used and a particle size of 40 nm was considered from the sample S80, considered to be representative of the target material (see Table III-4, on page 74).

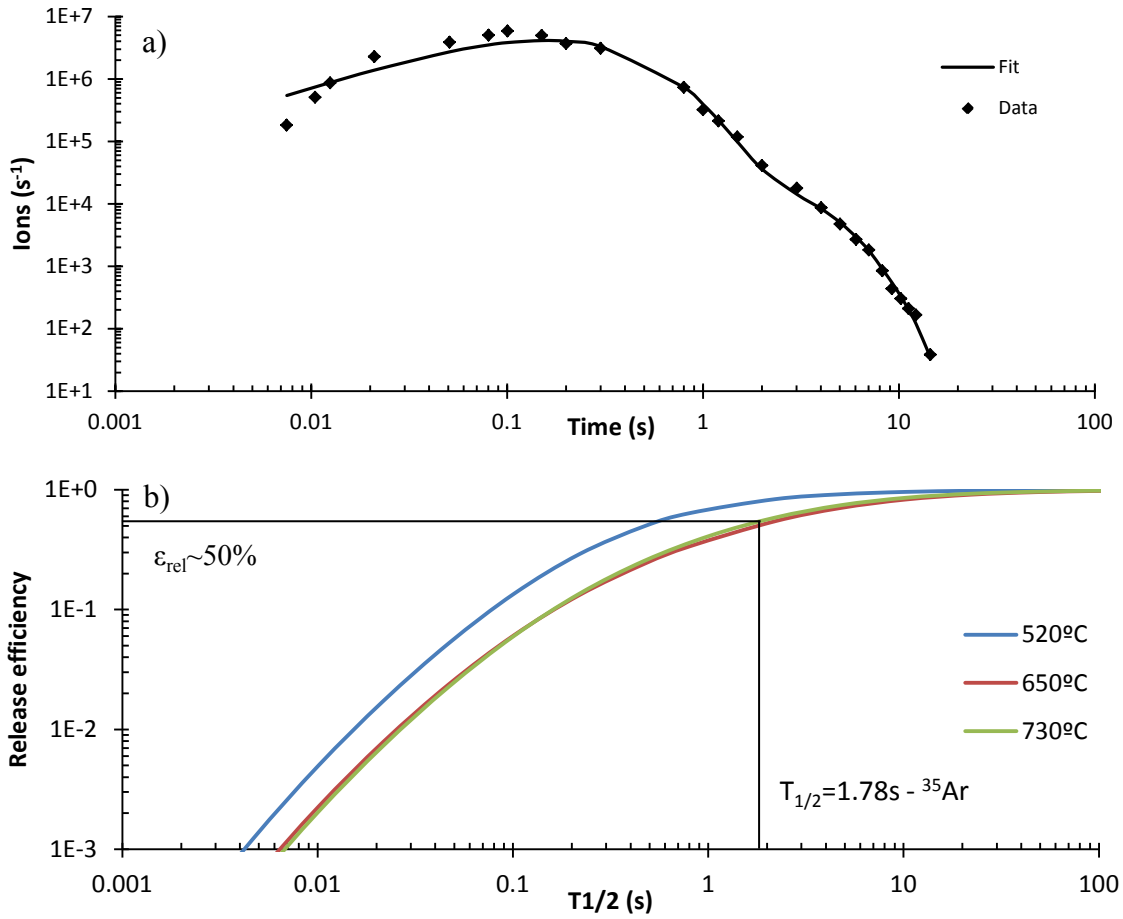

Figure III-16 – Example of release curve and respective fit, from equation (I.2), for ^{35}Ar at 520ºC (a) and release efficiency obtained through the fitting of the experimental release curves of ^{35}Ar for three different temperatures (b) in target CaO#469.

A representative example of a release curve fit of ^{35}Ar can be seen in Figure III-16 a). It can be seen that the fitted function does not match the first part of the release curve, which normally corresponds to where effusion phenomena is predominant. This induces an inconsistency later when obtaining the release efficiency curves, as can be seen in Figure III-16 b), where the release efficiency should be higher as higher is the temperature because effusion and diffusion rates are faster, improving the release efficiency. This especially fails in the case of the release efficiency at 520ºC, also confirmed by the values in Table III-8.

Table III-8 - Fitted effusion and diffusion parameters for ^{35}Ar for three different temperatures on target CaO#469.

Temperature (ºC)	Yield (ions/μC)	v_1 (s^{-1})	v_2 (s^{-1})	μ (s^{-1})	D (m^2/s)
520	8.9×10^{6}	160	2.13	5.22	1.6×10^{-16}
650	3.5×10^{7}	155	4.47	0.22	9.1×10^{-18}
730	3.9×10^{7}	144	3.59	0.29	1.2×10^{-17}

By comparing the values of μ and calculated D (in Table III-8), one can see that there is a logic tendency between the temperatures of 650°C and 730°C, which is not the case at 520°C. For the values of v_1 and v_2 there is no large evolution, whereas these should get higher as the temperature is increased. It shows that the difference between the fit and the data indeed affects the proper extraction of these parameters.

The diffusion delay parameter was alternatively deduced from the release efficiency by using equations (I.20) and (I.21), neglecting contributions from effusion as shown in Table III-9. The values are expected to be lower estimates of μ and D, since all losses are assumed to come from diffusion.

Table III-9 - Obtained diffusion parameters (neglected contribution from effusion) through the release efficiency of ^{35}Ar for three different temperatures on target CaO#469.

Temperature (°C)	ε_{is} (%)	Y_{prod} (ions/μC)	ε_{rel} (%)	μ (s^{-1})	D (m^2/s)
520°C	7.2	$3.4x10^9$	3.6	0.00058	$2.4x10^{-20}$
650°C	8.0		12.9	0.0078	$3.19x10^{-19}$
730°C	6.1		19.2	0.018	$7.4x10^{-19}$
840°C	19.4		29.8	0.047	$1.9x10^{-18}$

By looking at the values of μ in Table III-9, one can see that they are much lower than those obtained in Table III-8. The difference results from the disagreement between the release efficiencies determined by the two different methods (as seen in the values in Table III-9 and Figure III-16). These methods were already applied successfully before [37], which can means that a potentially error in the determination of the system efficiency might be in play: (i) it was detected that part of the beam was not being totally separated and lost in the way before or in the separator; (ii) the ion source efficiency can also be another source of the error since it can be overestimated, as seen already in past targets; (iii) experimental issues with the extraction and acceleration of the RIB were reported throughout the release measurements. All of these can have a strong influence on the proper assessment of the release process and efficiencies during the experimental tests. Another possible explanation may be related with a slow diffusion process (trapped or very slowly released Ar) which is in play (as shown in Table III-9 by the low values ofμ) which cannot be resolved by the current model, leading only to apparent diffusion values.

As expected the yield increases with the temperature, as can be seen in Table III-8. This is especially true in the case of diffusion which is the most limiting step, as can be

seen by the orders of diffusion and effusion time constants, v_1, v_2, and μ at 650°C and 730°C.

In the case of ^{19}Ne ($T_{1/2}$=17.22s), a representative example of a fitted release curve is also shown in Figure III-17 a), which fit agrees generally well with the data. The resulting release curves show, as expected, in Figure III-17 b), higher efficiencies for higher temperatures.

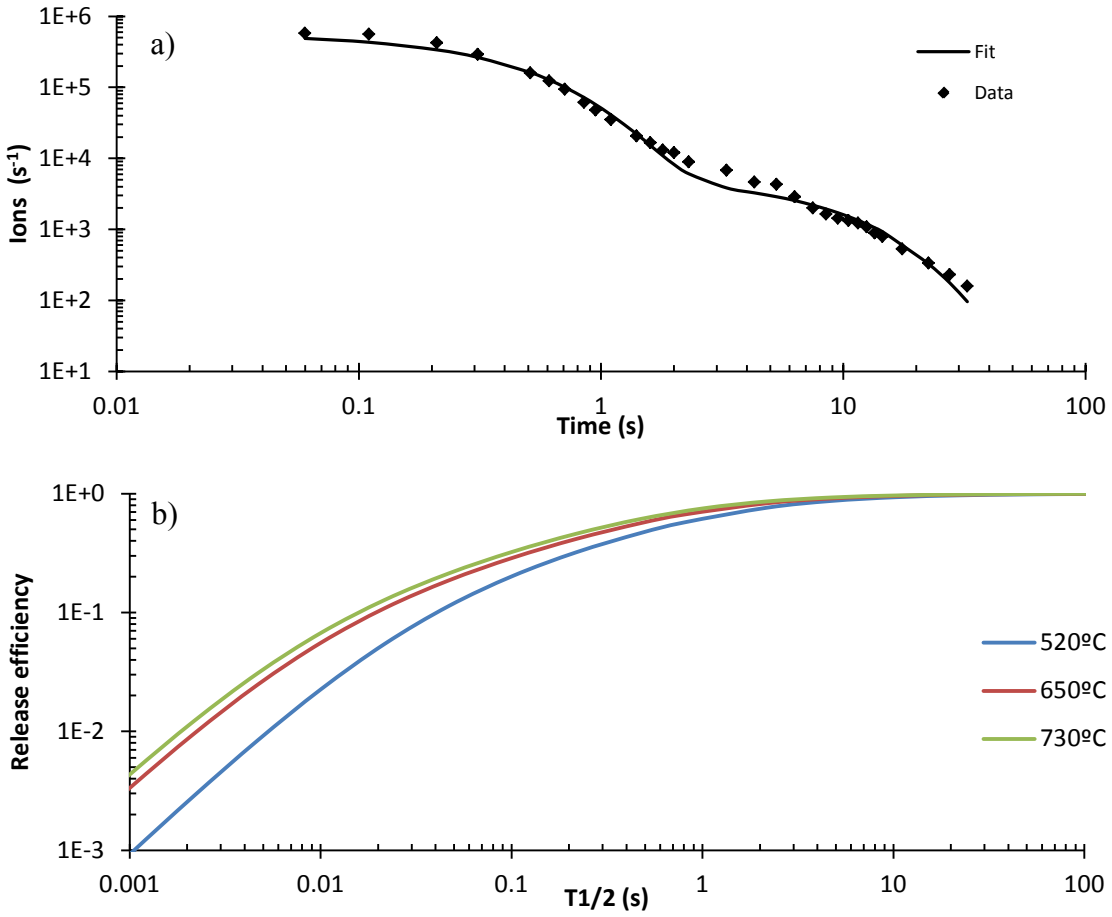

Figure III-17 – Example of release curve and respective fit, from equation (I.2), for ^{19}Ne at 520°C (a) Release efficiency obtained through the fitting of the experimental release curves of ^{19}Ne for three different temperatures in target CaO#469.

From the Table III-10 one can see that the values of v_1 and μ are increasing as the temperature increases, showing that temperature has a large influence on both diffusion and effusion. In the case of v_1 the values are unrealistic because of the rising part on the release curve could not be experimentally determined (see Figure III-17 a)) and respective t_r).

Calculations about release efficiency, similar to those made in Table III-9, cannot be done in the case of ^{19}Ne, since the ion source efficiency was not known. In terms of

yield, the values for 520°C and 650°C are in agreement, but for 730°C a mistuning in the high voltage of the extraction and acceleration of the RIB lead to beam losses, leading to a lower yield.

Table III-10 - Obtained effusion and diffusion fitted parameters for ^{19}Ne for three different temperatures on target CaO#469.

Temperature (°C)	Yield (ions/μC)	v_1 (s^{-1})	v_2 (s^{-1})	μ (s^{-1})	D (m^2/s)
520	2.8×10^{6}	2.7×10^{4}	23.9	0.62	2.5×10^{-17}
650	9.6×10^{6}	1.3×10^{11}	72.7	0.96	3.9×10^{-17}
730	6.6×10^{6}	3.4×10^{10}	84.9	1.23	5.0×10^{-17}

The values of D for both Ar and Ne on CaO cannot be compared to published figures in the literature. In both cases the release is limited by diffusion, except for the cases of the very short lived Ar isotopes, where it is also limited by effusion. Diffusion coefficients are in the order of 10^{-17} m^2/s for Neon and 10^{-18} m^2/s for Argon (or between for 10^{-20} and 10^{-19} m^2/s) in calcium oxide between 520 and 730°C. This was expected since neon is a smaller atom than argon and since they are both noble gases, neon should diffuse faster in the same matrix. The values of the diffusion delay time, μ, obtained by E. Bouquerel [35], were determined to be 1.79 s^{-1} for Ar in CaO at 1400°C. This value was taken in an old standard CaO target with a grain size at least one to two orders of magnitude larger (as discussed before). The diffusion delay time parameter is also compensated by the much higher temperature used. Further knowledge about the data treatment and the grain size would have to be known at this kind of temperatures for further conclusions. This value was also taken considering the equation (I.15), which is not for the spheres geometry, but for infinite foils. The diffusion values obtained in this study can also be influenced by the proton irradiation generated defects in the crystal structure. The effusion delay times obtained by E. Bouquerel [35] are 100 and 10.5 s^{-1}, which are in the same order of magnitude of the ones obtained in this work.

The values of diffusion coefficient of neon in aluminum oxide taken from the release fractions in a target for EURISOL [86], that is a close situation (neon in an oxide), they were, for the temperatures of 1100°C and 1450°C, 1×10^{-17} m^2/s and 7×10^{-17} m^2/s, respectively, which are very close to the ones obtained in this work. Furthermore from the diffusion coefficients of helium in a beryllium oxide target operated at ISOLDE [37], which is also a noble gas in an oxide, for temperatures between 800°C and 1400°C the diffusion coefficients were measured to be 10^{-13} to 10^{-14} m^2/s, which are still some orders of

magnitude higher than the ones obtained. Since helium is a much smaller atom than neon, and both are noble gases, helium diffusion coefficients are expected to be higher. Since the matrix in both cases is different further comparisons are not attempted.

From the calculated diffusion coefficients for ^{35}Ar and ^{19}Ne one can infer Q from equation (I.9) and the Arrhenius plot in Figure III-18. The calculated Q values are presented in Table III-11 for ^{35}Ar and ^{19}Ne. In the case of ^{35}Ar it is presented only for the first method (equation (I.21)).

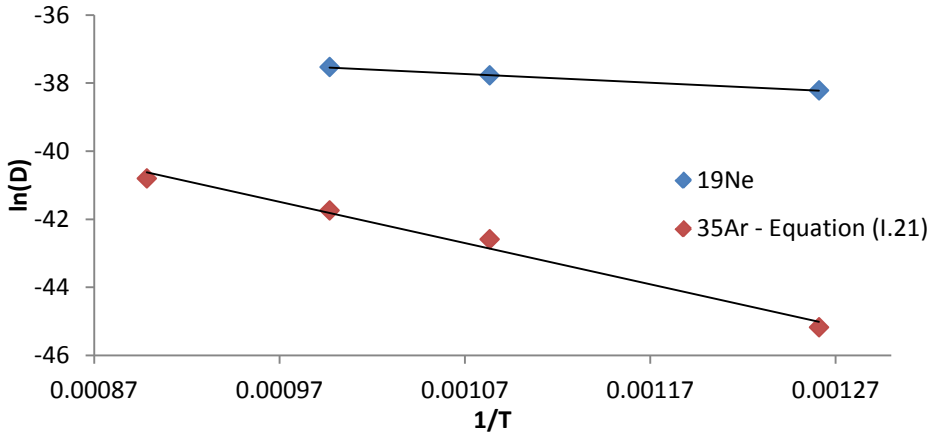

Figure III-18 - Plot of the ln(D) vs 1/T in order to determine D_0 and Q for ^{19}Ne and ^{35}Ar (the latter by a different method.

The fit to obtain Q is acceptable since the values of R^2 are close to 1 (Table III-11), even though there are few data points for each. It can be seen that the values of Q are low compared to the global activation energies (not the case of ^{35}Ar – equation (I.21)) obtained for diffusion which are generally in the order of hundreds of kJ/mol [48]. However in case of the diffusion of Ne in GeO_2 the reported activation energies in the temperature range of 37 to 400°C are comprised between 37 to 55 kJ mol^{-1} which are in the same order of magnitude than the ones obtained in this work [48].

Table III-11 - Values of Q and D_0 and respective R^2 for ^{19}Ne and ^{35}Ar.

Isotopes	Q (kJ mol^{-1})	R^2
^{35}Ar (equation (I.21))	101	0.986
^{19}Ne (equation (I.19))	21	0.999

Despite the disagreement obtained on ^{35}Ar, this is an attempt to take diffusion data out of online release curves. More accurate models and methods in terms of diffusion coefficients determination exist, but they are out of the scope of this work. Since there is no published data for Ar and Ne diffusion on CaO, no comments can be made about the

reliability of this method on this material. One should know that there are other errors associated to this method: grain size with direct impact on the values of *D*, since it is most probable, because of the thermal gradients during production and operation that the grain size varies. Another source of error can be the operation temperature which is not homogeneous throughout the target material. Further attempts in the future should be taken to explore and improve this process to study diffusion on target materials.

Chapter IV - Conclusions

IV.1 Conclusions

From the decomposition of $CaCO_3$ micrometric powder in vacuum ($p \leq 1$ Pa), at temperatures higher than 550°C, a mesoporous and nanometric (≥40 nm) powder could be obtained. For the same vacuum conditions, the powder crystallite size is lower and the surface area is higher as lower is the temperature used in the calcination process. The obtained CaO powders proved also to be very reactive in air to H_2O and CO_2 gases and special care was needed to be taken in storage and transport.

The vacuum sintering studies in nanometric CaO showed that the surface area has a net decrease from 1000°C which is accompanied by shrinkage. The kinetic analysis of the sintering results points to volume diffusion as controlling mechanism of matter transport during sintering at 1000-1200°C. The apparent activation energy was determined to be 155 kJ mol^{-1} close to the value of diffusion of Ca in CaO monocrystals, in the literature. From this study, one can also conclude that the temperatures used before for the target operation at ISOLDE, T>1050°C, degrade the CaO microstructure.

The CaO target material at ISOLDE-CERN was investigated. Based on the synthesis, reactivity and sintering results, changes were proposed for the production, operation and handling of the target material. The target was produced and operated at lower temperatures (T<800°C) and special care was taken due to the very fast hydration of this material.

The performance of the as produced CaO target material proved to be much higher and stable than standard CaO targets. The obtained yields for $^{31\text{-}33,35}Ar$, ^{19}Ne, ^{6}He, $^{10,15}C$ were higher than recent CaO targets, also higher or equivalent to the old (from 1999) CaO targets, and sometimes higher than any other target. No drop of the yields was seen. These results showed that choosing synthesis conditions to get a nanometric CaO powder and keeping its nanostructure during handling and operation, the release properties could be maintained over time.

By applying a mathematical model taking into account effusion and diffusion physical phenomena in the release curves at different temperatures, information on these parameters, for ^{19}Ne and ^{35}Ar in CaO, was extracted. As expected the diffusion times are much higher than effusion times, and diffusion is limiting most of the release. Diffusion coefficients were found to be in the order of $10^{-17} m^2/s$ for Neon and in between 10^{-20} and

$10^{-18}m^2/s$ for Argon in calcium oxide between 520 and 730°C. Activation energies for diffusion of Ne in CaO were found to be 21 kJ mol^{-1} and of Ar in CaO to be 101 kJ mol^{-1}.

IV.2 Outlook

A good improvement of the release properties of the calcium oxide as target material was achieved with this study. The target material development in this work is not only important to ISOLDE, but also for all other ISOL facilities throughout the world. Further investigation can still be done to further improve the release properties.

The improvements on this target material, permitted the WITCH experiment (Weak Interation Trap for Charged particles) at ISOLDE to obtain a yield good enough on ^{35}Ar and have results with good statistics, which they were attempting, unsuccessfully, for the last couple of years. It also improved the yield of the very exotic Ar isotopes which can be used for future experiments.

A nanometric material yet finer can be produced, but the sintering rates of this material, since it will be more reactive, have to be assessed before online operation. A good balance must be reached in terms of the nanostructured characteristics of the material and the temperature of online of operation, since both influences the diffusion times. Further studies on the limit operation temperature should be made, in order to keep the microstructure over time and tentatively increase the yields.

In this study, the CaO reactivity in air was only studied in order to prevent it. Further studies can still be done in this subject, especially in the kinetics of the reactions in air atmosphere, and determine when, with precision, either is the hydration or the carbonation reaction predominant.

The proton intensity used to operate this target was set to be low ($8x10^{12}$ protons per pulse). Studies with higher proton intensities can be done in order to study its influence on the release properties and on the degradation of the target material.

The method to obtain diffusion and effusion times from an online release curve, show be further explored in the future, in order to better study effusion and diffusion phenomena in target materials at ISOLDE.

Further improvements can be done in the target container design and in the oven to reduce the existent temperature gradient and avoid the creation of different microstructures along the material container.

The material study done on CaO clearly showed that better and stable isotope yields could be obtained, by knowing better how to produce, operate and handle the nanostructured material. Similar studies can be done for other oxide materials used at ISOLDE, certainly gaining in the release properties.

References

1. CERN. CERN in a nutshell. http://public.web.cern.ch/public/en/about/About-en.html (accessed August 13, 2011).
2. ISOLDE-CERN. The ISOLDE Facility. http://isolde.web.cern.ch/isolde/ (accessed August 13, 2011).
3. Kugler, E. The ISOLDE Facility. *Hyperfine Interactions* **2000,** *129,* 23-42.
4. Stora, T.; Bouquerel, E.; Bruno, L.; Catherall, R.; Fernandes, S.; Kasprowicz, P.; Lettry, J.; Marzari, S.; Nara Singh, B. S.; Noah, E.; Penescu, L.; Wilfinger, R. Oxide Target Designs for High Primary Beam Intensities for Future Radioactive Ion Beam Facilities. *CP1099, Application of Accelerators in Research and Industry: 20th International Conference*, 2009; pp 764-768.
5. Bennett, J. R. J. Targets for the Production of High Intensity Radioactive Ion Beams. *Nuclear Instruments and Methods in Physics Research B: Beam Interactions with Materials and Atoms* **1997,** *126,* 105-112.
6. Köster, U.; Bergmann, U. C.; Carminati, D.; Cathedral, R.; Cederkäl, J.; Correia, J. G.; Crepieux, B.; Dietrich, M.; Elder, K.; FEdoseyev, V. N.; Franchoo, L.; Fynbo, H.; Georg, U.; Giles, T.; Jonsson, O. C.; Kirchner, R.; Lau, C.; Lettry, J.; Maier, H. J.; Mishin, V. I.; Peräjärvi, M.; Ravn, H. L.; Rinaldi, T.; Santana-Leitner, M.; Wahl, U.; Weissman, L.; the ISOLDE Collaboration. Oxide Fiber Targets of ISOLDE. *Nuclear Instruments and Methods in Physics Research B: Beam Interactions with Materials & Atoms* **2003,** *204,* 303-313.
7. Fernandes, S. *Submicro- and Nanostructured Porous Materials for Productin of High-Intensity Exotic Radioactive Ion Beams;* PhD Thesis; École Polytechnique Fédérale de Lausanne: Lausanne, 2011.
8. Stora, T.; Fernandes da Visitação, S.; Mathot, S.; Bowen, P. *Nanostructured Target for Isotope Production;* Patent; CERN: Geneva, 2009.
9. Ravn, H. L.; Cathedrall, R.; Barker, J.; Drumm, P.; Evensen, A. H. M.; Hagebo, E.; Hoff, P.; Jonsson, O. C.; Kugler, E.; Lettry, J.; Steffensen, K.; Tengblad, O.; the ISOLDE Colaboration. Bunched Release of Gases from Oxide Targets. *Nuclear Instruments and Methods in Physics Research B: Beam Interactions with Materials*

and Atoms **1997,** *126,* 176-181.

10. Serway, R. A.; Moses, C. J.; Moyer, C. A. *Modern Physics,* 3rd ed.; Thompson Learning: Belmont, USA, 2005; pp 465-548.
11. Huyse, M. The Why and How of Radioactive-Beam Research. *Lecture Notes in Physics* **2004,** *651,* 1-32.
12. Minty, M. G.; Frank, Z. *Measurment and Control of Charged Particle Beams;* Springer: New York, 2003; pp 1-3.
13. Krane, K. S. *Introductory Nuclear Physics,* 3rd ed.; Wiley: Corvalis, Oregon, 1987; pp 1-8, 484-485.
14. Magill, J.; Pfennig, G.; Galy, J. *Karlsruher Chart of the Nuclides,* 7th ed.; Publications Office of the European Union, 2006.
15. International Atomic Energy Agency. Live Chart of Nuclides - Table of Nuclides. http://www-nds.iaea.org/relnsd/vchart/index.html (accessed August 13, 2011).
16. National Nuclear Data Center. Interactive Chart of Nuclides. http://www.nndc.bnl.gov/chart/reCenter.jsp?z=78&n=104 (accessed August 13, 2011).
17. Duppen, P. V. Isotope Separation On Line and Post Acceleration. *Lecture Notes in Physics* **2006,** *700,* 37-77.
18. Sauvageon, H. Deep spallation cross sections in high energy protons - Uranium interactions. *Zeitschrift Für Physik A Hadrons and Nuclei* **1987,** *326* (3), 301-308.
19. Morrissey, D. J.; Sherril, B. M. In-Flight Separation of Projectile Fragments. *Lecture Notes in Physics* **2004,** *651,* 113-135.
20. Köster, U. Intense Radioactive-Ion Beams Produced with the ISOL Method. *The European Physical Journal A* **2002,** *15,* 255-263.
21. Kowalska, M. Minutes of the 39th meeting of the INTC. *ISOLDE and Neutron Time-of-Flight Experiments Commitee*, Geneva, February 2011.
22. Serway, R. A.; Jewett, Jr., J. W. *Princípios de Física: Electromagnetismo,* 3rd ed.; Thompson: São Paulo, 2005; Vol. 3.
23. Kluge, H. -J. *ISOLDE Users' Guide;* Geneva, 1986.

24. Wolf, B., Ed. *Handbook of Ion Sources;* CRC Press: Darmstadt, 1995; pp 1-21.

25. Lettry, J.; Cathedrall, R.; Drumm, P.; Duppen, P. Van; Evensen, A. H. M.; Focker, G. J.; Jokinen, A.; Jonsson, O. C.; Kugler, E.; Ravn, H.; the ISOLDE Collaboration. Pulse shape of the ISOLDE Radioactive Ion Beams. *Nuclear Instruments and Methods in Physics Research B: Beam Interactions with Materials and Atoms* **1997,** *126,* 130-134.

26. Turrión, M.; Eller, M.; Cathedrall, R.; Fraile, L. M.; Herman-Izycka, U.; Köster, U.; Lettry, J.; Riisager, K.; Stora, T. Management of ISOLDE yields. *Nuclear Instruments and Methods in Physics Research B: Beam Interactions with Materials and Atoms* **2008,** *266,* 4674-4677.

27. Kirchner, R. On the release and ionization efficiency of catcher-ion-source systems in isotope separation on-line. *Nuclear Instruments and Methods in Physics Research B: Beam Interactions with Materials & Atoms* **1992,** *70,* 186-199.

28. Köster, U. ISOLDE target and ion source chemistry. *Radiochimica Acta* **2001,** *89,* 77777-77785.

29. Noah, E.; Bruno, L.; Cathedrall, R.; Lettry, J.; Stora, T. Hydrodynamics of ISOLDE liquid metal targets. *Nuclear Instruments and Methods in Physics Research B: Beam Interactions with Materials and Atoms* **2008,** *266,* 4303-4307.

30. Rahaman, M. N. *Ceramic Processing and Sintering,* 2nd ed.; CRC Press: Rolla, Missouri, 2003; pp 62-72, 126-156.

31. Smith, W. F. *Princípios de Ciência e Engenharia de Materiais;* McGraw-Hill: Lisboa, 1998; pp 103-115,144-153.

32. Callister, W. D. *Materials Science and Engineering: An Introduction,* 7th ed.; John Wiley& Sons, Inc.: Utah, 2007.

33. Kang, S.-J. L. *Sintering, Densification, Grain Growth & Microstructure;* Elsevier: Oxford, 2005.

34. Fernandes, S.; Bruetsch, R.; Cathedral, R.; Genther-Leopold, I.; Groeschel, F.; Lettry, J.; Manfrin, E.; Marzari, S.; Sgobba, S.; Noah, E.; Stora, T.; Zanini, L. Microstructure evolution of nanostructured and submicrometric porous refractory ceramics induced by a continuous high-energy proton beam. *Journal of Nuclear Materials* **2011,** Article in the Press.

35. Bouquerel, E. J. A. *Atomic Beam Merging and Suppression of Alkali Contaminants in Multi Body High Power Targets: Desing and Test of Target and Ion Source Prototypes at ISOLDE;* PhD Thesis; Université Paris XI: Orsay, 2009.

36. Ravn, L. H.; Carraz, L. C.; Denimal, J.; Kugler, E.; Skarestad, M.; Sundell, S.; Westgaard, L. New Techniques at ISOLDE-2. *Nuclear Instruments and Methods* **1976,** *139,* 267-273.

37. Stora, T.; Noah, E.; Hodak, R.; Hirsh, T. V.; Hass, M.; Kumar, V.; Kuljeet, S.; Vaintraub, S.; Delahaye, P.; Laurent, M. G. S.; Lhersonneau, G. A high intensity 6He for the beta-beam neutrino oscillation facility. Submited to Europhysics Letters.

38. Filges, D.; Frank, G. *Handbook of Spallation Research: Theory, Experiments and Applications;* Wiley VCH: Weinheim, 2009.

39. Gaimard, J.-J.; Schmidt, K.-H. A reexamination of the Abrasion-Ablation Model for the Description of the Nuclear Fragmentation Reaction. *Nuclear Physics A* **1991,** *351,* 709-754.

40. Carraz, L. C.; Sundell, S.; Ravn, H. L.; Skarestad, M.; Westgaard, L. High-Temperature Carbide Targets for Fast On-Line Mass Separation of Alkali and Noble Gas Elements. *Nuclear Instruments and Methods* **1979,** *158,* 69-80.

41. Portillo, M.; Nolen, J.; Gomes, I.; Panteleev, V. N.; Fedorov, D. V.; Barzakh, A. E.; Beznosjuk, V. I.; Moroz, F. V.; Orlov, S. Y.; Volkov, Y. M. Production of neutron-rich isotopes by one- and two-step processes in ISOL targets. *Nuclear Instruments and Methods in Physics Research B: Beam Interactions with Materials & Atoms* **2002,** *194,* 193-206.

42. Kjelber, A.; Rudstam, G. *The ISOLDE Isotope Separator On-Line Facility at CERN;* CERN: Geneva, 1970.

43. Ravn, H. L.; Bjornstad, T.; Hoff, P.; Jonsson, O. C.; Kugler, E.; Sundell, S.; Vosicki, B.; the ISOLDE Colaboration. *Use of Refractory Oxides, Carbides and Borides as Targets for On-Line Mass Separation;* CERN: Geneva, 1986.

44. CERN. INTC Agenda. http://indico.cern.ch/categoryDisplay.py?categId=2l85 (accessed November 21, 2011).

45. Turrion, M.; Urszula, H.-I. ISOLDE Yield

Database. https://oraweb.cern.ch/pls/isolde/query_tgt (accessed August 13, 2011).

46. Brady, G. S.; Clauser, H. R.; Vaccari, J. A. *Materials handbook : an encyclopedia for managers, technical professionals, purchasing and production managers, technicians, supervisors, and foremen,* 15th ed.; McGraw-Hill: New York, 2010; pp 540-541.
47. Lide, D. R., Ed. *CRC Handbook of Chemestry and Physics,* 84th ed.; CRC Press: New York, 2003.
48. Samsonov, G. V., Ed. *The Oxide Handbook,* 2nd ed.; IFI/PLENUM: Kiev, 1982.
49. Rodriguez-Navarro, C.; Ruiz-Agudo, E.; Luque, A.; Rodriguez-Navarro, A. B.; Ortega-Huertas, M. Thermal Decomposition of Calcite: Mechanisms of Formation and Textural Evolution of CaO Nanocrystals. *American Mineralogist* **2009,** *94* (4), 578-593.
50. Singh, A.; Kamruddin, M.; Ajikumar, P. K.; Tyagi, A. K.; Raghunathan, V. S.; Raj, B. Formation of Nanocrystalline Calcia by the Decomposition of Calcite. *Journal of the American Ceramic Society* **2002,** *85* (4), 927-932.
51. Dash, S.; Kamruddin, M.; Ajikumar, P. K.; Tyagi, A. K.; Raj, B. Nanorystalline and Metastable Phase Formation in Vacuum Thermal Decomposition of Calcium Carbonate. *Thermochimica Acta* **2000,** *363* (1-2), 129-135.
52. Weast, R. C., Ed. *CRC Handbook of Chemestry and Physics,* 64th ed.; CRC Press: New York, 1983.
53. Milne, C. R.; Silcox, G. D.; Pershing, D. W.; Kirchgessner, D. A. Calcination and Sintering Models for Application to High-Temperature Short-Time Sulfation of Calcium-Based Sorbents. *Industrial & Engineering Chemistry Research* **1990,** *29,* 139-149.
54. Beruto, D.; Barco, L.; Seacy, A. W.; Spinolo, G. Characterization of the Porous CaO Particles Formed by Decomposition of $CaCO_3$ and $Ca(OH)_2$ in Vacuum. *Journal of the American Ceramic Society* **1980,** *63* (7-8), 439-443.
55. Spinolo, G.; Anselmi-Tamburini, U. Mechanism of Low Temperature Calcite Decomposition. *Solid State Ionics* **1989,** *32/33,* 413-419.
56. Glasson, D. R. Reactivity of Lime and Related Oxides. I. Production of Calcium Oxide. *Journal of Applied Chemistry* **1958,** *8,* 793-797.

57. Maciejewski, M.; Oswald, H. R. Morphological Observations on the Thermal Decomposition of Calcium Carbonate. *Thermochimica Acta* **1985,** *85,* 39-42.

58. Beruto, D. T.; Searcy, A. W.; Kim, M. G. Microstructure, Kinetic, Thermodynamic Analysis for Calcite Decomposition: Free-Surface and Powder Bed Experiments. *Thermochimica Acta* **2004,** *424,* 99-109.

59. Criado, J. M.; Ortega, A. A Study of the Influence of Particle Size on the Thermal Decomposition of $CaCO_3$ by Means of Constant Rate Thermal Analysis. *Thermochimica Acta* **1992,** *195,* 163-167.

60. Beruto, D.; Searcy, A. W. Use of the Langmuir Method for Kinetic Studies of Decomposition Reactions: Calcite ($CaCO_3$). *Journal of the Chemical Society, Faraday Transactions 1: Physical Chemistry in Condensed Phases* **1974,** *70* (0), 2145-2153.

61. Powell, E. K.; Searcy, A. W. Surface Areas and Morphologies of CaO Produced by Decomposition of Large $CaCO_3$ Crystals in Vacuum. *Journal of the American Ceramic Society* **1982,** *65* (3), C-42-C-44.

62. Beruto, D.; Barco, L. Rearrangement of Porous CaO Aggregates During Calcite Decomposition in Vacuum. *Journal of the American Ceramic Society* **1983,** *66* (12), 893-896.

63. Ewing, J.; Beruto, D. The Nature of CaO Produced by Calcite Powder Decomposition in Vacuum and in CO_2. *Journal of the American Ceramic Society* **1979,** *62* (11-12), 580-584.

64. Towe, K. M. Ultrastructure of Calcite Decomposition in Vacuo. *Nature* **1978,** *274,* 239-240.

65. Beruto, D.; Barco, L.; Searcy, A. W. CO_2-Catalyzed Surface Area and Porosity Changes in High-Surface-Area CaO Aggregates. *Journal of the American Ceramic Society* **1984,** *67* (7), 512-516.

66. Beruto, D.; Searcy, A. W. Calcium Oxides of High Reactivity. *Nature* **1976,** *263,* 221-222.

67. Glasson, D. R. Reactivity of Lime and Related Oxides. V. Crystal Changes in Hydrated Lime at Different Temperatures. *Journal of Applied Chemistry* **1961,** *11,* 24-27.

68. Beruto, D.; Barco, L.; Belleri, G.; Searcy, A. W. Vapor-Phase Hydration of

Submicrometer CaO Particles. *Journal of the American Ceramic Society* **1981,** *64* (2), 74-80.

69. Bhattacharya, T. K.; Ghosh, A.; Das, S. K. Densification of Reactive Lime from Limestone. *Ceramics International* **2001,** *27,* 455-459.
70. Glasson, D. R. Reactivity of Lime and Related Oxides. VI. Crystal Changes in Carbonated Lime at Different Temperatures. *Journal of Applied Chemistry* **1961,** *11,* 28-34.
71. Glasson, D. R. Reactivity of Lime and Related Oxides. IV. Carbonation of Lime. *Journal of Applied Chemistry* **1960,** *10,* 42-48.
72. Chen, M.; Wang, N.; Yu, J.; Yamaguchi, A. Effect of Porosity on Carbonation and Hydration Resiscance of CaO Materials. *Journal of the European Ceramic Society* **2007,** *27,* 1953-1959.
73. German, R. M.; Munir, Z. A. Surface Area Reduction During Isothermal Sintering. *Journal of the American Ceramic Society* **1976,** *59* (9-10), 379-383.
74. Borgwardt, R. H. Sintering of Nascent Calcium Oxide. *Chemical Engineering Science* **1989,** *44* (1), 53-60.
75. Keyser, W. L.; Wollast, R.; Duvigneaud, P. H. The Sintering of Activated CaO. *Journal of Materials Science* **1969,** *4,* 989-996.
76. Borgwardt, R. H. Calcium Oxide Sintering in Atmospheres Containing Water and Carbon Dioxide. *Industrial & Engineering Chemistry Research* **1989,** *28,* 493-500.
77. Hammond, C. *The Basics of Crystallography and Diffraction,* 3rd ed.; Oxford University Press: New York, 2009; pp 216-219, 256.
78. Pecharsky, V. K.; Zavalij, P. Y. *Fundamentals of Powder Diffraction and Structural Characterization;* New York, 2005; pp 171-184.
79. Roque-Malherbe, R. M. A. *Adsortion and Diffusion in Nanoporous Materials;* CRC Press: New York, 2007; pp 79-105.
80. German, R. M. A Measure of the Number of Particles in Agglomerates. *The International Journal of Powder Metallurgy* **1996,** *32* (4), 36-373.
81. Condon, J. B. *Surface Area and Porosity Determinaion Measurments and Theory;* Elsevier: Amesterdan, 2006; pp 6-16.

82. Chu, S. Y. F.; Ekström, L. P.; Firestone, R. B. The Lund/LBNL Data Search. http://nucleardata.nuclear.lu.se/nucleardata/toi/index.asp (accessed August 13, 2011).

83. Glasson, D. R. Reactivity of Lime and Related Oxides. II. Sorption of Water Vapour on Calcium Oxide. *Journal of Applied Chemistry* **1958,** *8* (12), 798-803.

84. Lindner, R. Die Kinetik im Kalziumoxyd. *Acta Chemica Scandinavica* **1952,** *6,* 468-474.

85. Gupta, Y. P.; Weirick, L. J. Self-diffusion of calcium in single crystal calcium oxide. *Journal of Physics and Chemestry of Solids* **1967,** *28,* 811-821.

86. Fernandes, S.; Stora, T. *Eurisol Task #3 Deliverable Report - D3 - Online Tests of a High Power Al_2O_3 EURISOL Target Prototype;* EURISOL TM03-25-2009-0016; CERN: Geneva, 2009.

87. the ISOLDE Collaboration; Kugler, E.; Fiander, D.; Johnson, B.; Haas, H.; Przewloka, A.; Ravn, H. L.; Simon, D. J.; Zimmer, K. The new CERN-ISOLDE on-line mass-separator facility at the PS-Booster. *Nuclear Instruments and Methods in Physics Research Section B: Beam Interactions with Materials and Atoms* **1992,** *70* (1-4), 41-49.

Appendix

Table A-1 - Characteristics of the raw material ($CaCO_3$) used at ISOLDE to produce past CaO targets in the past (CC2).

Present Phases[*]	Calcite, Aragonite	**Impurities:**[*2]	
Avg. P. Size[*2]	14μm	**Sodium**	0.2%
SSA	0.33 m^2/g	**Strontium**	0.1%
G_{BET}	7.64μm	**Potassium**	0.01%
Purity[*2]	99%	**Chlorine**	0.005%
		Barium	0.005%
		Iron	0.001%
		Lead	0.0005%
		Copper	0.0005%

[*] Determined by Powder X-Ray Diffraction
[*2] *Merck*® information